2022-12-08

Focusing of High-Amplitude Sound Waves Using the Time Reversal Process

Brian D. Patchett
Brigham Young University

Focusing of High-Amplitude Sound Waves Using the Time Reversal Process

Brian D. Patchett

A dissertation submitted to the faculty of
Brigham Young University
in partial fulfillment of the requirements for the degree of

Doctor of Philosophy

Brian E. Anderson, Chair
Kent L. Gee
Scott D. Sommerfeldt
Tracianne B. Neilsen
Matthew S. Allen

Department of Physics and Astronomy

Brigham Young University

ABSTRACT

Focusing of High-Amplitude Sound Waves Using the Time Reversal Process

Brian D. Patchett
Department of Physics and Astronomy, BYU
Doctor of Philosophy

Time reversal is a method often used to focus sound to a desired location, and works best in a reverberant environment. The effect of focus location within a reverberant environment is presented first, revealing that proximity to reflecting surfaces has a significant effect on the amplitude of the focus both experimentally and when using a modal summation model. These effects are a primary component to creating focus signals at high amplitudes. High-amplitude focusing experiments show that when multiple sources are used simultaneously to generate a focus, a peak amplitude pressure spike of 200 dB can be achieved in air. A pressure spike of this amplitude has multiple nonlinear characteristics, and an investigation into the spatiotemporal features and harmonic content of these signals was conducted. The peak amplitude of the focus signal also increases in amplitude nonlinearly as the loudspeaker volume is linearly increased. This nonlinear increase is the primary subject of investigation in this work. Experimental and computational methods are implemented in order to understand the mechanisms driving the nonlinear increases observed when the sources are combined acoustically as opposed to linear superposition of the contributions from each sound in post-processing. Finally, models of converging high-amplitude waves are generated using the k-Wave© package for MATLAB©. These show a similar nonlinear increase in amplitudes, supporting the hypothesis of a Mach wave coalescence. A COMSOL finite element model allows visualization of the converging waves with Mach stems forming in free space to cause the nonlinear amplification.

Keywords: time reversal, focus, high amplitude, acoustics, aeroacoustics, nonlinear

ACKNOWLEDGMENTS

I would like to thank my advisor, Brian Anderson, for taking a chance on me when I was a non-traditional student working at another university, and his willingness to help me struggle through unfunded research to make something meaningful of it. Your patience and your faith in me over these years is what gave me faith in myself, thank you.

I would also like to thank Dr. Kent Gee, who was willing to sit down with me long before I thought acoustics would be a realistic career path and talk me through all of the potential and possibilities it held. Though it sounded intimidating, you made it feel as though it was worth fighting every obstacle to discover how something as simple as sound could be full of so much complexity.

To all of my committee members who have had patience and given guidance as I have worked to make deadlines, finish classes, and pass candidacy exams, I have appreciated each of you and your willingness to work with me when I felt I'd never reach the finish line, thank you all.

Thank you to my family. Without their constant encouragement, infinite patience, and willingness to sacrifice this never would have been possible. And especially to my wife, Elizabeth, whose constant support has helped me to do something that I never thought I could do.

Table of Contents

List of Figures

Chapter 1

An Introduction to Time-Reversal Acoustics

1.1 Introduction

Time reversal (TR) is a signal processing technique that has been utilized in many areas of wave-based physics.[1,2] In acoustics, its purpose began as a way to remotely reconstruct a reproducible source signal in an underwater environment. This proved effective in underwater communications, and was initially termed matched signal processing.[3-5] In modern times TR has been used as a communication tool in highly reverberant environments, as well as a method of detecting imperfections or cracks in solid media.[6-17] All of these methods take advantage of multiple reflections in the system to intentionally focus a signal at a predetermined location from a single source or bank of multiple sources.

The TR process involves two primary steps in order to successfully focus a signal. In the initial step, often referred to as the *forward step*, a signal is broadcast into a reverberant environment from a source location and recorded by a receiver located somewhere within the same environment. The signal used in this work is a logarithmically swept chirp signal. The receiver records the response of the environment to the broadcast; this data is referred to as the chirp response (CR). The CR can be defined mathematically as the convolution of the chirp signal with the impulse response (IR) of the environment. Once recorded, the CR is deconvolved to calculate the IR by cross-correlating it computationally with the original chirp signal in order to obtain the IR of the environment. The second step, often termed the *backward step*, is done by reversing the IR on the time axis, and broadcasting this new time-reversed impulse response (TRIR) from the source position(s).[18] The waves broadcast in this TRIR retrace the path of the reflections in the

reverberant environment and converge at the receiver position, reconstructing an acoustic impulse (pressure spike), called a focus.

This method of TR, where the source and receiver are left in place to perform the backward step, is referred to as reciprocal TR.[2] It assumes that the environment through which the signal passes is time-invariant. Assuming these properties hold, the IR records how waves travel from the source to the receiver in the environment. The IR is impacted by the size and shape of the environment, any absorption or propagation losses, and any objects that may be contained in the environment.[19] Not only can this process be used to generate an impulsive focus, but a communication signal can be convolved with the TRIR in order to focus the communication signal.

The following sections introduce additional details of the TR process, as well as applications of TR to multiple fields of science. It begins with an overview of the history of the research done in TR up to the present. A discussion of the most common experimental methods is presented with the fundamental mathematical descriptions of TR included, as well as the most popular modeling methods for generating a TRIR for a defined space. The introduction then concludes with an overview of the work presented in this dissertation.

1.2 An Overview of Time-Reversal Research

In the early 1960's, Antares Parvulescu and Clarence Clay[4,5] conceived of an experiment wherein a signal could be broadcast from a source in a reverberant environment to a receiver in that environment. The received signal could then be broadcast in reverse, traveling through that same environment, and thus the result was a reversed signal combined with a matching forward version of that signal. This approach allowed for the reconstruction of the original broadcast signal at the receiver location. This experiment was then performed at sea in order to demonstrate the technique

as a way of reproducing signals between fixed points in the ocean. Between the 60's and the 80's a related technique called optical phase conjugation was developed for imaging with antennas.[20-25] In 1990 Jackson and Dowling[26] summarized the applications phase conjugation to underwater acoustics. Researchers in France began exploring TR applications and usefulness once again in the 1990's when technology was sufficiently advanced to perform these complex experiments in a much more cost and time effective manner. In a 1997 article published in Physics Today, Mathias Fink[1] outlined the most current experimental and theoretical ideas of TR, setting the groundwork for the technique to be built upon by many fields of scientific research.

One common field of research is in the non-destructive evaluation of materials (NDE). In the NDE of solid materials, high amplitude TR is utilized to locate potentially damaged regions inside of a material through excitation using ultrasound.[15,17-18] This technique has been used to detect and locate nonlinearities in solids that are indicative of the presence of cracks in the crystal structure of the material.[17-19] By making a relative comparison of a high amplitude focus signal that is applied to both damaged and undamaged locations, one can determine the size and location of the damaged area by analyzing the nonlinear response characteristics that are present at those locations in their high amplitude focal signals. Many popular analysis methods have been developed in the field of NDE. The scaling-subtraction method, which shows the difference in linear and nonlinear responses, can be used in both the frequency and time domains, and was first introduced by Scalerandi *et al.*[12] as a method of analysis that forgoes the necessity of performing a fast Fourier transform. The phase inversion (or pulse inversion) technique was developed as a method by Sutin *et al.*[27] for use in the detection of nonlinear signals generated by landmines. This approach was later implemented by Ulrich *et al.*[13] as a NDE crack detection method. Finally,

Ciampa and Meo[28] produced a technique of phase symmetry, investigating third-order nonlinear effects present in a defective material.

Biomedical applications of high-amplitude TR have been studied by researchers in the destruction of accumulated calculus within the soft tissues of the body, known as lithotripsy. Thomas *et al.*[29] used this technique to destroy several kidney stones using a high amplitude TR mirror. Time-reversal histotripsy has been applied by several groups to focus sound through the inhomogeneities of a human skull, targeting lesions found within the soft tissue of the brain.[30,31] The structure of human teeth has also been studied using TR techniques with ultrasound by Dos Santos and Prevorovsky.[32] In this technique, nonlinear elastic waves properties are used to define the entire structure, as well as locate defects such as cracks in the tooth that could lead to decay. Each of these studies focused more on the application of high-amplitude TR and the frequency content of the signals within the tissues and structures under investigation, rather than looking for insights into the details of nonlinearities occurring in the signals themselves.

On a larger scale, TR (not necessarily used at high amplitudes) is also used to track and locate the origination point of seismic activity in the Earth's crust, as well as in glacial masses.[33] By using signals recorded by seismometers, the waves produced by seismic activity can be retraced to their origin. Additionally, Larmat *et al.*[34] showed that sufficient information could be recreated, if enough data is available, to allow the scientist to characterize the type of geophysical event that happened (e.g., if the earthquake was a subduction event or a transform sliding of plates).

Research into communication in complex or highly reverberant environments has benefitted from TR techniques (again not necessarily conducted at high amplitudes).[6-7,9] Due to TR's dependence on the reverberation of a given environment, effectively transmitting a signal through this type of space from a source location to a receiver is trivial. Thanks to work done by

Ribay *et al.*[8] and others, the number of sources was shown to have an effect on the amplitude of the focus, increasing its value for each source added to the process. They also showed that the reverberation time of a given environment and the bandwidth of the IR calculated in the process would affect the focus amplitude significantly. Denison and Anderson[35] found that while increasing the dimensions of the room would increase reverberation time, it also lowered the peak amplitude of the focus signals. Smaller reverberant environments generated higher-amplitude focuses than larger ones. In an additional study, Denison and Anderson[36] found that placing the sources further from the focusing location (beyond the critical distance) increased the focus amplitude, as did placing the sources and receiver in the same Cartesian plane. Anderson *et al.* [37] were also able to show that focusing benefitted from reducing the direct sound from source to receiver by aiming the sources away from the receiver location. In addition to these physical changes in experimentation to benefit the TR process, several signal processing techniques have been developed that aid in focus generation as well. These processes are outlined in the following section.

Wallace and Anderson[38] were able to show that high amplitude focusing of two different ultrasound frequencies produced a difference frequency at the focal location. This work also showed that the diffusiveness of a source through the application of beam blockers contributes to higher amplitude peak focus levels of the generated difference frequency. A paper by Furlong *et al*.[39] was able to show that when focusing a continuous signal in order to mitigate noise experienced by patients undergoing an MRI, TR used in conjunction with active noise control signals was effective at lowering the sound level patients could experience by 18 dB. Most recently, Patchett *et al.*[40] was able to show a direct relationship between the placement of the receiver within a reverberation chamber and the peak amplitude of the focus. This work showed

that as the receiver is brought near to more reflective surfaces, the amplitude of the focus increases significantly.

1.3 Experimental Practices in Time-Reversal Acoustics

As introduced in the previous section, TR in reverberant environments is conducted by broadcasting a predetermined signal into the environment (see Fig. 1 (a)). This signal then travels to a receiver location tracing a large number of paths across the reflective and absorptive boundaries of the space. The resulting response is recorded at the receiver location. This is the CR signal mentioned previously (see Fig. 1 (b)). The CR signal can be defined mathematically as the convolution of the original chirp signal and the impulse response (IR in the time domain) of the room.

$$\mathrm{CR} = \int_{-\infty}^{\infty} h(t)c(t-\tau)d\tau \tag{1.1}$$

where c represents the chirp broadcast into the room, and h represents the impulse response function of the room, both in the time-domain. In order to obtain the IR, a deconvolution is performed to remove the chirp from the CR and the result is the IR of the space. The deconvolution is actually done here using a cross-correlation of the chirp with the CR to obtain the IR. By applying fast-Fourier transforms, the cross-correlation can be done in the frequency domain, speeding up the computational process significantly by transforming convolution and deconvolution processes into simpler multiplication and division processes:

$$\mathrm{CR} = C(\omega) \cdot H(\omega) \tag{1.2}$$

$$C^*(\omega) \cdot \mathrm{CR} = |C|^2 \cdot H(\omega) \tag{1.3}$$

Where $C(\omega)$ and $H(\omega)$ are the fast-Fourier transforms of the $c(t)$ and $h(t)$ terms in Eq. 1.1 respectively, and the * symbol represents a complex conjugate of the function. The terms on the

left-hand side of Eq. 1.3 represent a cross-correlation of the original chirp signal with the CR recorded at the receiver position.

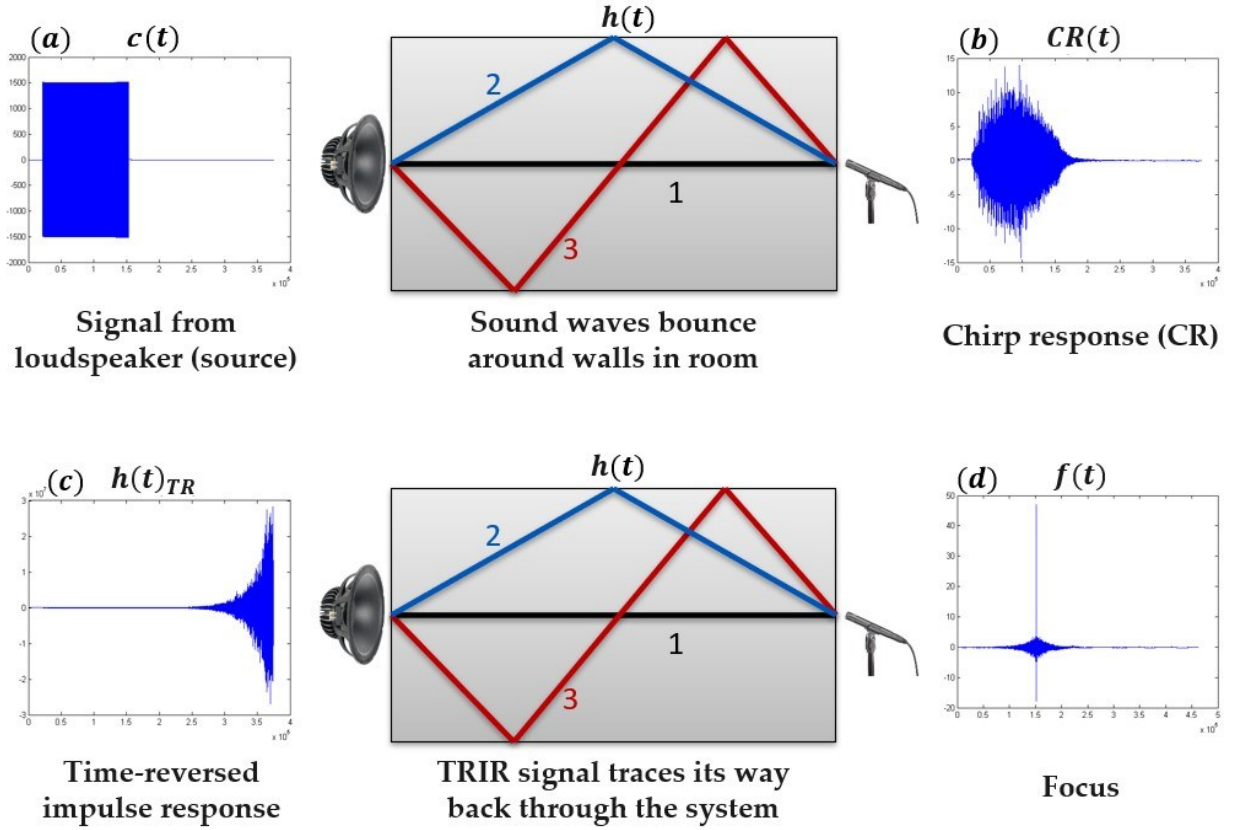

FIGURE 1.1: (a) Typical logarithmic chirp used in the forward step as the signal broadcast into the reverberant environment. (b) Chirp response recorded at the receiver position. (c) The calculated time-reversed impulse response for the backward step. (d) Focus signal generated at the receiver position.

When normalized, the right-hand side of Eq. 1.3 represents the normalized transfer function of the system. Applying an inverse fast-Fourier transform to the normalized transfer function returns the IR of the system. Once obtained, the IR is reversed on the time axis and broadcast from

the original source position (see Fig. 1 (c)). Mathematically, this is the same process as convolving the IR of the environment with a matched signal to that environment, effectively producing an approximation of an impulse at the receiver location. The recording of the time evolution at the focal location with the focused impulse is referred to as the focus signal (see Fig. 1 (d)).

The primary goal of this dissertation is centered on the generation of high amplitude impulsive pressure spikes through the broadcast of the TRIR, which produces constructive interference at the focus location and nowhere else. This method of simply broadcasting the TRIR is the simplest form of TR experimentation, and is termed the traditional TR process. However, manipulation of the focus signal spatial resolution and amplitude can be achieved through multiple forms of preprocessing of the TRIR. These preprocessing techniques are typically implemented as singular methods of effecting the focus signal, and not performed together.

The inverse filtering method in TR, also known as the deconvolution method, is capable of generating focus signal with high spatiotemporal resolution.[41] This method differs mathematically from the traditional TRIR process outlined by Eqs. 1.2-1.3 in that the transfer function is redefined to have no null terms (see Eq. 1.4). This technique leads to a lower amplitude of the peak in the focus signal relative to traditional TR, but Anderson *et al.*[3] found that for approximating a delta function in air, it is the most successful method of TR. Acquiring the TRIR in this way requires the optimization of a regularization constant, γ, to avoid the possibility of having a zero value in the denominator of the equation given by Anderson *et al.*,

$$H_d(\omega) = \frac{H^*(\omega)}{|H(\omega)|^2 + \gamma \cdot \mathrm{mean}(|H(\omega)|^2)} \tag{1.4}$$

Where $H_d(\omega)$ represents the deconvolution transfer function. The γ value a regularization parameter that can be adjusted to find a focus signal with the greatest spatiotemporal resolution.

The one-bit method, introduced by Derode *et al.,*[42] differs from the deconvolution method by performing the TR process as outlined in Eqs. 1.2-1.3, with the addition of imposing a threshold to the TRIR. All values above this threshold are clipped so that when the signal is normalized, they have a value of 1 (negative values below the negative threshold are set to -1), and all values with an absolute value below the threshold are set to 0. An example of a One-bit processed TRIR is compared to the traditional TRIR in Fig. 1.2.

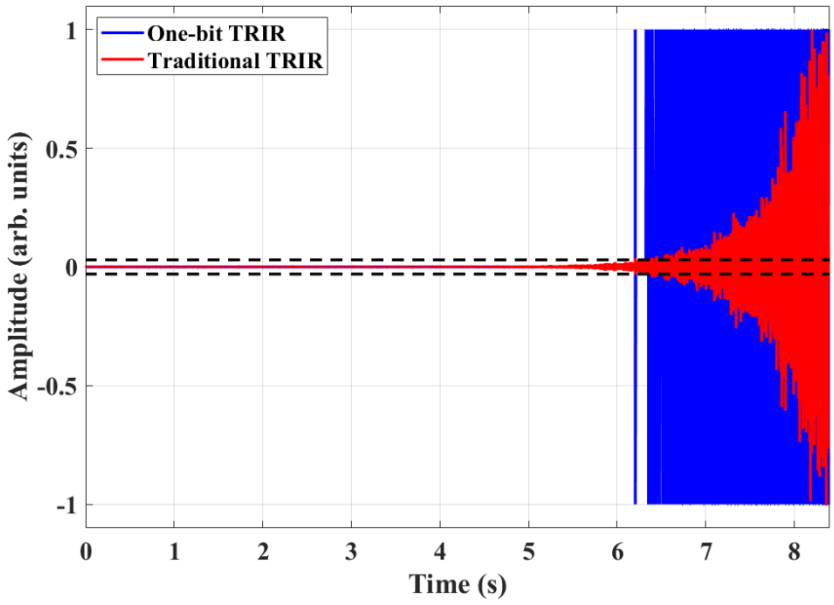

FIGURE 1.2: A comparison of the one-bit method signal process versus the traditional time-reversed impulse response without clipping applied. The threshold for the one-bit process is shown as the black dashed line.

This method is intended to achieve the highest possible peak focus amplitude by increasing the energy of the signal when the TRIR is broadcast. Setting the values below the threshold to 0 helps to eliminate unwanted background noise from the focus signal. While this method is not as

effective at generating high spatial resolution focus signal production, it preserves the phase information of the TRIR, and is shown to increase the peak focus amplitude by an average of 12 dB_{pk} in the work done by Derode *et al.*

Similar to the one-bit method, the clipping method has been shown to produce the highest peak amplitude.[41,43] In the clipping method, a threshold is applied to the TRIR just as in the one-bit method. However, all values at amplitudes between the set thresholds are retained and not set to zero. Figure 1.3 compares a TRIR that has been processed with the clipping technique against a traditional TRIR. While this method retains possible noise in the signal, reducing the resolution of the focus, it retains the energy of the lower amplitude parts of the TRIR and allows them to contribute to the focused amplitude.

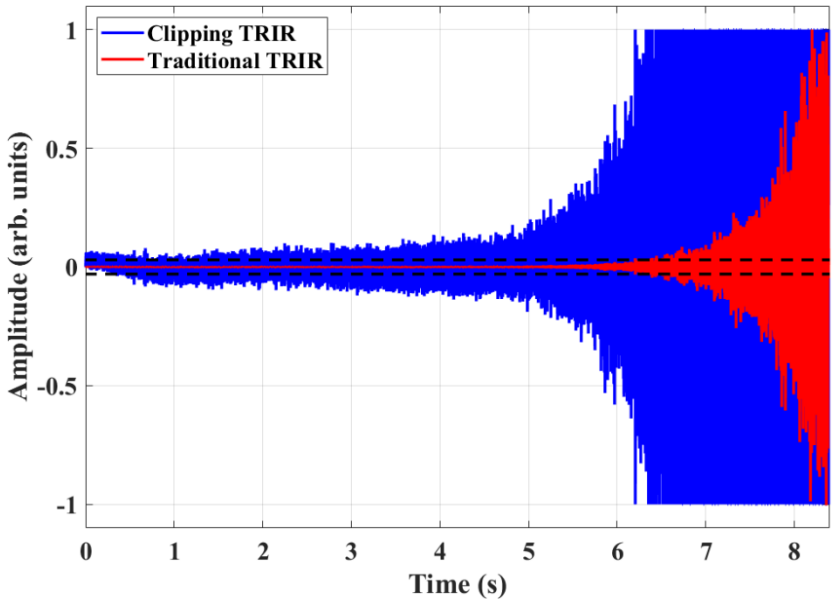

FIGURE 1.3: A comparison of the clipping method signal process versus the traditional time-reversed impulse response without clipping applied. The threshold of clipping is shown as the black dashed line.

The final method of modifying a TRIR is known as decay compensation. It is a method introduced by Gliozzi *et al.*[44] where the exponential decay of the IR is compensated for by fitting a curve to the TRIR (in first-order decay compensation this takes the form of a Hilbert transform), and then multiplying the inverted form of this curve by the TRIR. This effectively compensates for the decay in the TRIR and raises all of the amplitudes of the reflections to their maximum possible value prior to amplification. Figure 1.4 compares a decay compensated TRIR against a traditional TRIR.

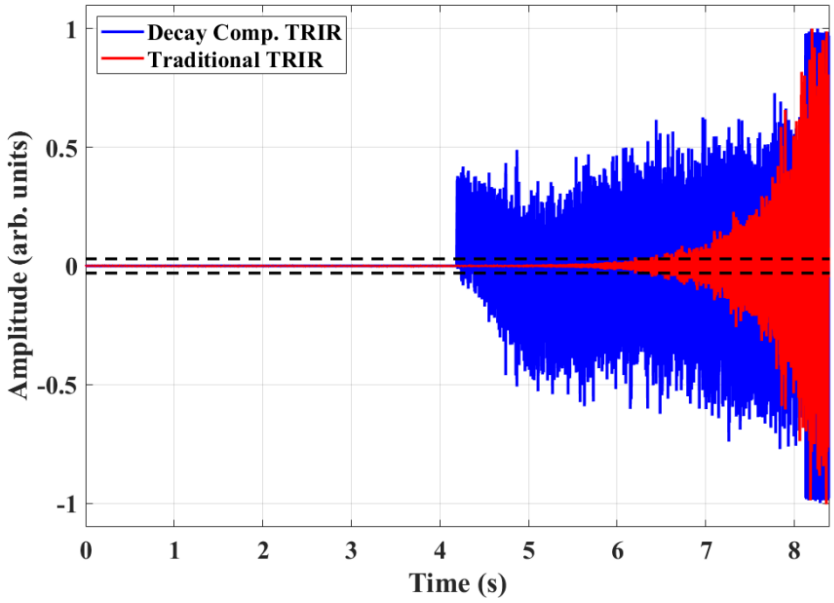

FIGURE 1.4: A comparison of the decay compensation method signal process versus the traditional time-reversed impulse response without clipping applied. The threshold of decay is shown as the black dashed line.

These methods were studied in greater detail for application of TR of audible sound in rooms by Willardson *et al.*,[41] in which the authors attempted to maximize the peak focus amplitude

in a reverberant environment through application of the clipping technique in preprocessing and manipulation of the physical experimental environment as outlined previously (e.g., source placement, loudspeaker placement, etc.). Young *et al.*[43] investigated similar techniques when analyzing nondestructive evaluation methods of stress corrosion crack detection in metal.

1.4 Common Modeling Methods in TR

One of the most common methods of generating a modeled impulse response is by using a technique known as the image source method.[45] Reflections of a source off of a hard boundary can be thought of as waves emanating from their own source (referred to as the image source) on the other side of the boundary, but now with the boundary removed. An example of a real and an image source relationship to the receiver is depicted in Fig. 1.5.

By redefining the reflections in this way, one can imagine a whole series of these types of image sources placed in an imaginary three-dimensional array existing beyond the now imaginary reflective boundaries of the room that all broadcast at the same time to provide arrivals at the receiver that coincide with when reflected waves would arrive at the receiver. This method has been successful at generating approximations of the IR computationally between a source and receiver. Once calculated, the autocorrelation of the IR generates a computational approximation of a focus signal at the receiver position. When properly generated, this method can account for propagation losses, thermo-viscous losses, and absorption losses at the walls, making it a very good approximation tool. Denison and Anderson[35,36] used this tool. However, the image source modeling method has not yet been successful at replicating experimental data showing that placing receivers near a wall (within one to several centimeters) or reflecting surface the amplitude of a focus increases. This increase is not yet apparent in image source modeling.

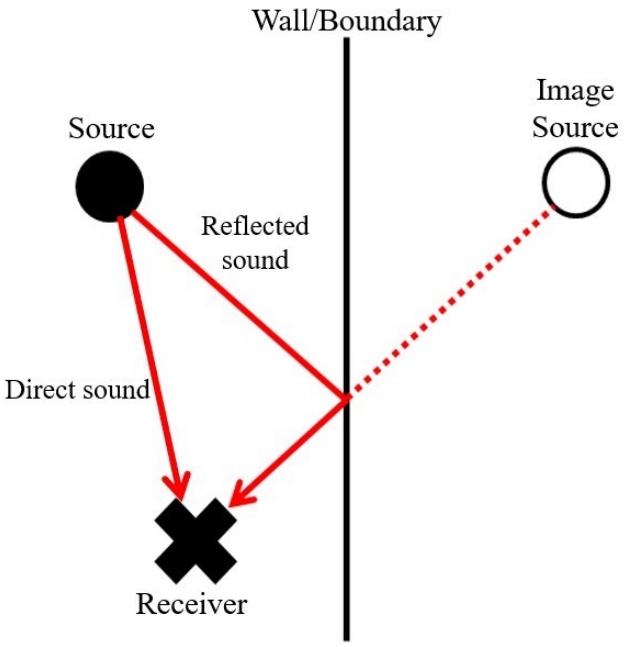

FIGURE 1.5: Example of the image source method of creating an impulse response for a room by assuming the reflection is actually an attenuated signal arriving from an image source.

To account for these empirical results, a paper by Patchett *et al.*[40] used a different method of computationally calculating IRs, called the modal summation modeling method. In the modal summation method, the pressure at a receiver position due to a source placed in the room is calculated for frequencies ranging from 500-15,000 Hz in 0.25 Hz increments. Each of these frequencies is capable of exciting several modes within the chamber, and the pressure contribution of each mode at each frequency is summed and stored as a vector of pressure versus frequency. This vector is the frequency response, or transfer function, of the room for the specific source and receiver locations (see Fig. 1.6 (a)). By taking an inverse fast Fourier transform of the transfer response, the IR of the chamber is produced (see Fig. 1.6 (b)). This new IR accounts for all forms of spatial and modal responses in the chamber by including a generalized damping term that

incorporates the frequency dependent reverberation time for the space. As such, when the autocorrelation of the modal summation IR is computed, it produces focus signals with amplitudes that more closely fit the experimental results when focusing near boundaries (see Fig. 1.6 (c)). This method, and its results, are given in greater detail in Chapter 2 of this dissertation.

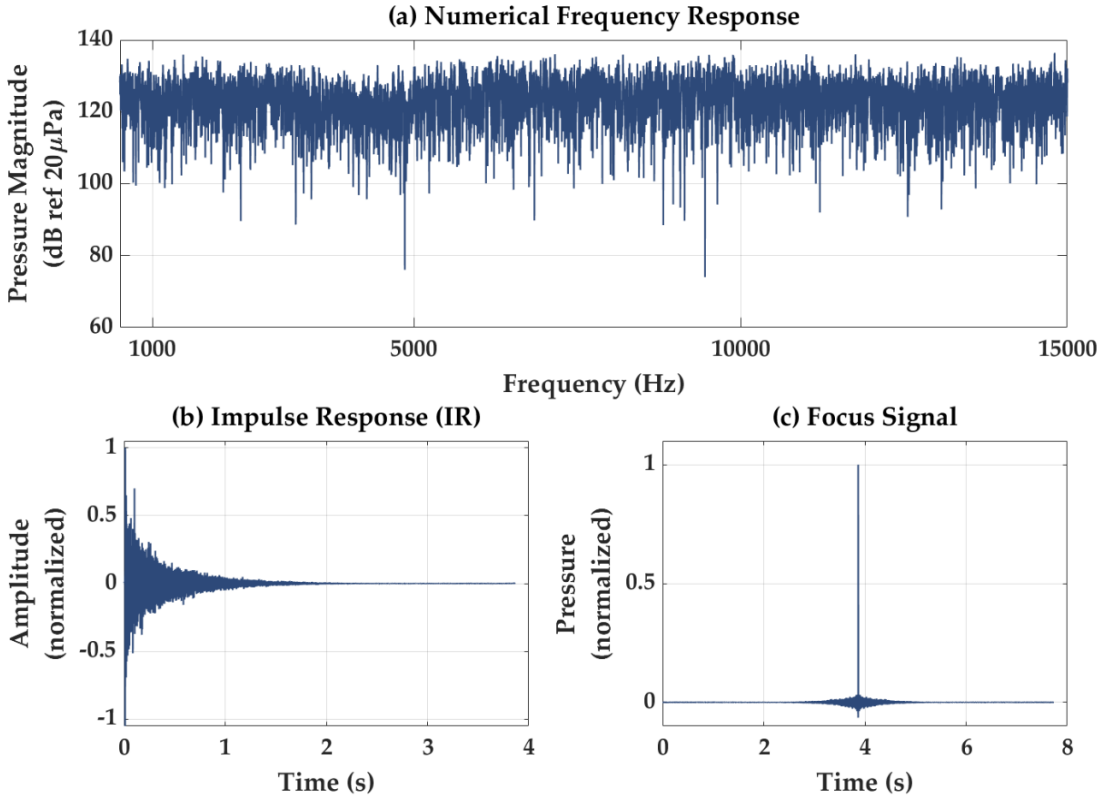

FIGURE 1.6: (a) The numerical frequency response function generated by the modal summation model method. (b) The impulse response created by taking an inverse fast-Fourier transform of the frequency response function. (c) The focus signal created by auto-correlating the impulse response.

1.5 Outline of Dissertation

This dissertation covers an investigation into high-amplitude focus signal generation in highly reverberant environments and includes aspects of nonlinear wave characteristics, multiple modeling methods, and a series of experiments meant to test the hypothesis about the mechanisms that generate the specific features seen in high-amplitude acoustic focusing.

Chapter 2 is a peer reviewed published article that discusses, in detail, a study of the spatial effects of receiver placement (focal location) in both the large and small reverberation chambers at Brigham Young University. This study combines empirical and computational results that are in very close agreement, showing that the Cartesian position of a receiver can have a dramatic effect on the peak focus pressure measured at a given location in the chamber. It also confirms the results, both computationally and empirically, previously found by Denison and Anderson's[36] model that the size of a given environment can have a significant effect on the peak focus pressure. Kingsley contributed to this publication by assisting in the development of the computational model, primarily by helping vectorize, implement GPU processing, and develop methods of speeding up the computational process.

An additional peer-reviewed and published article appears in Chapter 3. It contains an analysis of the nonlinear characteristics observed in high-amplitude focusing studied in greater detail, and a hypothesis is given as to how these characteristics may be generated. An experiment is conducted to test this hypothesis, and the resulting data are shown to justify the hypothesis.

A model of nonlinear wave interaction comprises Chapter 4. This model, made with the open-source MATLAB© software named k-Wave©, is used to demonstrate that high amplitude pressure waves propagating through the air can in fact overlap to form free-space Mach stems. This result supports the hypothesis that underlies the majority of the work put forth in this

dissertation: The coalescence of high-pressure Mach waves creates an effective Mach stem region where the waves overlap and interact with each other to generate a higher-than-expected peak focus pressure at the receiver.

The dissertation then concludes with Chapter 5, which is a summary of the work completed and the conclusions, followed by an outline of current and future studies that could further this research into the nonlinear characteristics of high-amplitude focusing using TR.

Appendix A contains a published peer-reviewed article in which the author of this dissertation was a contributing author. This paper, authored by Willardson *et al*.[41], laid the groundwork for the research done in this dissertation, as the first signs of slight nonlinear deviations were initially observed by this group. Appendix B contains an additional peer reviewed paper, authored by Furlong *et al.*[39], that the author contributed to by generating a large amount of experimental data for a comparison of TR to active noise control (ANC) systems. Appendix C is the modal summation modeling MATLAB© code used in Chapter 2 to verify the experimental findings. Finally, Appendix D contains all of the MATLAB© code used for the k-Wave© modeling in Chapter 4, along with a brief description of how to properly place your elements when using k-Wave©.

Chapter 2

The Impact of Room Location on Time Reversal Focusing Amplitudes

2.1 Introduction

The following chapter is a peer-reviewed published journal article that is published in the Journal of the Acoustical Society of America. In this paper, I was able to create a MATLAB© script using a well-known equation for modal summation in a room and adapt it to model the time-reversal process. This model generated data that closely matched the experimental phenomenon recorded when focusing at various positions in the reverberation chambers at Brigham Young University. Previous attempts at modeling the experiments using the traditional image source method had not been successful at reproducing the experimental results. This paper was a step forward in modeling methodology and verification and has provided additional insight into the physics of time-reversal in highly reverberant environments. It has also helped to move the research forward by providing a new means to study and verify phenomena that had proved difficult in the past. The script has found wide use in our research group and is currently being used to model various phenomena not related to its original use. Coauthor Adam Kingsley's contribution to this work consisted of helping to rewrite the original version of the script to reduce the computation time. Specifically, he and I worked on including CPU and GPU processing techniques together, as well as vectorization that cut the processing time down by about eighty percent. The code used to generate this model is included as Appendix C.

2.2 Required Copyright Notice

Citation:

B. D. Patchett, B. E. Anderson, and A. D. Kingsley, “The impact of room location on time reversal focusing amplitudes,” J. Acoust. Soc. Am., **150**(2), 1424-1433 (2021).

JASA ARTICLE

The impact of room location on time reversal focusing amplitudes

Brian D. Patchett, Brian E. Anderson,[a] and Adam D. Kingsley
Acoustics Research Group, Department of Physics and Astronomy, Brigham Young University, Provo, Utah 84602, USA

ABSTRACT:
Time reversal (TR) is a signal processing technique often used to generate focusing at selected positions within reverberant environments. This study investigates the effect of the location of the focusing, with respect to the room wall boundaries, on the amplitude of the focusing and the uniformity of this amplitude when focusing at various room locations. This is done experimentally with eight sources and two reverberation chambers. The chambers are of differing dimensions and were chosen to verify the findings in different volume environments. Multiple spatial positions for the TR focusing are explored within the rooms' diffuse field, against a single wall, along a two-wall edge, and in the corners (three walls). Measurements of TR focusing at various locations within the room show that for each region of study, the peak amplitude of the focusing is quite uniform, and there is a notable and consistent increase in amplitude for each additional wall that is adjacent to the focal location. A numerical model was created to simulate the TR process in the larger reverberation chamber. This model returned results similar to those of the experiments, with spatial uniformity of focusing within the room and increases when the focusing is near adjacent walls. © *2021 Acoustical Society of America*. https://doi.org/10.1121/10.0005913

(Received 27 April 2021; revised 24 June 2021; accepted 30 July 2021; published online 25 August 2021)
[Editor: Julien de Rosny] Pages: 1424–1433

I. INTRODUCTION

Time reversal (TR) is a signal processing technique that relies on the principle of reciprocity in a given environment to generate a focused signal at a location within that environment.[1,2] This technique benefits from being performed in a reverberant environment and is often performed in one. It began as a method called matched signal processing for underwater communication[3–5] and has since branched to multiple scientific fields such as medicine,[6,7] nondestructive evaluation of materials (NDE),[8–10] and source event localization in geophysics.[11] TR has also been explored with sound in the audible range as a method of communication in complex reverberant environments[12,13] as well as common room situations.[14] Recently, TR of high-amplitude ultrasound in air was used to generate a difference frequency.[15] The focusing process is comprised of two steps, an initial forward step in which the impulse response (IR) of the environment is calculated and a backward step where the IR is reversed in time and broadcast from the initial source position [the so called reciprocal TR (Ref. 2) process]. This time reversed impulse response (TRIR) signal is then broadcast, causing energy to converge on the receiver position, resulting in impulsive focusing.

To achieve the forward step of TR, multiple sources and a single receiver are placed in a reverberation chamber. A chirp signal is broadcast from each of the source locations individually, and the chirp response (CR) of each broadcast is recorded at the receiver position. Because the IR is spatially unique for each individual source/receiver system, this step is performed consecutively for each of the eight sources alone. If the IRs were not captured consecutively, then the signal recorded at the receiver would be a mix of all eight IRs together, and they could not be separated for the backward step performed later. This also produces individual IRs with better resolution and signal-to-noise ratio than if they were all collected simultaneously. The CR is described mathematically as the convolution of the chirp signal with the IR of the reverberation chamber. Once the CRs have been recorded, the IR for each can also be calculated. Once obtained, the IR is reversed on the time axis, creating the TRIR. Each of the TRIRs is then broadcast from all sources simultaneously. Due to the reciprocal nature of the system, the emissions from the TRIRs from each source trace the same paths back through the reverberation chamber to the receiver. The result is a convergence of the signals on the receiver, generating a focus. The location of this focusing will be termed the focal location. The converging acoustic waves behave in such a way that the eight simultaneous broadcasts overlap constructively and add collectively to the focusing amplitude. The amplitudes are such that linearity can be assumed in each individual chirp broadcast, but during the backward step the amplitude of the converging waves near the focal location is large enough that nonlinear phenomena occur. In the medical field, a similar TR technique is employed to both locate and destroy kidney stones in a technique known as lithotripsy.[7,16] Scientists studying NDE have employed this method of TR in solids to evaluate damage to a material through vibrational excitation of the material using a TR generated focus in this same way.[9,10]

The first studies applying TR to room acoustics focused primarily on communication in reverberant environments

[a]Electronic mail: bea@byu.edu, ORCID: 0000-0003-0089-1715.

with complex structures. Candy *et al.*[12,13] studied the application of TR communication in highly reverberant environments. They found that communication quality could be improved through the use of multiple sources and a linear equalization filter. In a subsequent study, Ribay *et al.*[17] applied a room acoustics model, based on work by Draeger and Fink[18] and Derode *et al.*[19] using TR in solid materials, to show that focal amplitudes are dependent upon the number of sources present, the reverberation time (RT_{60}) of the environment, and the bandwidth of the IR. Additionally, Yon *et al.*[14] performed an experimental study in a standard room (non-reverberation/non-anechoic), finding that TR produces temporal and spatial focusing that is better than time-delay beamforming. This is due to multiple sound paths between the sound sources and focus location. It was also found that increasing the number of sources while simultaneously increasing the bandwidth of the IR decreases the level of the side lobes, resulting in improved focusing. Those experiments were done with a linear 20-loudspeaker array and a single microphone mounted to a liner scanning system. This allowed the group to measure the focus both spatially and temporally. A numerical and experimental study recently conducted by Denison and Anderson[20,21] was able to show through similar modeling techniques that changes in RT_{60} due to changes in the volume of the room affect the amplitude of the focus differently than do changes to absorption. Increasing the volume of a reverberant environment (thereby increasing RT_{60}) with similar boundary conditions (wall absorption) leads to a decrease in peak focal amplitudes when all other variables remain constant. They were also able to show a direct connection between the RT_{60} of a room and the performance of the TR focusing, demonstrating that a longer RT_{60} reduced the spatial side lobes that are characteristic to TR focusing. Their experimental work was done in a reverberation chamber, where absorbers were used to tailor the RT_{60} to study the effect on the focus signal. Ribay *et al.*[17] limited their study to changes in RT_{60} due to changes in absorption (they did not explore the impact of room volume). Denison and Anderson verified the work of Ribay *et al.*, while also studying the impact of a changing volume. However, Denison and Andersons' experimental verifications of the increased volume effect were limited to non-ideal environments. These effects have not been studied or verified in reverberation chambers until now. Experimental work performed by Ma *et al.*[22] found that when using metamaterial objects known as acoustic prisons, they were able to increase the peak focus intensity when additional reverberating surfaces were included inside of the prison objects. Additional work by Ma *et al.*[23] used a set of loudspeakers with a microphone and reported findings similar to those discussed above, primarily that chirp bandwidth, chirp time duration, and RT_{60} all affect the focus in a meaningful way.

Previous studies have not explored the impact of the TR focal location's position within a room (i.e., near walls or away from walls and what level of consistency is found when away from walls) on the TR focusing amplitude. The purpose of this paper is to apply the TR process experimentally in two different reverberation chambers, along with numerical modeling of TR in a reverberation chamber, to show how the TR focusing amplitude depends on the focal location within a room. Reliable prediction of an expected focus amplitude at a given position within the environment relative to reflecting surfaces is necessary when applications involve using TR to deliver energy to that position. Resulting data show that the amplitude increases by moving the focal location from a diffuse field position (away from all walls/surfaces) to a position adjacent to one reflecting wall by approximately 3 dB. In this paper, the word "wall" will be used to refer to any of the four walls, the ceiling, or the floor. It increases again near a two-wall edge and again in the corner of the room where three walls are adjacent to the focal location. The increase in amplitude for diffuse sound in a room is well known to be a 6 dB increase with each additional reflecting surface. A mathematical description of the TR process is performed in Sec. V, confirming that the resulting increases should also be on the order of 6 dB, and a reason why they are not that high in both the experiment and the model is given. The amplitude of the focusing is also quite uniform when the focal location is placed anywhere within the diffuse field of the room. This is in contrast to the expected outcome for diffuse sound fields in rooms, where one standard deviation away from the mean of the level can be expected to vary by as much as +5/–6 dB.[24] The volume of the room has a significant effect on the amplitude as well, confirming the results obtained by Denison *et al.*[20] The measurements taken in the small reverberation chamber (SRC) were consistently higher than those taken in the large reverberation chamber (LRC) when using the same configuration and output settings.

It is worth noting that the peak sound pressure levels (SPLs) attained in the experiments presented here were on the order of 150–160 dB. These are only peak levels of a short duration focal event, but these levels are considerably high. Applications for these levels include the investigation of high amplitude sound acting on rigid bodies, testing of hearing protection at high amplitudes, and use as a tool to study nonlinear sound propagation. The work of Willardson *et al.*[25] showed that nonlinear effects can begin to cause distortion in the TR focusing when the peak levels exceed about 160 dB. Thus, we assume that the peak levels reported here are within the linear regime.

II. EXPERIMENTAL DETAILS

A. Setup

The experiments were conducted in two separate reverberation chambers. The two chambers were chosen because they differ in volume but have similar construction. The walls, floors, and ceilings are composed of the same materials and treatment from one chamber to the next. And there are diffuser panels of similar material suspended in each. Dimensions of the SRC are 5.70 m × 4.30 m × 2.50 m, with a volume of 61.3 m^3. The SRC has an overall RT_{60} of 4.2 s,

with a Schroeder frequency of 522 Hz. The LRC measures 4.96 m × 5.89 m × 6.98 m, with a volume of 204 m^3, an overall RT_{60} of 7.6 s averaged across the frequency spectrum of the input signal,[26] and a Schroeder frequency of 410 Hz.[27] A GRAS (Holte, Denmark) 40BE free-field microphone with a 26CB preamplifier is used as the receiver (referred to as a microphone in this section) with a GRAS 12AX power module. BMS (Hannover, Germany) 4590 dual diaphragm high output loudspeakers fitted with original equipment manufacturer (OEM) crossovers and horns are utilized as the sources (referred to as loudspeakers in this section). It was found by Anderson *et al.* that directionality of sources has a destructive effect on the focus amplitude when the sources are pointed at the focal location and that facing the sources away from the focal location serves to increase the focus amplitude.[28] As such, these loudspeakers are placed near the walls in the room and oriented in such a way as to be facing away from the focal location (microphone position) (see Fig. 1). Two four-channel Crown (Stamford, CT) CT4150 amplifiers are used to provide power to the loudspeakers. All signals are generated and processed for TR using a custom in-house LabVIEW™ interface, coupled with two Spectrum (Grosshansdorf, Germany) M2i.6022 signal generation cards and an M2i.4931 digitizer card. All post-processing is handled in MATLAB™.

To begin, a logarithmic chirp signal with a bandwidth of 500–15 000 Hz is broadcast from a single loudspeaker, and the CR is recorded at the microphone position. In initial trials, the use of a logarithmically swept chirp signal produced a higher amplitude focus than a linear chirp signal. It was found by Willardson *et al.* that extending the bandwidth beyond 500–7500 Hz had a negligible effect on the peak amplitude of the focus in the LRC environment.[25] However, the Willardson study was limited in that the equipment only had the capability of reaching 9500 Hz. The drivers used in the current study have been upgraded with OEM crossovers, allowing for frequencies up to 15 000 Hz. Since the objective of this study, in part, is to produce a focus with a high signal-to-noise ratio, the decision to extend the bandwidth to the full flat frequency response capability of the driver (500–15 000 Hz) was made in order to capture the most possible energy from the focusing sound field.

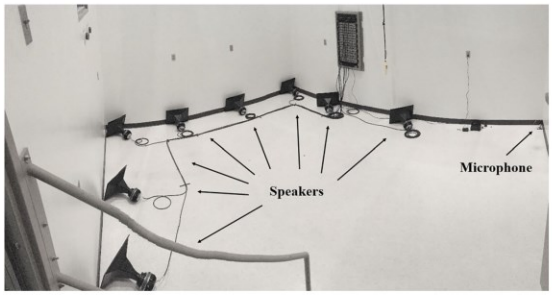

FIG. 1. (Color online) Photograph of the experimental layout in the LRC. The room is a rectangular room with parallel walls, along with reflecting panels (not shown in the image) intended to make the sound field more diffuse. Distortion in the image is due to the panoramic nature of the photograph.

An IR for this loudspeaker and microphone combination is then calculated using a cross correlation of the chirp with the CR[28,29] and stored for that loudspeaker channel. This is repeated for each loudspeaker-microphone combination to acquire eight individual IRs. The IRs are then reversed in time to create a set of eight TRIRs, at which point TRIRs are broadcast simultaneously from each of their respective loudspeakers (see Fig. 2). Each IR has a sampling frequency of 250 kHz for the entire process. The high sampling frequency ensures that the peak amplitude of the focusing is captured with high accuracy.

The TR process time aligns the convergence of multiple arrivals of sound to achieve constructive interference in the form of high amplitude focusing of sound at the microphone location. The use of software synchronization of the broadcasts from multiple loudspeakers generates a higher amplitude focus than a single loudspeaker would when used alone. This full TR process is repeated at various spatial positions within the room in this study to explore the dependence of the TR focusing amplitude with respect to the spatial location of that focusing within the room. All measurements are made assuming linearity both acoustically and in terms of the operating limits of the equipment used. Even though the focus amplitude peaks have levels of around 150 dB, linear scaling of the focusing is observed using different amplification levels.[24]

B. Spatial position measurements

One aim of creating a diffuse field in room acoustics is to provide uniform SPLs measured at any location within that diffuse field. However, in Fig. 2.17(a) of Kleiner and Tichy[24] and in Fig. 3.8 of Kuttruff,[30] it is demonstrated that the pressure values measured across a diffuse field in a reverberant room can vary by greater than ±10 dB for a given frequency as a measurement receiver is moved across the space. Kleiner and Tichy quantified the variation by stating, "The logarithmic representation of twice the variance that contains 70% of the sound amplitudes is (nonsymmetrically) within 11 dB…".[24] In other words, 70% of the pressure fluctuations can be within +5 or −6 dB above and below the mean value (one standard deviation above and below the mean).

This variation is due to modal overlapping throughout the space, even though the frequency range may be above the Schroeder frequency.[31] It is therefore interesting to investigate how the amplitude of TR focusing varies across the diffuse field region of a room and how the proximity of the focal location to walls impacts the amplitude of the focusing. It may be of interest to know how much uncertainty in the focusing amplitude one might expect when using TR to focus sound to a given location within a room. Throughout these measurements, it is useful to keep in mind that the focal location is changed by moving the microphone to different locations in the room, while keeping the

JASA
https://doi.org/10.1121/10.0005913

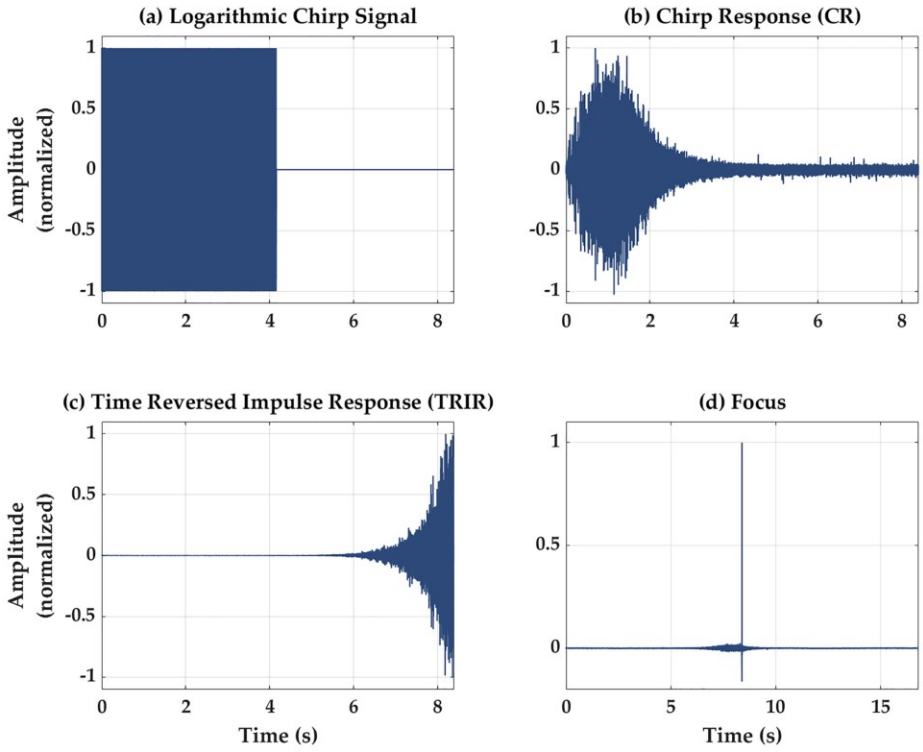

FIG. 2. (Color online) example signals used in the TR experiments. (a) The logarithmic chirp signal, 4.16 s in length. (b) The CR recorded in the forward process at the microphone. (c) The normalized TRIR. (d) Focus generated by simultaneous broadcast of eight loudspeakers. All amplitudes in this figure are normalized for clarity in display.

loudspeakers' locations fixed, and redoing a full TR experiment at the new microphone location (both forward and backward steps).

The various focal locations explored here include four different types of locations, with focal locations of similar types being referred to as regions: the open space (diffuse field region) of the room, against one of the reflecting walls (wall region), against two of the reflecting walls (edge region), and against three walls of the room (corner region). The diffuse field position measurements are made in accordance with the ISO standard,[32] where a diffuse field is defined as occurring at least 1 m from any reflecting wall. A total of 20 diffuse field focal locations are chosen at random, while ensuring that the focal location is at least 1 m from any of the reflecting walls in the room (see Fig. 3). The single wall measurements are made at six random positions against one of the reflecting walls in the room. Care is taken to ensure that the focal location remains more than 1 m from any other adjacent wall. The edge region measurements are made at six locations in the room. Again, care is taken to keep the focal location at least 1 m away from the corners of the room. For practical purposes, only four corner measurements are made due to the geometry of the rooms and the difficulty in reaching the upper corners reliably with the microphone. In the one- and two-wall region measurements,

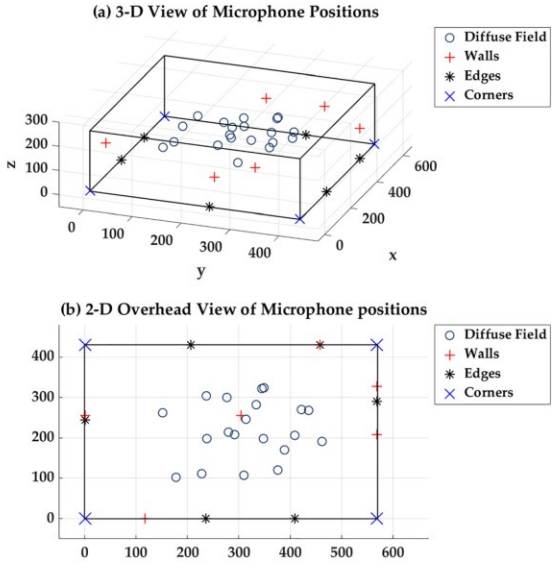

FIG. 3. (Color online) Microphone positions in the SRC. Each position region is denoted with a unique character. (a) Three-dimensional (3-D) representation of positions. (b) Top-down view of the chamber in two dimensions (2-D).

the microphone is placed 1 cm from any wall for consistency in positioning. The body of the microphone is oriented so that it is parallel to the walls. In the case of the corner measurements, the microphone is pointed directly into the corner, 1 cm from its apex, with an equal angular alignment from each wall. Measurements are performed in both the SRC and LRC to compare results for both environments.

Figure 4 illustrates the focal amplitude measurements with a bar graph in decibels (peak SPLs). This figure shows clearly that the position of the focal location in proximity to additional walls has a consistent effect of increasing the focusing amplitude. It is also worth noting that the focusing amplitude in each particular region has very little variance from the mean SPL. This indicates that there is a fair amount of uniformity of the focusing amplitude at various focal locations within the same region, especially when compared to the greater than ±10 dB fluctuations that can be expected when moving a microphone to various locations within a diffuse field without using TR. This means that one can reliably expect a certain focal amplitude irrespective of where they choose to focus sound with TR within a given region of the room.

The mean values in Fig. 4 were calculated using the squared pressure values, as this accurately represents the energy relation to the peak focal amplitude values in the sound field. Standard deviations were measured as 150.5 dB (+0.5/–0.5 dB) in the diffuse field, 153.6 dB (+0.8/–1.0 dB) against one wall, 155.7 dB (+0.9/–1.0 dB) against an edge (two walls), and 158.7 dB (+0.7/–0.8 dB) for the corners (three walls), where the values in the parentheses represent one deviation above and below the mean pressure value. As is evident in the mean values reported, the average focusing amplitude for a focal location near a wall increases by 3.1 dB (+0.6/–0.7 dB) from the diffuse field focal locations. The average increases again by 2.1 dB (+0.7/–0.8 dB) when the focal location is placed near an edge (two walls) compared to one-wall focal locations. Corner locations (three walls) again increase the focusing amplitudes by 3.0 dB (+0.6/–0.7 dB) relative to an edge (two walls).

The variation of the focal locations for TR experiments conducted in the SRC is now similarly conducted in the LRC. All signal settings, gain values, and signal processing are identical to those used in the SRC experiments to ensure a direct comparison between the two rooms of different volumes. The set of measurements made in the LRC also serves to confirm that the results from the SRC may be expected in other similar rooms and allows for comparison of the focusing amplitudes in two similar rooms of different volumes. Figure 5 shows the microphone positions used to measure peak focal amplitudes in the LRC, while Fig. 6 shows a similar bar graph as Fig. 4, but now for values measured in the LRC.

A similar uniformity is observed in the LRC measurements as was observed in the SRC measurements for each region of locations. The mean value (and one standard deviation above/below the mean) was measured to be 147.7 dB (+1.0/–1.4 dB) in the diffuse field, 151.5 dB (+0.4/–0.5 dB) against one wall, 153.7 dB (+0.7/–0.8 dB) against an edge (two walls), and 156.1 dB (+0.5/–0.6 dB) for the corners (three walls). Here, the mean diffuse field peak focal amplitude increases by 3.8 dB (+1.0/–1.2 dB). Moving to an edge, the mean increases by 2.2 dB (+1.0/–1.2 dB). Moving from an edge to a corner, the mean increases by 2.4 dB (+0.9/–1.1 dB). According to the experimental data, the SRC consistently yields higher focusing amplitudes regardless of the type of location within the room. For example, the focusing amplitude at SRC diffuse field focal locations is consistently higher than the focusing amplitude at LRC diffuse field focal locations. This agrees with the finding of Denison *et al.*[20] that, when all other experimental characteristics are kept the same, the smaller volume room will have a higher TR focusing amplitude. Figure 7 shows a comparison of the

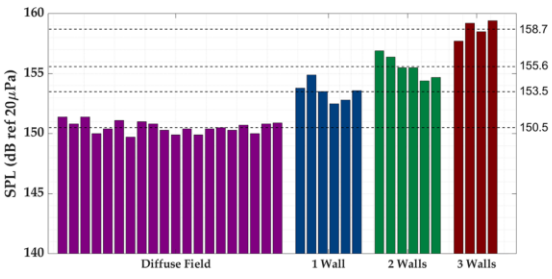

FIG. 4. (Color online) Bar graph display of measured peak SPL for various TR experiments done at the locations specified in Fig. 3 for the SRC. The mean of the peak SPL values for each region is displayed as a dashed line with mean value label to the right.

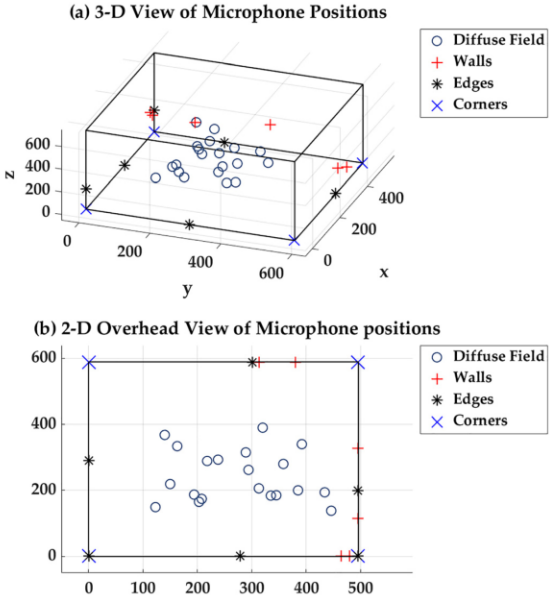

FIG. 5. (Color online) Microphone positions in the LRC. Each position region is denoted with a unique character. (a) 3-D representation of positions. (b) Top-down view of the chamber in 2-D.

https://doi.org/10.1121/10.0005913

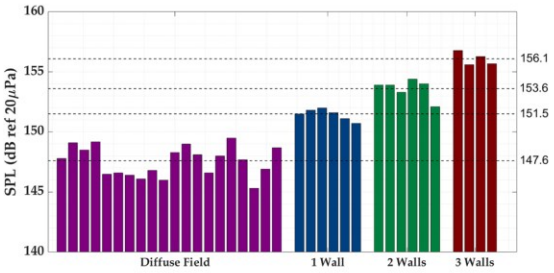

FIG. 6. (Color online) Bar graph display of measured peak SPL for various TR experiments done at the locations specified in Fig. 5 for the LRC. The mean of the peak SPL values for each region is displayed as a dashed line with mean value label to the right.

averaged focal signals measured at the focal locations in the SRC and LRC (averaged across the focal locations within a given region for a given room). This illustrates that the increase in peak focal amplitudes is consistent for the measurements performed in the SRC versus the LRC.

III. NUMERICAL MODEL OF EXPERIMENT

A numerical model was generated to compare the experimental results obtained in the LRC to theory. The model is based on a modal summation equation given by Kleiner and Tichy.[24] This form of modal summation as a way to model TR differs from both Denison and Anderson[20,21] and Ribay *et al.*,[17] who each used models based on geometric ray tracing and image sources. Denison and Anderson[20] used an image source model of TR in a room, and though they did not report this in their paper, they did not observe an increase

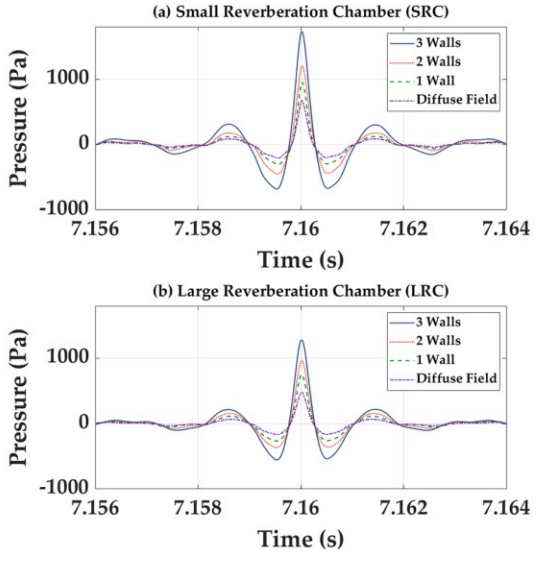

FIG. 7. (Color online) Average focal signals shown zoomed in on the time axis. (a) Comparison of the mean focal signals for each region in the SRC; (b) the same for the LRC.

in TR focusing amplitude when focusing near walls in their model. As such, a new method that incorporated the summation of pressure contributions from each excited mode in the reverberation chamber was deemed appropriate in an attempt to match observed experimental results. The model here assumes a rectangular room with parallel walls. The presence of diffusors is not factored into the calculation, though they are present in the experimental reverberation chambers.

The equation describes the pressure, $\hat{p}$, at receiver position (x, y, z) due to any given source position, (x_0, y_0, z_0), as a function of frequency or wavenumber, k, in a 3-D environment. It is a frequency response between the source and receiver locations,

$$\hat{p}(x,y,z,k) = -4\pi \frac{A}{V} \sum_{n=0}^{\infty} \frac{\Psi_n(x_0,y_0,z_0)\Psi_n(x,y,z)}{\left(k^2 - k_n^2 - j2k_n\frac{\delta_n}{c}\right)\Lambda_n}, \quad (1)$$

where A is the monopole amplitude related to the source strength (or volume velocity), Q, used in the original equation through the relationship,

$$A = \frac{j\rho_0 ckQ}{4\pi}, \quad (2)$$

V is the room volume $(204\,\mathrm{m}^3)$, n is the mode number, Ψ_n is the spatial dependence of the n th mode, k_n is the wavenumber for the n th mode, and δ_n is the damping factor. Λ_n is the function that accounts for orthogonality such that

$$\Lambda_n = \frac{1}{\varepsilon_{n_x}\varepsilon_{n_y}\varepsilon_{n_z}} \quad \text{and} \quad \varepsilon_{n_x,n_y,n_z} = \left\{ \begin{matrix} 1, \text{ for } n_x, n_y, n_z = 0 \\ 2, \text{ for } n_x, n_y, n_z = 1 \end{matrix} \right\}, \quad (3)$$

where $\varepsilon_{n_x,n_y,n_z}$ represents the Neumann orthogonality factor for the three Cartesian spatial dimensions. Λ_n can have values of $1/2$ (for axial modes), $1/4$ (for tangential modes), and $1/8$ (for oblique modes). Since the primary purpose of this analysis was the comparison of focal amplitudes obtained at different regions of the room, the amplitude, A, of the source was set to a value of 1 in Eq. (1), resulting in a Green's function. The source output levels can be arbitrary in magnitude since linearity is assumed and only relative increases in focal amplitudes are of interest as they pertain to the focal location region in which they are calculated (diffuse field, wall region, etc.).

The model implies that for a given k, the modal response due to the source position, $\Psi_n(x_0, y_0, z_0)$, and due to the receiver position, $\Psi_n(x, y, z)$, is determined from a summation of an infinite number of normal modes of the room. For the rigid walled room being modeled, with dimensions $L_x = 4.96\,\mathrm{m}$, $L_y = 5.89\,\mathrm{m}$, $L_z = 6.98\,\mathrm{m}$, the eigenfunction can be written as $\Psi_n(x,y,z) = \cos(n_x\pi x/L_x)\cos(n_y\pi y/L_y)\cos(n_z\pi z/L_z)$. As an infinite number of modes would lead to an infinite computation time, only modes whose modal frequencies lie within the bandwidth of 500–15 000 Hz were used, as this is the same bandwidth of

the chirp used in the experimental data. The modal frequency bandwidth, $\Delta f = 2.2/\mathrm{RT}_{60}$ [see Eq. (3.43) of Ref. 30], was calculated for the lowest frequency of the chirp (with the longest RT_{60}) and determined to be 0.44 Hz. Thus, a spacing less than that of $\Delta f = 0.44$ Hz was selected to make sure that every mode would be sampled at this frequency resolution. This means that the calculation for the pressure at each position used a wavenumber value of $k = 2\pi f/c$, where k ranged from $f = 500.25$ Hz to $f = 15\,000$ Hz in steps of 0.25 Hz. This resulted in 60 000 values of k for each spatial position. Given the maximum frequency used, the number of modes summed for each value of k is approximately 7.1×10^7. While it is possible to limit the number of modes in the summation by including only those with a significant contribution to the pressure amplitude (such as only summing the modes within a certain number of modal bandwidths of a given k), this calculation included all available modes. The damping factor,

$$\delta_n = \frac{6.91}{(\mathrm{RT}_{60})_{f_n}}, \tag{4}$$

is calculated from frequency-dependent, experimentally obtained RT_{60} values.[30] The frequency-dependent $(\mathrm{RT}_{60})_{f_n}$ is calculated using reverse Schroeder integration (RSI) on the IRs measured in the LRC.[33] This ensures that the model has a RT_{60} (and a subsequent δ_n) that matches the experimental values as closely as possible. Before applying the RSI, each IR was filtered using a one-third octave band filter to find the RT_{60} as a function of frequency. The one-third octave values were then linearly interpolated to represent an approximation of the RT_{60} over all discrete frequencies at a resolution of 0.25 Hz, which is the frequency spacing of the model variable f_n. The δ_n values are computed from the extracted values of $(\mathrm{RT}_{60})_{f_n}$. This 0.25 Hz resolution was empirically determined to be sufficient. During post-processing, $(\mathrm{RT}_{60})_{f_n}$ values were extracted from numerically generated IRs using the RSI method again. This analysis returned $(\mathrm{RT}_{60})_{f_n}$ values matching the input $(\mathrm{RT}_{60})_{f_n}$ values, indicating that Eq. (4) generates a numerical IR that closely matches the experimentally measured IR.

Due to the quantity of the calculations required for this modeling approach and the size of the data stored in random access memory (RAM) as the pressure is calculated, Eq. (1) is computationally broken down into several pieces and then reassembled for a final calculation (parallelization of the code). This method reduces computation time to one-third of the original time as compared to a non-parallelized version of the code. The k_n^2 and k_n values in the denominator are calculated in a standard "for" loop nested for each physical dimension. Then the product of the eigenfunctions in the numerator is calculated in a parallelized "for" loop (parfor function in MATLAB™) for each index value of x, y, and z. Finally, all of the pieces are brought together into the final form of Eq. (1). The solution for each n value and the summation is computed using the graphical processing unit. The array of pressures at each mode is then summed for each k value and saved as a pressure versus frequency spectrum. This is repeated for each receiver position, $\Psi_n(x, y, z)$, of interest.

A post-processing modification to the output pressures of the model is used to simulate the experimental use of a logarithmic chirp weighting to the input signal. The weighting was determined by applying a low pass filter with a logarithmic frequency roll-off for the 500–15 000 Hz frequency bandwidth and then determining the appropriate filter values through a curve fit. To simulate a TR focusing of energy, an inverse fast Fourier transform is calculated with the pressure versus frequency vector output from Eq. (1), producing an IR from the numerical model. An autocorrelation of the numerical IR is used to produce a focal signal like that found using standard experimental TR for the given pressure spectrum at that position.[34] The application of autocorrelation on the numerical IR ensures that a central data point is always at the exact time for peak of the focus signal, producing a highly accurate value of peak focal amplitude. Because the maximum frequency is 15 kHz, a sampling frequency of 30 kHz is assumed for all focus generation with the numerical data. Example spectra and signals at each step in this simulation of TR can be seen in Fig. 8.

It is worth pointing out that Eq. (1) is the same equation used by Kleiner and Tichy[24] to determine the fluctuations in pressure found within a diffuse field. Due to the computational nature of this work, many more focal locations were included in this numerical analysis than were used experimentally. A total of 18 randomized focal locations in each region were selected except for the corners, where seven focal locations were selected. A single source was used in the model for simplicity and economical use of computation time. Its location was chosen to be the lower corner of the numerical "room," opposite the majority of the measurement locations. Figure 9 depicts the source and receiver positions used as focal locations in the numerical

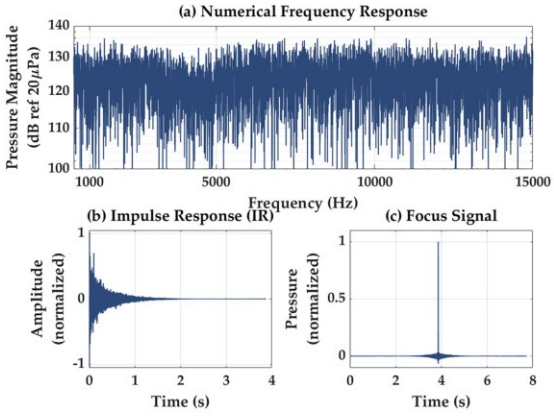

FIG. 8. (Color online) (a) An example frequency response output from the numerical model based on Eq. (1); (b) the IR found by taking an inverse fast Fourier transform of (a); (c) the focal signal generated by an autocorrelation of the IR in (b).

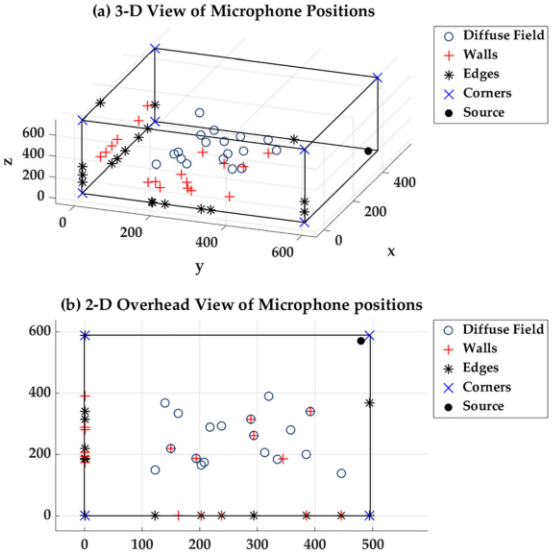

FIG. 9. (Color online) Receiver positions used in the numerical modeling. Each position region is denoted with a unique character. (a) 3-D representation of positions. (b) Top-down view of the chamber in 2-D.

calculations, and Fig. 10 shows the peak focal amplitudes obtained from the numerical model with a mean value for each region. The significance of the focal amplitude values lies in the uniformity of the focal amplitudes in each region and the difference in amplitudes from one region of focal locations to the next, as was investigated experimentally. The mean value (and one standard deviation above/below the mean) was measured to be 152.7 dB (+0.4/–0.5 dB) in the diffuse field, 155.7 dB (+0.4/–0.4 dB) against one wall, 159.1 dB (+0.2/–0.2 dB) against an edge (two walls), and 163.1 dB (+0.5/–0.6 dB) for the corners (three walls). The mean values increase by 3.0 dB (+0.3/–0.3 dB) when moving from the diffuse field to one wall, 3.4 dB (+0.2/–0.2 dB) when moving from one wall to an edge, and 4.0 dB (+0.4/–0.4 dB) when moving from the edge into a corner. The general trend of an increase in focal amplitude with the proximity to additional walls matches that seen experimentally.

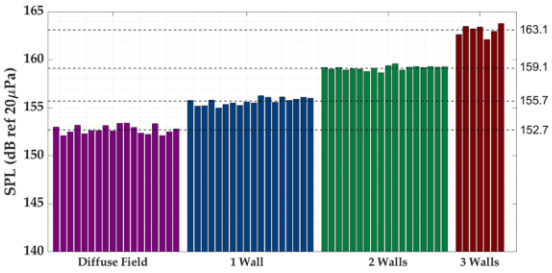

FIG. 10. (Color online) Bar graph display of measured peak SPL for various TR experiments done at the locations specified in Fig. 9 for the numerically modeled reverberation chamber. The mean of the peak SPL values for each region is displayed as a dashed line with mean value label to the right.

Numerical modeling was also conducted without using the previously mentioned filter that simulates the use of logarithmic chirp to see if this filter impacts the modeling results. The use of this filter to simulate the logarithmic chirp showed no significant change in the peak focal amplitudes generated by the model.

IV. COMPARISON OF NUMERICAL TO EXPERIMENTAL RESULTS

Table I provides a comparison summary of the two sets of experimental results in the SRC and in the LRC along with numerical results in the LRC. The comparison clearly shows that increasing the number of reflecting surfaces (walls) near the focal location consistently raises the value of the focus amplitude near an average of ≈3 dB per additional surface (to within the given standard deviation of each region). It is especially worth noting the overall uniformity of each region. Both of the experimental cases as well as the numerical case showed uniformity to within a very small deviation from the mean. This deviation was smallest in the numerical model, which is to be expected given the idealization of the algorithm's "environment" (virtual space generated for calculation) when compared to the potential for systematic and random error in real world experimentation.

Variation in the increases (meaning comparing the 3.8 dB increase in the experimental LRC results to the 3.1 dB increase in the experimental SRC results to the 3.0 dB increase observed in the numerical LRC results when moving from the diffuse field region to the one-wall region) in average focal amplitude value from one focal location region to the next could be caused by multiple things. The loudspeakers used in the experiments are placed near walls, with the horn openings facing the wall, close enough that there could be a frequency-dependent change in the radiation from the source that is not seen in the numerical model (the model assumes sources with flat frequency responses). It is also worth noting that omnidirectional sources are assumed in the numerical model, whereas the experimental ones are directional. Because the experimental loudspeakers are directional, they were pointed away from the receiver to avoid the large direct path arrival relative to the other arrivals in the IR as suggested by Anderson *et al.*[26] The rooms used for experiments also had diffusor panels hung in them, whereas the numerical model assumed an empty rectangular room. Also, the number of sources used in the modeling was decreased to one to simplify the calculation. These exceptions aside, the increasing nature of the focal amplitude in each focal location region is consistent, and similar trends are seen in the experimental results and the numerical simulations.

V. THEORETICAL IMPACT OF WALL PROXIMITY ON FOCAL AMPLITUDE

Recall from Sec. III that traditional TR can be modeled as an autocorrelation of the IR. This is the equivalent to multiplying Eq. (1) by its complex conjugate to compute the auto-spectrum. The equation can be simplified by

https://doi.org/10.1121/10.0005913 JASA

TABLE I. Comparison of the average results for the increase in focal amplitude when the focal location is moved from one focal location region to the next (adding a wall each time) in each of the reverberation chambers as well as the numerical results. Values shown represent peak SPLs in decibels (ref 20 μPa). The average values for one-wall locations are given relative to the average diffuse field location values. The values for edge locations are given relative to the average one-wall values. The values for corner locations are given relative to the average edge location values. Values in parentheses represent one standard deviation above and below the mean pressure value given.

Focal location	Experimental LRC	Experimental SRC	Numerical LRC
Diffuse field	0.0 dB (+1.0/−1.4 dB)	0.0 dB (+0.5/−0.5 dB)	0.0 dB (+0.4/−0.5 dB)
Wall	+3.8 dB (+1.0/−1.2 dB)	+3.1 dB (+0.6/−0.7 dB)	+3.0 dB (+0.3/−0.3 dB)
Edge	+2.2 dB (+1.0/−1.2 dB)	+2.1 dB (+0.7/−0.8 dB)	+3.4 dB (+0.2/−0.2 dB)
Corner	+2.4 dB (+0.9/−1.1 dB)	+3.0 dB (+0.6/−0.7 dB)	+4.0 dB (+0.4/−0.4 dB)

condensing all of the terms not associated with the eigenfunctions into a single variable A_n,

$$A_n = \frac{\left(k^2 - k_n^2 - j2k_n\frac{\delta_n}{c}\right)\Lambda_n}{-jk\rho_0 cQ/V}. \tag{5}$$

An auto-spectrum can then be represented by the product of the original summation with its complex conjugate,

$$y(r_0, r, k) = \sum_{n=0}^{\infty}\frac{G_n(r_0, r)}{A_n}\cdot\sum_{n=0}^{\infty}\frac{G_n(r_0, r)}{A_n^*}, \tag{6}$$

where $G_n(r_0, r)$ represents the product of the eigenfunctions $\Psi_n(x_0, y_0, z_0)\Psi_n(x, y, z)$ and in the case of a rigid walled room is a real quantity. This product of summations can then be expanded as

$$\begin{aligned} y(r_0,r,k) = &\left(\cdots + \frac{G_{n-1}(r_0,r)}{A_{n-1}} + \frac{G_n(r_0,r)}{A_n}\right.\\ &\left. + \frac{G_{n+1}(r_0,r)}{A_{n+1}} + \cdots\right)\cdot\left(\cdots + \frac{G_{n-1}(r_0,r)}{A_{n-1}^*}\right.\\ &\left. + \frac{G_n(r_0,r)}{A_n^*} + \frac{G_{n+1}(r_0,r)}{A_{n+1}^*} + \cdots\right). \end{aligned} \tag{7}$$

A careful analysis of the product of the summations allows them to be rewritten as the sum of same-indexed terms and a sum of cross-terms (where the indices are different),

$$\begin{aligned} y(r_0, r, k) = &\sum_{n=0}^{\infty}\frac{G_n(r_0, r)^2}{|A_n|^2}\\ &+ \sum_{l\neq m=0}^{\infty}\sum_{m\neq l=0}^{\infty}\frac{G_l(r_0, r)G_m(r_0, r)}{A_l A_m^*}. \end{aligned} \tag{8}$$

The pressure contribution from a single mode can be evaluated as a fixed source while the receiver is moved throughout the space. Thus, the impact on the response from each mode when having the receiver against one or more walls may be determined. For any given mode, the first summation term in Eq. (8) yields an average increase in 6 dB when the receiver position is moved from the diffuse field region to up against one wall. Another 6 dB is gained when the receiver position is placed at an edge. And again, there is another 6 dB increase when the receiver position is in the corner. The second summation term yields no average increase whether the receiver is in the diffuse field or up against any walls. Thus, when summing many modes in Eq. (8), the overall result is that a 6 dB increase should be expected when the receiver is placed exactly against each additional wall.

This analysis suggests a higher increase at the surface regions than is found both experimentally and numerically. This is likely due to the positions of the microphones being 0.01 m from the walls in both the experiments and the numerical simulation. Experimentally, this was done to avoid direct contact with the surfaces, so that mechanical vibration between the walls and the microphone would be avoided. Also, placing the microphones exactly in the corner or at an edge of a room is not possible due to the practical, finite size of microphones. The microphone positions used in the numerical calculation were mostly the same as in experiments in order to replicate the experiment as closely as possible with the numerical simulation. However, when the microphone positions are moved exactly against the walls in the simulation, the increase is 6 dB for each wall added, just as the mathematics in this section suggests.

VI. CONCLUSIONS

The results presented in this paper have shown that, using the TR process, a relative uniformity of the peak focal amplitude may be expected within a diffuse field (or when against one wall, against two walls, or against three walls). The standard deviation of the obtained focal amplitudes across each type of focal amplitude region is small. This indicates that no matter where a receiver is placed within a specific region (diffuse field, single wall, etc.), the amplitude may not fluctuate more than 1 dB. As described in Sec. II B, diffuse field theory predicts a deviation in SPL for any given frequency of up to 11 dB (+5/–6 dB above and below the mean) across a reverberant space.[23] The TR technique provides a peak focal amplitude that varies far less across a reverberant space, having a deviation of up to 1 dB (+0.5/–0.5 above and below the mean) experimentally and 0.9 dB (+0.4/–0.5 above and below the mean) in the modeling results.

The proximity of the focal location with respect to adjacent walls has a significant effect on the amplitude of a generated focus. The increase in amplitude expected when the focal location is placed exactly against each additional wall

is 6 dB. However, according to the presented experimental results, an increase in amplitude on the order of ≈3 dB per wall can be seen as the focal location is made to be adjacent to each additional wall, likely due to the practical inability to place a microphone exactly against a wall, edge, or corner of a room. This indicates that placement near three walls (in a corner of a room) produces the highest possible TR focal amplitude, approximately 9 dB higher than focal amplitudes obtained in the diffuse field. These experimental results are verified with a numerical model. This knowledge is important for the use of TR in reverberant environments.

These conclusions are based on experiments conducted in a SRC (volume 61 m^3) and in a LRC (volume 204 m^3). The full TR process (both forward and backward steps) was conducted for several different focal locations within these rooms while keeping the loudspeaker locations fixed. The focal locations included many positions away from walls in the diffuse field, near one wall, near two walls (edges of the room), and near three walls (corners of the room). A numerical model of the LRC was constructed to simulate TR in a rectangular room. The model was based on normal mode summation theory.

The size of a room also has an effect on the amplitude of the TR focusing. The facilities used in this study differed in volume by approximately a 3:1 ratio. The smaller of the two chambers produces focal amplitudes that average 2.4 dB higher for each type of focal location region. This agrees with the finding by Denison and Anderson[20] that a smaller volume room can contribute to the generation of a higher focal amplitude than a larger volume room.

ACKNOWLEDGMENTS

Funding provided by internal support from the Brigham Young University College of Physical and Mathematical Sciences is gratefully acknowledged. We thank Kevin Leete and Mylan Cook for their insight into mean and standard deviation calculations of pressure magnitudes.

[1]M. Fink, "Time reversed acoustics," Phys. Today **50**(3), 34–40 (1997).
[2]B. E. Anderson, M. Griffa, C. Larmat, T. J. Ulrich, and P. A. Johnson, "Time reversal," Acoust. Today **4**(1), 5–16 (2008).
[3]C. S. Clay and B. Anderson, "Matched signals: The beginnings of time reversal," Proc. Meet. Acoust. **12**(1), 055001 (2011).
[4]A. Parvulescu and C. S. Clay, "Reproducibility of signal transmissions in the ocean," Radio Electron. Eng. **29**(4), 223–228 (1965).
[5]H.-C. Song, "An overview of underwater time-reversal communication," IEEE J. Ocean. Eng. **41**(3), 644–655 (2016).
[6]A. Sutin and H. Salloum, "Prospective medical applications of nonlinear time reversal acoustics," Proc. Meet. Acoust. **34**(1), 020003 (2018).
[7]G. Montaldo, P. Roux, A. Derode, C. Negreira, and M. Fink, "Ultrasound shock wave generator with one-bit time reversal in a dispersive medium, application to lithotripsy," Appl. Phys. Lett. **80**, 897–899 (2002).
[8]B. E. Anderson, M. Griffa, T. J. Ulrich, P.-Y. L. Bas, R. A. Guyer, and P. A. Johnson, "Crack localization and characterization in solid media using time reversal techniques," in *Proceedings of the 44th U.S. Rock Mechanics Symposium and 5th U.S.-Canada Rock Mechanics Symposium*, Salt Lake City, UT (June 27–30, 2010), ARMA-10-154.
[9]S. M. Young, B. E. Anderson, S. M. Hogg, P.-Y. L. Bas, and M. C. Remillieux, "Nonlinearity from stress corrosion cracking as a function of chloride exposure time using the time reversed elastic nonlinearity diagnostic," J. Acoust. Soc. Am. **145**(1), 382–391 (2019).
[10]B. E. Anderson, L. Pieczonka, M. C. Remillieux, T. J. Ulrich, and P.-Y. L. Bas, "Stress corrosion crack depth investigation using the time reversed elastic nonlinearity diagnostic," J. Acoust. Soc. Am. **141**(1), EL76–EL81 (2017).
[11]C. S. Larmat, R. A. Guyer, and P. A. Johnson, "Time-reversal methods in geophysics," Phys. Today **63**(8), 31–35 (2010).
[12]J. V. Candy, D. H. Chambers, C. L. Robbins, B. L. Guidry, A. J. Poggio, F. Dowla, and C. A. Hertzog, "Wideband multichannel time-reversal processing for acoustic communications in highly reverberant environments," J. Acoust. Soc. Am. **120**(2), 838–851 (2006).
[13]J. V. Candy, A. W. Meyer, A. J. Poggio, and B. L. Guidry, "Time-reversal processing for an acoustic communications experiment in a highly reverberant environment," J. Acoust. Soc. Am. **115**(4), 1621–1631 (2004).
[14]S. Yon, M. Tanter, and M. Fink, "Sound focusing in rooms: The time-reversal approach," J. Acoust. Soc. Am. **113**(3), 1533–1543 (2003).
[15]C. B. Wallace and B. E. Anderson, "High-amplitude time reversal focusing of airborne ultrasound to generate a focused nonlinear difference frequency," J. Acoust. Soc. Am. **150**(2), 1411–1423 (2021).
[16]J.-L. Thomas, F. Wu, and M. M. Fink, "Time reversal focusing applied to lithotripsy," Ultrason. Imaging **18**(2), 106–121 (1996).
[17]G. Ribay, J. de Rosny, and M. Fink, "Time reversal of noise sources in a reverberation room," J. Acoust. Soc. Am. **117**(5), 2866–2872 (2005).
[18]C. Draeger and M. Fink, "One-channel time-reversal in chaotic cavities: Theoretical limits," J. Acoust. Soc. Am. **105**(2), 611–617 (1999).
[19]A. Derode, A. Tourin, and M. Fink, "Limits of time-reversal focusing through multiple scattering: Long-range correlation," J. Acoust. Soc. Am. **107**(6), 2987–2998 (2000).
[20]M. H. Denison and B. E. Anderson, "Time reversal acoustics applied to rooms of various reverberation times," J. Acoust. Soc. Am. **144**(6), 3055–3066 (2018).
[21]J. B. Allen and D. A. Berkley, "Image method for efficiently simulating small-room acoustics," J. Acoust. Soc. Am. **65**(4), 943–950 (1979).
[22]F. Ma, J. Chen, J. H. Wu, and H. Jia, "Realizing broadband sub-wavelength focusing and a high intensity enhancement with a spacetime synergetic modulated acoustic prison," J. Mater. Chem. C **8**(28), 9511–9519 (2020).
[23]F. Ma, J. Chen, and J. H. Wu, "Experimental study on performance of time reversal focusing," J. Phys. D Appl. Phys. **53**(5), 055302 (2020).
[24]M. Kleiner and J. Tichy, *Acoustics of Small Rooms* (CRC, New York, 2017), pp. 37–99.
[25]M. L. Willardson, B. E. Anderson, S. M. Young, M. H. Denison, and B. D. Patchett, "Time reversal focusing of high amplitude sound in a reverberation chamber," J. Acoust. Soc. Am. **143**(2), 696–705 (2018).
[26]M. K. Rollins, T. W. Leishman, J. K. Whiting, E. J. Hunter, and D. J. Eggett, "Effects of added absorption on the vocal exertions of talkers in a reverberant room," J. Acoust. Soc. Am. **145**(2), 775–783 (2019).
[27]M. R. Schroeder, "The 'Schroeder frequency' revisited," J. Acoust. Soc. Am. **99**(5), 3240–3241 (1996).
[28]B. E. Anderson, M. Clemens, and M. L. Willardson, "The effect of transducer directivity on properties of time reversal focusing," J. Acoust. Soc. Am. **139**(4), 2083–2083 (2016).
[29]B. Van Damme, K. Van Den Abeele, Y. Li, and O. Bou Matar, "Time reversed acoustics techniques for elastic imaging in reverberant and non-reverberant media: An experimental study of the chaotic cavity transducer concept," J. Appl. Phys. **109**, 104910 (2011).
[30]H. Kuttruff, *Room Acoustics*, 6th ed. (CRC, Boca Raton, FL, 2017), pp. 66–69.
[31]M. R. Schroeder and K. H. Kuttruff, "On frequency response curves in rooms: Comparison of experimental, theoretical, and Monte Carlo results for the average frequency spacing between maxima," J. Acoust. Soc. Am. **34**(1), 76–80 (1962).
[32]ISO 3741:2010, "Sound power and energy in reverberant environments" (International Organization for Standardization, Geneva, Switzerland, 2010).
[33]M. R. Schroeder, "New method of measuring reverberation time," J. Acoust. Soc. Am. **37**(3), 409–412 (1965).
[34]M. Tanter, J. Thomas, and M. Fink, "Time reversal and the inverse filter," J. Acoust. Soc. Am. **108**(1), 223–234 (2000).

Chapter 3

Nonlinear Characteristics of High-Amplitude Focusing Using Time Reversal in a Reverberation Chamber

3.1 Introduction

The following chapter is a peer-reviewed published journal article that is published in the Journal of the Acoustical Society of America. While conducting high-amplitude TR focusing experiments in the large reverberation chamber at BYU, it was observed that deviations from linear scaling of the peak amplitude occurred.[41] These deviations were initially unexpected (nonlinear amplification), and an investigation of them forms the basis of this dissertation. This paper discusses in detail the processes required to maximize the nonlinearities observed in order to better understand and characterize the mechanism behind them. Through multiple experiments a hypothesis of a free space Mach stem formation, referred to as Mach wave coalescence, is proposed and an experiment is designed to test it. The resulting data suggests that the hypothesis is valid, and that the nonlinear increases in amplitude reported are the direct result of the coalescence of high-amplitude waves converging to the focus position.

3.2 Required Copyright Notice

Citation:

B. D. Patchett and B. E. Anderson, “Nonlinear characteristics of high amplitude focusing using time reversal in a reverberation chamber,” J. Acoust. Soc. Am., **151**(6), 3603-3614 (2022).

JASA ARTICLE

Nonlinear characteristics of high amplitude focusing using time reversal in a reverberation chamber

Brian D. Patchett and Brian E. Anderson[a)]
Acoustics Research Group, Department of Physics and Astronomy, Brigham Young University, Provo, Utah 84602, USA

ABSTRACT:
Time reversal (TR) signal processing is an effective tool to exploit a reverberant environment for the intentional focusing of airborne, audible sound. A previous room acoustics TR study found preliminary evidence that above a certain focal amplitude the focal waveform begins to display signs of nonlinearity [Willardson, Anderson, Young, Denison, and Patchett, J. Acoust. Soc. Am. **143**(2), 696–705 (2018)]. This study investigates that nonlinearity further by increasing the focal peak amplitudes beyond that previously observed. This increases the nonlinear characteristics, allowing for a closer inspection of their properties. An experiment is conducted using eight horn loudspeaker sources and a single receiver in a reverberation chamber. A maximum peak focal amplitude of 214.8 kPa (200.6 dB_{pk}) is achieved. The focus signal waveforms are linearly scaled to observe and characterize the nonlinear amplification of the waveform. Frequency spectra of the peak focal amplitudes are plotted to observe changes in frequency content as the signals become nonlinear. A one-dimensional spatial scan of the focal region is conducted to observe properties of the converging and diverging waves. A proposal for a possible explanation involving free-space Mach stem formation is given. https://doi.org/10.1121/10.0011517
(Received 21 February 2022; revised 11 May 2022; accepted 12 May 2022; published online 1 June 2022)
[Editor: Julian D Maynard] Pages: 3603–3614

I. INTRODUCTION

Time reversal (TR) is a signal processing technique utilized in multiple areas of wave physics.[1–3] Its origins began in the early 1960s to provide reproducible sound transmission for underwater communication,[4,5] and at the time was referred to as matched signal processing. TR has been used in a reverberant environment to generate intentional focusing of sound at a receiver position from a distant source, or bank of sources.[6–9] There is a forward step, and a backward step when generating a TR focus. In the forward step an impulse response (IR) is obtained for a physical system. To accomplish this, a chirp signal is broadcast from a source position and the response is recorded at a receiver position as the chirp response (CR). The IR can then be approximated by performing a cross correlation of the original input chirp signal and the CR.[10,11] In the backward step, the IR is reversed in time [afterward referred to as the time-reversed impulse response (TRIR)] and broadcast from the source position. Due to the reciprocity of the system, the TRIR produces waves that retrace the same paths traversed during the forward step, resulting in acoustic waves converging on the receiver position as a focus of sound.

There are a wide variety of applications of high-amplitude TR. One such area, non-destructive evaluation of solid materials, utilizes TR to probe solid materials with focused ultrasound at various locations to locate and image defects in the solid by observing nonlinear content of the resulting focus signal.[3,12–18] The TR focusing generated in these studies is large enough to excite nonlinear wave motion of cracks or delaminations in the material, but not high enough amplitude to induce nonlinear motion of the intact portions of the material. Through a relative comparison of the TR focusing generated at intact and damaged locations, one can identify the damaged locations by observing relative increases in nonlinear wave phenomena (e.g., harmonic frequency content). Additional analytical methods have also been developed to help increase the ability to detect nonlinearities when TR is focused at localized positions in a solid. These include phase inversion (or pulse inversion),[14,18] the scaling subtraction method (implemented in the time domain[12,13] and the frequency domain[12,16,17]), and third-order phase symmetry analysis.[19] Observation of nonlinearities in TR focused waves in solid materials without localized defects, such as in concrete mortar blocks, has been made but not carefully studied.[20] Several of the methods listed above were found to be of use in interpreting the data presented in this paper.

High amplitude TR has multiple biomedical applications as well. In a paper by Thomas *et al.*,[21] the treatment of kidney stones, known as lithotripsy, is discussed as an application where a time-reversal mirror (in the form of a small transducer array) is used to target a kidney stone. Studies of the application of TR for histotripsy applied to brain tumor treatment have also been conducted.[22,23] These studies applied the methods of TR to focusing through inhomogeneous materials to multiple positions within a human skull. TR has also been used as a method of imaging imperfections in human teeth using ultrasound.[24] In each of these papers the goal was to generate high amplitude acoustic energy rather than to study any nonlinearities of the focused waves.

[a)]Electronic mail: bea@byu.edu

The use of TR in room acoustics initially explored communications applications in complex environments.[6–9] Ribay *et al.*[8] asserted that in an average room environment the amplitude of the TR focusing is proportional to the number of sources, reverberation time of the room, and bandwidth of the impulse response. Denison and Anderson[25] confirmed that a longer reverberation time leads to a higher focal amplitude if the reverberation time is altered due to changes in the absorption in the room. However, they found that increasing the room size to increase the reverberation time decreased the amplitude of TR focusing. Denison and Anderson[26] also found that sources used in the backward step should be placed further away from the focusing location than the critical distance in the room and that sources and focusing location should be in the same Cartesian plane in a rectangular room. Anderson *et al.*[11] showed that, in a reverberant room, aiming sources away from the intended location for TR focusing also increases the amplitude of the focus. Willardson *et al.*[27] explored the use of TRIR modification methods and found that the processing technique known as clipping yielded the largest amplitude TR focusing. Using the clipping technique, they were able achieve a peak focus sound pressure level of 173.1 dB_{pk} using a chirp with a bandwidth of 500–7500 Hz. Wallace and Anderson[28] demonstrated that TR focusing of airborne ultrasound could be used to generate a nonlinear difference frequency, achieving peak focal amplitudes of 134 dB_{pk} [henceforth, all measured dB values are peak values (dB_{pk}) reported with a reference of 20 μPa] with frequencies between 35 and 40 kHz. And recently, Patchett *et al.*[29] showed that the amplitude of the TR focusing depends on the location of the receiver with respect to the room boundaries. Placing the microphone used to measure the IR(s) in the corner of the room in order to focus sound there yields approximately a 9 dB increase in the focusing amplitude compared to the microphone being placed away from all walls in the room.

Appert *et al.*[30] presented an analytical and numerical study applied to observations of nonlinear wave steepening in the generation of nucleation points in liquid helium via the use of focused spherical sound waves. While TR was not used in this case, the observations of nonlinearities in a focused sound wave prove relevant to this study. The models used indicated that the breakdown of the standard linear equation of state for helium was a key factor in the generation of nonlinearity in that study. Nonlinear behavior in TR focusing of underwater sound was also observed in a study by Montaldo *et al.*[31] They showed that when focal signals are generated underwater with increasing amplitude the wave distorts in shape, in that the leading side of a compression peak in a focus signal steepens significantly forming shock waves. When the results of Montaldo *et al.* are linearly scaled, the amplitude of the largest compression peak is lower in amplitude than the linearly scaled version of the lower amplitude focus signal. Their experimental setup had waves propagating principally from one direction to the focus location, whereas in this paper the wave focusing effectively comes from all directions (when including the contributions from image sources). Willardson *et al.*[27] demonstrated that TR can be used to generate high amplitude acoustic focusing in air. At the maximum focusing amplitudes they reported of 173 dB_{pk}, there was an observable distortion in the focus signal. This distortion was characterized by steepening of the leading edge of the focus in the time domain, a slight nonlinear increase in the amplitude of compressions, and a slight nonlinear suppression of rarefactions. This nonlinear increase in focused compressions observed by Willardson *et al.* in airborne focusing was not observed by Montaldo *et al.* with underwater focusing; instead, compression peaks decreased in the Montaldo *et al.* study. Wallace and Anderson[28] did not observe wave steepening or these nonlinear increases and suppressions of compressions and rarefactions, respectively.

The purpose of this paper is to further study the nonlinearities apparent in TR focusing of higher amplitudes than those achieved by Willardson *et al.* Higher amplitudes are achieved by using a smaller reverberation chamber, multiple high-amplitude loudspeakers in the same plane as the focusing location, pointing the sources away from the focal location, using the clipping TR method, and focusing in the corner of the room. As summarized previously each of these methods contributes to higher amplitude focusing. Importantly, microphones with lower sensitivities than those used by Willardson *et al.* were used here to enable accurate recording of these higher amplitudes. These measures allow the generation of TR focusing amplitudes that greatly exceed any previously measured results, thereby increasing the nonlinearities in the focused waves allowing a more careful observation of them. Comparisons of linearly scaled focal signals are presented, as well as a one-dimensional spatial scan of the high-amplitude converging and diverging waves of the TR process. Optimization of the amplitude of the TR focusing is discussed, with a description of the applied methods of refinement. A comparison of different microphone types is done to confirm that the levels reached are genuine and not an artifact of the equipment or systematic error. Representation of the harmonic content is also presented to show that the high frequency content increases significantly as the focus amplitude is increased. A proposed explanation of the observed nonlinearities is presented, that of free-space, Mach-wave generation in the superposition of converging waves.

II. EXPERIMENTAL DETAILS

A. Setup

The experiments were carried out in the smaller of two reverberation chambers available on the campus of Brigham Young University. This is due to the findings by Denison and Anderson[25] and by Patchett *et al.*[29] showing that a room of smaller volume and dimension contributes to a higher peak focal amplitude. This smaller reverberation chamber has dimensions 5.7 m × 4.3 m × 2.5 m and a volume of 61 m^3. The overall reverberation time in the room is approximately 4.16 s across the chirp bandwidth used, with a

https://doi.org/10.1121/10.0011517

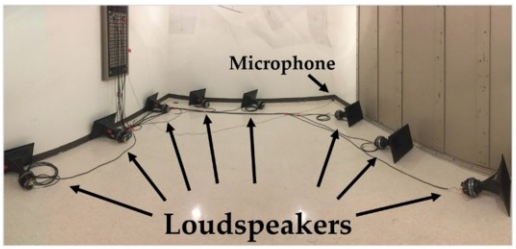

FIG. 1. (Color online) Photograph of the experimental layout in the small reverberation chamber. The room is a rectangular room with parallel walls, along with diffusing panels (partially shown at the top of the image) intended to make the sound field more diffuse. Distortion in the image is due to the panoramic nature of the photograph.

Schroeder frequency of 522 Hz. While the large chamber used measures 4.96 m × 5.89 m × 6.98 m, with a volume of 204 m^3, with an overall reverberation time of 7.6 s across the chirp bandwidth, and a Schroeder frequency of 410 Hz. A PCB (Buffalo, NY) microphone, model 112A21 with a sensitivity of 7.1 mV/kPa, is the primary receiver for the experiments unless otherwise stated. It is placed in the lower corner of the chamber and oriented pointing toward the floor, with the face 1 cm from each adjacent wall. Eight BMS (Hannover, Germany) 4590 dual diaphragm high output loudspeakers fitted with the appropriate crossovers and horns manufactured by BMS are utilized as the sources (referred to as loudspeakers). A photograph of the setup is shown in Fig. 1. They are placed in the chamber facing toward the walls in order to minimize the amplitude of the direct acoustic path to the microphone.[11] When utilizing normalized TRIRs, the TR process yields higher amplitude focusing when the direct sound is not much larger than the multi-path reverberation in the TRIR. This is achieved by pointing somewhat directional sources away from the target microphone for the focusing location so that the direct sound arrival is smaller in amplitude. Power to the drivers is provided by two Crown (Elkhart, IN) CT4150 amplifiers. A swept sine wave (chirp signal) is then created with a bandwidth of 500–15 000 Hz, and length of 4.16 s. This chirp is broadcast sequentially from each driver. This allows for a calculation of the IR for each individual loudspeaker-to-microphone combination.

The preprocessing method known as clipping is applied to the TRIR signals before they are broadcast during the backward step. This method has been shown to be the most effective at increasing the focus amplitude, in both air and in solid media, when compared to other well-known methods of preprocessing.[27,32] Clipping TR, similar in nature to one-bit TR,[31] intentionally clips the higher amplitude portions of a TRIR, which is then normalized, resulting in a relative increase in the broadcasted energy. Importantly, the phase information (timing of the reflections) is preserved in the TRIR. The threshold value for clipping in these experiments was set to 0.05. This value is slightly different than the threshold used by the Willardson *et al*. but was found to optimize peak focus amplitudes in various trials during the experimental setup and calibration. These clipped TRIRs are normalized to utilize the full power output available from the amplifiers. The TR process is carried out using an in-house designed LABVIEW™ (Austin, TX) executable program, coupled with two Spectrum Instrumentation (Großhansdorf, Germany) M2i.6022 signal generation cards and a M2i.4931 digitizer card. A sampling frequency of 250 kHz is used for generating and digitizing all signals used in this study. All post-processing is done with MATLAB™ (Natick, MA). Figure 2 shows an example of the signals generated in the TR process used here.

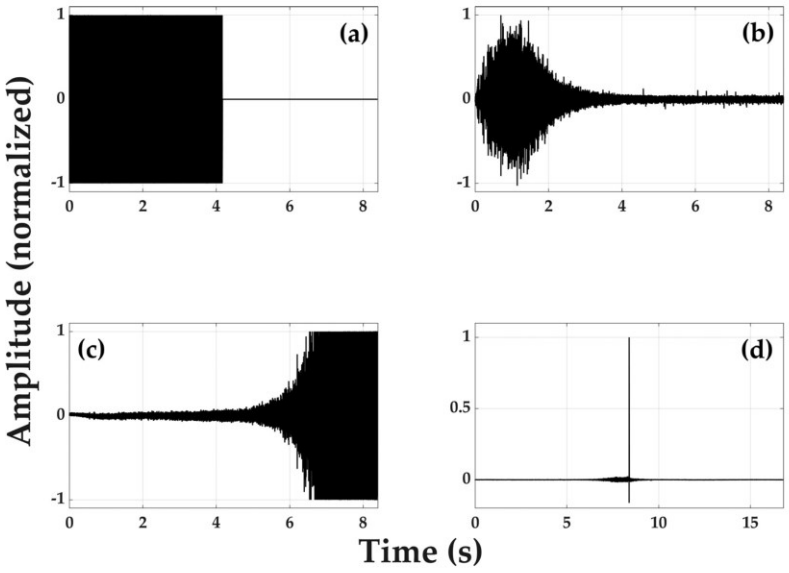

FIG. 2. Example signals used in the time reversal experiments. (a) The logarithmic, swept-sine chirp signal. (b) The chirp response (CR) recorded in the forward step at the microphone. (c) The normalized, clipped time reversed impulse response (TRIR). (d) Focus signal generated by simultaneous broadcast of eight loudspeakers. All amplitudes in this figure are normalized.

B. Linear vs logarithmic chirp signal

The use of a cross correlation of the chirp signal and measured CR to extract an IR typically relies on the use of a linearly varying, swept-sine frequency chirp (linear chirp). It is logical to assume that equal amplitude per frequency will produce the optimal amount of amplitude in TR focusing of impulsive signals since a Delta function's spectrum contains equal amplitude at all frequencies. However, it was found empirically by others (including the authors) in a few different systems that the use of a logarithmically varying, swept-sine frequency chirp (log chirp) yielded larger TR focusing amplitudes than when using a linear chirp.[27,28,33] Higher frequencies generally experience a larger degree of damping with wall absorption, thermo-viscous propagation, and boundary-layer losses. This results in a frequency-dependent reverberation time in the room, with longer reverberation times at lower frequencies. Therefore, the use of a log chirp, with a longer time spent at lower frequency, will result in an IR with overall longer reverberation times than would be found when using a linear chirp because there is more low frequency content. Longer reverberation times in the IRs results in larger amplitude TR focusing for a given room.[8]

Figure 3 shows a comparison of the IR time signals and their corresponding spectra. The IRs are normalized by their respective peak values but the frequency spectra are both normalized with respect to the peak of the log spectrum.

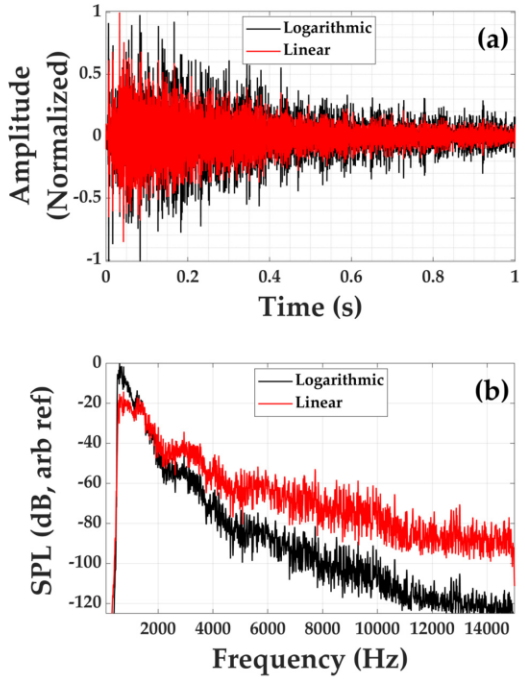

FIG. 3. (Color online) Normalized (a) impulse response signals and (b) associated frequency response spectra obtained with linear and log chirp signals (both normalized with respect to the peak of the logarithmic spectrum).

While similar in amplitude over time, the IR obtained with the log chirp has a larger amount of energy over the time period shown. The spectrum of the IR obtained with the log chirp also has a larger amount of energy present at low frequencies. Overall energy can be compared by squaring and then summing the pressure sample values in the IR signals. This method of energy comparison reveals an energy increase in the log signal of 12 dB compared to the linear signal, which indicates average pressure values are four times higher in the log IR when compared to the linear IR (Fig. 3). Due to the higher overall energy in the normalized IR obtained with the log chirp, application of clipping TR should also benefit from the use of the log chirp in terms of achieving a larger focusing amplitude. This is because a larger amplitude exists for a longer period of time in the TRIR so that when it is clipped more energy remains in the clipped TRIR and thus more energy is broadcast in the backward step. Empirical results demonstrate that the use of a log chirp to obtain the IR results in a larger TR focusing amplitude whether clipping TR is used or not. Based on these results a log chirp is used throughout the remainder of the experiments.

III. GENERATING A HIGH-AMPLITUDE FOCUS

A. Physical nonlinear characteristics

The TR process is now optimized to achieve the maximum possible peak focal amplitude by using a logarithmic chirp, eight loudspeakers, the clipping TR method, a smaller reverberation chamber, and by placing the microphone in a corner position. The peak focal amplitudes now obtained greatly exceed levels that have previously been reported for TR focusing of sound in air. The focal signals are modified in order to scale their amplitudes linearly up to the highest amplitude result, allowing for analysis of the focusing waveform as the output level in increased. By scaling the signals in this manner, a comparison of the nonlinear departure from linear scaling can be made. Figure 4 shows a zoomed-in view of the focal signals at the microphone location at five different levels. The same TRIRs were used in each case but the amplitude of the input signals to the amplifiers were increased. As the output from the generating cards is increased there is a dramatic change in the focal waveforms. The leading edge steepens dramatically, moving the largest compression peak forward in time. This is an indication of an amplitude dependence of the speed of sound. The rarefactions shift backward in time, indicating a relative slowing of their propagation speed. These amplitude-dependent, wave-steepening observations are characteristic of nonlinear shock wave formation.[34–36] The peak focus value for the highest amplitude focus signal in Fig. 4(a) measures 214 800 Pa, a sound pressure level of 200.6 dB_{pk}. Atmospheric pressure at the elevation where these measurements were made is 86 kPa, not the standard 101 kPa at sea level. This means that the peak pressure of 215 kPa is approximately 2.4 times the ambient pressure, or an overpressure that is 1.4 atmospheres above the ambient pressure.

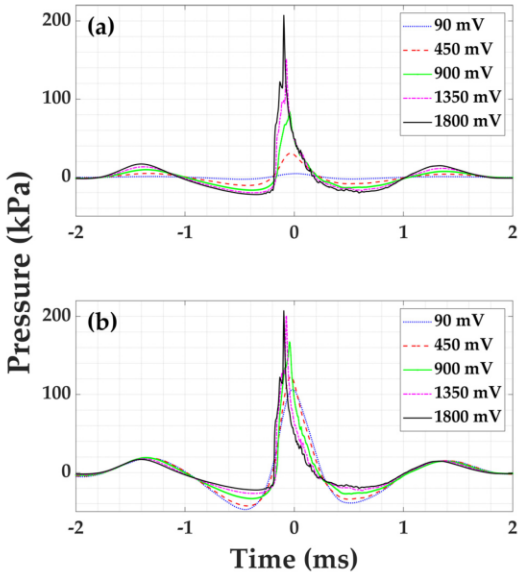

FIG. 4. (Color online) (a) Five focus signals recorded at the microphone position as the voltage of the signal from the generator cards is increased. (b) Linearly scaled versions of the focus signals in (a). Legend values represent the output level from the generator cards.

Figure 4(b) compares the same waveforms as shown in Fig. 4(a) but these are linearly scaled by multiplying each signal by the appropriate scaling constant relative to the scaling used for the output voltage signal amplitude. This figure illustrates the primary nonlinear phenomenon of interest. When scaled, linear waveforms should be identical with small deviations being possible due to background noise. In Fig. 4(b) it is apparent that the large compression peak increases in amplitude in a nonlinear fashion. Smaller effects were reported by Willardson *et al.*[27] The compression peak distorts significantly in shape by steepening on the leading edge of the compression. There are two peaks evident in the compression peak and the presence of both of these peaks is repeatable in these largest amplitude experiments. The initial, lower amplitude peak is caused by a prominent wave (sidelobe) that is detected by the microphone prior to it reflecting off of the nearby wall and arriving at the intended focal time. The trailing edge of the compression peak rolls off in amplitude more slowly than linear scaling would predict. The rarefactions on either side of the compression peak also do not scale linearly. These rarefactions are nonlinearly suppressed with increasing amplitude of the focusing. The lower amplitude peaks and troughs at times before and after these rarefactions appear to maintain linear scaling. This suggests that only in the high enough amplitude waves that produce the TR focusing are these nonlinear effects observed. Additionally, because the lower amplitude peaks before and after the main focal event scale linearly, this suggests that the distortion is generated acoustically rather than by the amplifiers since the distortion of the peaks only occurs for the higher amplitude peaks.

Multiplication of the TRIR signals by −1 inverts the phase of these signals and when used in the TR process this creates a focused rarefaction as opposed to a compression. The results of this inversion, shown in Fig. 5, was done to observe the nonlinear effects seen when the focus is a rarefaction as opposed to a compression (Fig. 4). It is apparent from Fig. 5 that similar physical phenomena are present in a rarefaction focus as well. The scaled rarefaction focus also exhibits a suppression of its maximum and is shifted later in time. The leading and trailing compressions show nonlinear growth with increasing amplitude. Instead of wave steepening happening on the leading edge of the compression, as observed with a focused compression, now a wave steepening is observed most dramatically on the trailing edge of the rarefaction peak, which is the leading edge of the largest compression peak. The lowest peak rarefaction value measured is 31 300 Pa (in absolute units), a value of 54 700 Pa (underpressure) below the ambient level of 86 kPa, or a sound pressure level of 188.7 dB_{pk}.

B. Frequency analysis of focus signals

An autospectrum of each increasing-amplitude focus signal from Fig. 4 provides insight into the changes in the frequency content as the focal signal amplitude increases and subsequent acoustic nonlinearity increases. Figure 6 shows that as the level of the input signal is increased, the low frequency content decreases, and the high frequency content increases. A similar analysis of the frequency content of the focal signals was made in the Willardson *et al.*

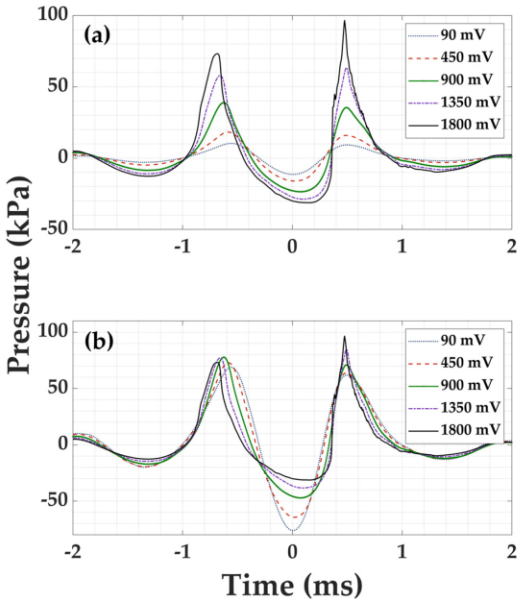

FIG. 5. (Color online) (a) Five inverted focus signals recorded at the microphone position as the voltage of the signal from the generator cards is increased. (b) Linearly scaled versions of the inverted focus signals in (a). Legend values represent the output level from the generator cards.

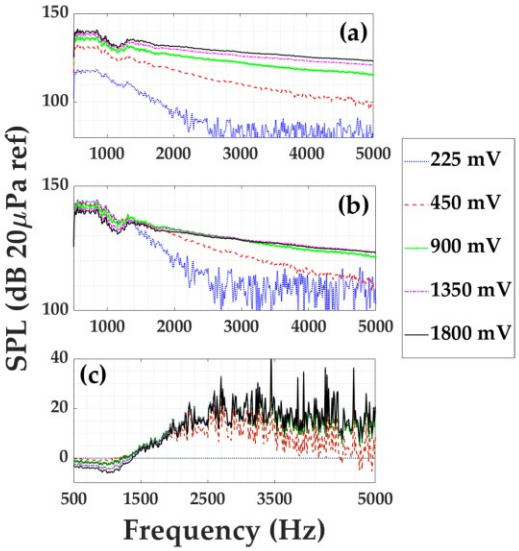

FIG. 6. (Color online) (a) The autospectrum of each focus signal of Fig. 4 with increasing output from the generator cards. (b) The scaled autospectrum of each focus. (c) The difference of the scaled autospectra in (b) with respect to the lowest amplitude spectrum.

study of this phenomenon.[27] Figure 6(c) depicts the autospectral difference in the focus signal recorded by the microphone as the gain is increased (relative to the lowest amplitude spectrum). It is apparent from Fig. 6(c) that there is a large increase in the high frequency content extending from 1500 to 7500 Hz when the focus signal amplitude is increased. The presence of increasing high frequency content is an indicator that the focus signal may be developing harmonic content that is characteristic of nonlinear harmonic generation as the waves steepen due to high amplitude propagation of the waves. Typically, with nonlinear acoustic harmonic generation of a sine wave, the higher harmonics grow in amplitude as the amplitude of the fundamental decreases and the overall peak amplitude of the wave decreases.[34] This would suggest that the peak focal amplitudes observed should decrease as the acoustic amplitude of the focus increases. However, as shown in Fig. 4, there is a nonlinear increase in the peak amplitude of the focus, while the high frequency content continues to increase. In the linearly scaled spectra plot [Fig. 4(b)] frequencies between 500 and 1000 Hz of the highest amplitude focus spectrum loses 6 dB, while the frequencies from 1000 to 2000 Hz see an increase by as much as 10 dB, when compared to the lowest level peak focus amplitude. It appears that the high frequency content begins to converge to a constant increase value as the focal signal amplitude is increased. The large fluctuations seen in the high frequencies (above 2500 Hz) of the lowest focal amplitude signal in Fig. 4(c) are due to the recording being near the noise floor of the microphone. Thus, the differences in the higher amplitude spectra should be greater than those displayed in Fig. 4(c), likely continuing to increase at the slope seen from 1500 to 2500 Hz.

C. Confirmation of focus amplitude values using multiple microphones

To the authors' knowledge, the peak levels produced in this study far exceed any achieved in previously conducted experiments of TR with airborne sound, being 29.5 dB higher than the peak level reported by Willardson *et al.*[27] It is also noteworthy that the peak levels measured exceed the operating limits of most condenser microphones. An investigation into the validity of the amplitude values measured by the equipment is conducted using two different microphones measuring the same TR focusing events. As is demonstrated in Sec. IV, the spatial width of the peak is on the order of 1 cm. This allows for two microphones to be placed closely enough to measure the same focus amplitude with relative accuracy. A PCB (Depew, NY) 112A21 and a GRAS (Holte, Denmark) 46BG are used to conduct the test. The 112A21 is a piezoelectric-type transducer designed to measure high-amplitude pressure waves, with a manufacturer's specified measurement maximum level of 210 dB, and sensitivity of 7.10 mV/kPa. The 46BG is an electret, condenser microphone (pressure type) with a measurement maximum level of 184 dB and sensitivity of 300 mV/kPa. The forward step of recording the chirp response was done with the 112A21. Because of its lower sensitivity level, the frequency content stays well within the measurable range of the 46BG, and no loss of frequency content need be assumed due to the difference in the two microphones differing sensitivities. For this test, the microphones were placed in the middle of the small reverberation chamber oriented with the faces of the diaphragms toward each other, and a spacing between them of about 3 mm.

The measurements were done by beginning with a minimum output level from the Spectrum generator cards of 100 mV, and then incrementally increasing that level by 3 dB until the peak focal amplitude reached the maximum operating level of the 46BG. Each focus was performed five times to obtain an average value for each measurement. In order to demonstrate that the measurements from each microphone are very closely matched, the experiment is initially done with just one source loudspeaker. This resulted in focal amplitudes that are low enough that nonlinear characteristics are not observable in the focus signal. The experiment is then repeated with all eight of the sources, and the levels are increased until the 46BG reaches it maximum operating limit (here, 1131 mV output from the generator cards). Figure 7 illustrates the values recorded by each microphone. The magnitudes for the maximum rarefactions (the maximum negative value just prior to the peak compression) of the focus signals is also plotted. This demonstrates that the peak focus amplitudes reached throughout these measurements are being reliably measured, and no acoustic nonlinearity differences or microphone distortions are present. The two microphones have two very different types of transduction mechanisms and since both report the

JASA
https://doi.org/10.1121/10.0011517

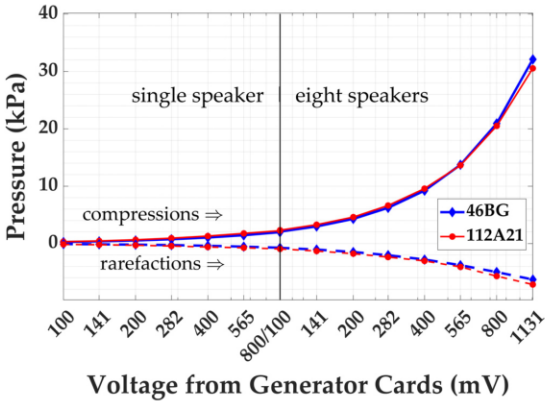

FIG. 7. (Color online) Comparison of PCB 112A21 and G.R.A.S. 46BG simultaneous microphone measurements of the same focus events as the output levels from the generator cards are increased.

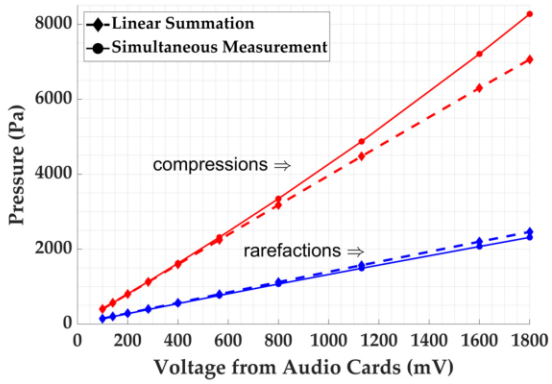

FIG. 8. (Color online) A comparison of the linearly summed peaks of focus signals generated by one loudspeaker at a time to the peak focus generated by all eight loudspeakers broadcasting simultaneously at increasing levels. The peak rarefaction values are represented as an absolute value of the measurement, and as such are positive. Traditional TR was used for these data.

same peak amplitudes, it can be assumed that no microphone distortions are present since it would be highly unlikely that both distort the response in the same way and both are being used within the manufacturers' specified ranges of linear assessment.

D. Linear summation vs acoustically summed focus waves

A traditional TR experiment (meaning clipping TR was not used here) was conducted comparing a linear sum of the focal signals from each of the eight loudspeakers generated one at a time and summed in post processing, and the acoustically summed focus resulting from the energy focused by all eight loudspeakers simultaneously. This experiment was performed with the G.R.A.S. 46BG microphone positioned in the reverberation chamber away from any reflecting surfaces. A TRIR for each loudspeaker is generated individually as before, and then broadcast at increasing output levels for each loudspeaker individually. The maximum pressure amplitudes of each of the eight focus signals (each generated by one loudspeaker at a time) for each level is then linearly summed and compared to the levels measured when all eight loudspeakers are broadcasting their respective TRIRs simultaneously. A comparison of the measurements is shown in Fig. 8.

The peak compressions of the simultaneously broadcast focus signals are clearly higher in amplitude than the focus signals that were broadcast individually and then summed. This indicates that there is a nonlinear acoustic phenomenon by which the compression peaks are increasing nonlinearly as the output levels are increased. The same can be seen in the absolute value (magnitude) of the rarefaction measurements, indicating that the suppression of the rarefactions is stronger when the eight loudspeakers are used simultaneously versus when the singular measurements are summed. A threshold of where nonlinear gain becomes significant in the increase in the peak focus amplitude is set by the authors as occurring when the ratio of the pressure between the simultaneously recorded peak, p_{sim}, and the peak calculated by linear summation, p_{lin}, has a level difference ≥ 0.5 dB,

$$Nonlinear\ Threshold = 20 * \log_{10}\left(\frac{p_{sim}}{p_{lin}}\right) \geq 0.5\,\text{dB}. \tag{1}$$

A level of increase of 0.5 dB has been deemed significant enough that it would lie outside of the potential for error in the measurement. Using this method, the nonlinear threshold in the preceding focus signals occurs above 800 mV of output from the audio generator cards. This corresponds to a sound pressure level in the simultaneously broadcast data of 165 dB_{pk}.

It is worth noting that the clipping TR method nonlinearly introduces additional high frequency content into the TRIR signal. However, once introduced to the TRIR signals, the same TRIR signals are broadcast from the loudspeakers for each increased signal level, so the clipping TR process cannot be the cause of the increasing nonlinearity observed with increasing levels. To avoid the possibility of any nonlinearity induced through the use of clipping TR process itself, the preceding experiment was performed without applying the clipping method to the TRIR, i.e., using traditional TR. The nonlinear compression amplification and nonlinear rarefaction suppression effects still are present, though to a lesser degree because the focal amplitudes achieved were not as high. This confirms that it is the simultaneity of the converging acoustic waves that is contributing to the observed nonlinear increases. A clipping TR spectrum possesses high amplitudes at higher frequencies than a traditional TR spectrum but when the signal levels fed to the loudspeakers are increased, a nonlinear increase in those high frequency amplitudes is observed whether clipping TR or traditional TR is used. When the increasing amplitude experiment is repeated and the clipping method is applied,

the nonlinear threshold occurs at a much lower output level of 400 mV from the generator cards because clipping TR produces higher focal amplitudes. Which, when considering the nonlinear acoustic addition of high frequencies described above, is expected, corresponding to a sound pressure level of 173 dB_{pk}. This is the level reported by Willardson *et al.*[27] as the point at which nonlinearity was beginning to appear in the data when they applied the clipping method. Thus, when TR is performed with the clipping method, levels above 173 dB_{pk} can be considered to have significant nonlinear characteristics, whereas the threshold is 165 dB_{pk} for traditional TR. The difference in nonlinear thresholds of 8 dB seems to be related to the higher frequency content contained in a clipped TRIR relative to that in the traditional TRIR, suggesting that the nonlinear threshold depends on the frequency content, which makes sense.

A similar analysis of the highest peak amplitudes attained using clipping TR is done, showing that when all methods of high amplitude focus generation are applied [logarithmically weighted chirp signal, clipping TR process, and receiver placement near maximum number of reflecting surfaces in the room (corner)], the peak focus amplitude increases nonlinearly from linear expectations. It must be pointed out that the linear data by which the comparison is being made is purely an approximation of a linear sum, derived by using the equation of the line for the linear summation data in Fig. 8, and adjusted to begin at the initial data point of the high amplitude data set. But it also indicates significant nonlinear increases at and above 175 dB_{pk}. Figure 9 shows the results of this experiment, with the peak focus amplitudes plotted against the linear approximation, reaching a peak compression of 200.6 dB_{pk} at maximum output from the generator cards.

Squaring and summing the linearly scaled pressure values across the full duration of each signal length allows an estimation of the change in the potential energy of each signal with increasing focal amplitude. Figure 10 shows a lowering of overall potential energy in the scaled signals, despite the nonlinear increase observed in the main compression of the focal signal.

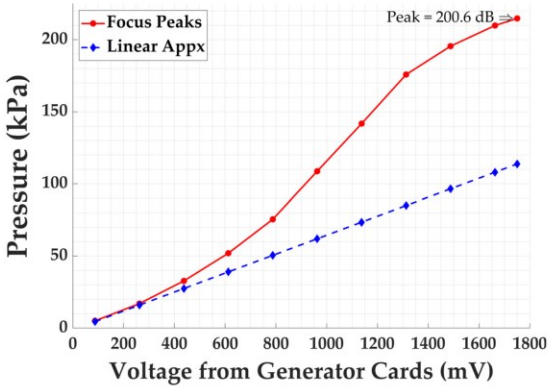

FIG. 9. (Color online) Peak focus amplitudes using clipping TR plotted alongside linearly scaled expected amplitudes.

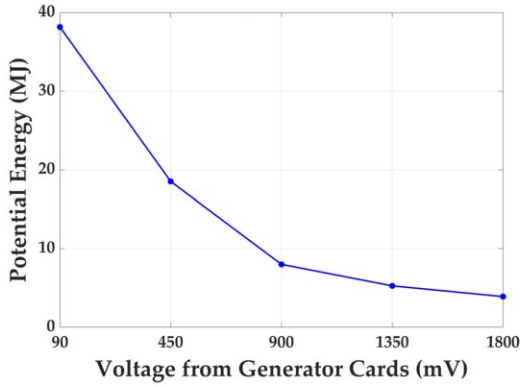

FIG. 10. (Color online) The sum of the potential energy values for the linearly scaled focal signals as the output from the generator cards is increased.

IV. LINE SCAN OF FOCUSING

A line scan of the spatial dependence of the high-amplitude TR focusing is presented in this section to obtain physical insights into the wave propagation during convergence and subsequent divergence in the TR focusing. This allows for a closer inspection of the changes to the converging and diverging waves as they propagate towards and away from the focal position, respectively. To conduct this experiment a linear-translation scanning system is placed in the larger reverberation chamber due to the size constraints of the smaller chamber. The experimental setup of the sources is similar to what was done previously in the smaller chamber. The PCB 112A23 microphone is mounted to an arm one meter above the ground, which is attached to the moving platform on the scanning system. The setup can be seen in Fig. 11.

IRs are obtained with the microphone at the center position of the scanning range. Once IRs are obtained, the microphone is moved 50 cm off of center and recordings are made across a line including the focal position from 50 cm to −50 cm in 0.50 cm increments, with the TRIRs being broadcast again for each microphone scan position. The

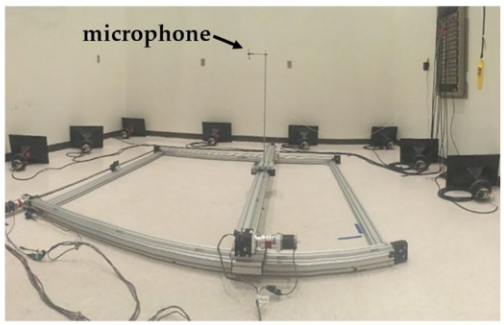

FIG. 11. (Color online) Photograph of the experimental layout for a one-dimensional line scan in the larger reverberation chamber. Distortion in the image is due to the panoramic nature of the photograph.

recordings at each position are then used to create an animation of the focused waves. The resulting animation (Mm. 1) shows waves approaching the focus location from both sides, the focusing moment, and waves moving away after the focus in one dimension. The duration of the entire animation represents 0.0068 s of time. Snapshots in time from this animation are depicted in Fig. 12.

Mm. 1. Animation of the spatial dependence of high-amplitude time reversal focusing over time. The data comes from a line scan in which the pressure was recorded at each spatial position while repeating the experiment. This is a file of type ".mp4" (4.34 MB).

Two important physical features may be observed in Mm. 1 and Fig. 12. The leading edge of the incoming wave fronts can be observed to steepen dramatically from Figs. 12(a) to 12(b). Figure 12(d) shows a time in which two waves are diverging outward after the focusing. The peak of the wave is visibly sharper in space relative to the incoming wave [compare the peaks in Figs. 12(b) and 12(d)]. This implies that there is more high frequency content in the diverging waves than was present in the converging waves. This growth of high frequency content should be expected with wave steepening of high-amplitude propagating waves. Interestingly, in these two diverging waves it is now the trailing edge of both of these waves that is steeper. Normally one would expect that the two converging waves superpose and then pass through each other before and after focusing. This should result in the leading edges of both converging waves and diverging waves always being the steeper sides of the waves. The waves do not appear to reflect off of each other either since reflection would also result in the leading edge of the waves being steeper. A quantitative analysis of the converging waves shows that as the wave moves across the frame to the focus position from the outer edges, the wave speed, c, increases from approximately 373 m/s at the edges to approximately 526 m/s as it converges across the last 0.20 m to the focus. Using a binomial expansion of the adiabatic equation of state [$p = \gamma p_0(\rho/\rho_0)$, where p is the acoustic pressure, γ is the ratio of specific heats, p_0 is the ambient pressure, ρ is the acoustic density, and ρ_0 is the ambient density], we can approximate the acoustic density of the air, ρ, as the wave passes the 0.10 m mark as 2.13 kg/m^3, and a density of 2.64 kg/m^3 at the time of focus. Using these values, the impedance of the converging waves just before they meet (at 0.10 m) is about 2.7 times higher than ambient conditions. Assuming adiabatic conditions hold, which is unlikely, the temperature, T_K, at the time of focus could be estimated ($T_K = c^2/\gamma r$, where r is the specific gas constant). This would also suggest an instantaneous temperature at the focus of 690 K at the time of focus!

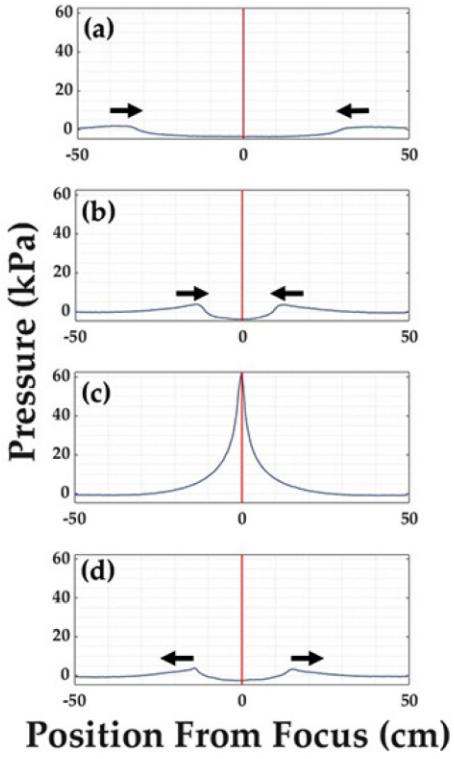

FIG. 12. (Color online) Snapshots in time from a spatial scan of the high-amplitude time reversal focusing. (a) Two waves converge toward the focal position. (b) The leading edge of each wave has steepened significantly as it progresses toward the focus. (c) The spatial dependence at peak focusing. (d) The trailing edge of each wave is steeper as they propagate away from the focus.

The full width half max of the peak is 4.5 ± 0.1 cm, with a peak amplitude in the line scan configuration of 188 dB$_{pk}$. This peak amplitude of the focusing is lower than the maximum value reported on in Fig. 4. This is due to the lack of rigid boundaries being near the focusing location (in order to allow for the scanning system hardware to be used) as expected from the work of Patchett *et al.*[29] The peak of the focusing in the line scan is 12 dB lower then when the focusing was in the corner of the room, whereas Patchett *et al.* suggested it should be closer to 9 dB lower between a corner location and a diffuse field location for the focusing location. It must be remembered that these two experiments of focusing to the corner and focusing for the line scan were done in different reverberation chambers. The line scan was done in the larger reverberation chamber, which chamber was also shown by Patchett *et al.* to reduce the peak amplitudes by an additional 3 dB. This means that the value of 12 dB lower than Fig. 4 is to be expected.

V. MACH STEM FORMATION IN CONVERGING WAVES

Ernst Mach first observed shockwave reflections in experiments reported in 1878.[36] It was noted that when a shockwave reflected from a rigid surface two types of phenomena could be observed. In the first, a shockwave propagates outward spherically from a source and is incident on a reflecting surface. The reflected wave and the incident wave

meet at the reflecting plane, and that intersection of the two propagates forward along the reflecting plane [Fig. 13(a)]. In the second, at a high enough pressure amplitude, the incident shock wave changes the ambient temperature and pressure of the medium it leaves behind (a breakdown of adiabatic assumptions) just enough to increase the speed of the reflecting wave. This allows the reflected shock wave to merge with the incident shock wave forming what has become known as a Mach stem [Fig. 13(b)]. The result is that three shock fronts are present, the incident shock, the reflected shock, and the region of convergence of the two, or the Mach stem.[36,37]

The Mach stem is the superposition of the incident and reflected waves and has a pressure value somewhat greater than the summation of the incident and reflected wave amplitudes. A study conducted by Karzova *et al.*[38] explored the formation of Mach stems from focused nonlinear acoustic beams. It was shown that the formation of underwater Mach stems could be achieved in free-space with no rigid reflecting surface, just the existence of two superposed nonlinear acoustic beams using a model based on a numerical solution to the Khokhlov-Zabolotskaya-Kuznetsov (KZK) equation.[39] Hansen *et al.*[40] was able to show through numerical calculation that two overlapping astrophysical bow-shock fronts generated between two propagating high-amplitude waves form a Mach stem in the region between them. In an unclassified technical report released by the U.S. Army Ballistic Research Laboratory, Reisler *et al.*[41] cited a study known as DIPOLE WEST, where measurements were made of simultaneous and non-simultaneous multi-blast shockwave interference in the air. The results from those tests conclusively showed that two or more shockwaves that interfere with each other generate the same Mach stem type effect seen when the shockwaves are incident upon hard boundaries, but at their intersection regions in the medium. This effect, referred to as Mach wave coalescence, was recently defined for small incidence angles in jet noise by Willis *et al.*,[42] where the increase in wave amplitude and propagation distance was observed experimentally. Vaughn *et al.*[43] confirmed this effect by quantifying an angle of incidence for nonlinear Mach wave reflection leading to a steeper shock front at the reflecting surface.

These generated regions of excess pressures in the Mach wave front were greater than the sum of the initial waves combined. This supports a potential mechanism for the nonlinearly increased focal amplitudes of compressions observed in this paper. The amplitude of the time reversed waves continuously increases as the TRIRs are broadcast into the reverberation chamber at higher levels. As the final reflection paths converge to the focus, the propagation of sound coming from the walls to the microphone approximates an array of high-pressure spherical waves emanating from images sources that surround the focal position.[25,44] As these waves converge to the focus, they begin to physically intersect with one another. At high-amplitudes it stands to reason that the overlapping areas of these waves reach a pressure level greater than their linear sum, due to free-space Mach stem formations. This effect is sketched in Fig. 14. Six of the many possible waves that contribute to the focusing are depicted to comprise the net spherically converging wave that creates the focus. At high-amplitudes Mach stems could be created at the overlapping regions of adjacent waves. If the reader will recall from the Introduction, Montaldo *et al.* showed that high-amplitude focusing did indeed generate wave steepening, but did not

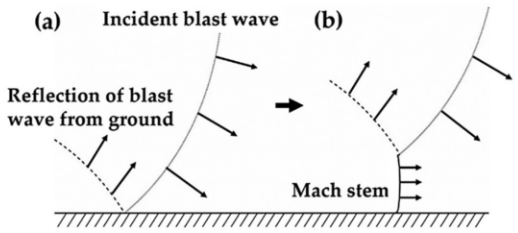

FIG. 13. Drawings of incident and reflected blast waves from an above ground explosion, along with a Mach stem formation. (a) The initial blast wave is incident on the ground, and the reflected wave propagates outward. (b) Later in time, and propagated further from the initial blast region in distance, the reflected wave and incident wave merge to form a Mach stem.

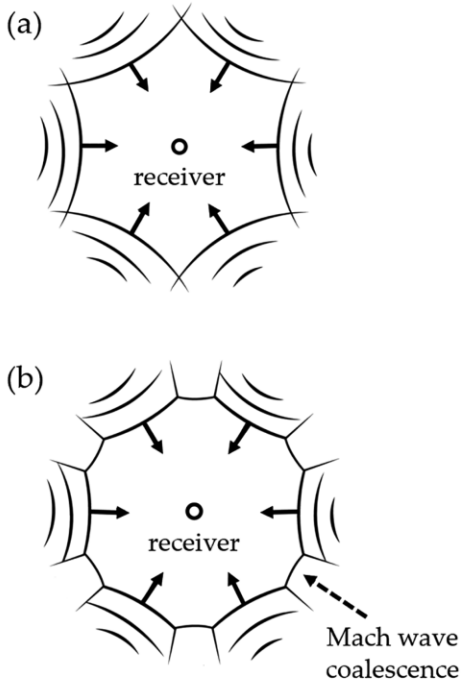

FIG. 14. (a) Drawing of six propagating waves that together approximate a spherically converging wave that arrives at the receiver position (or focal position). The arrows indicate the direction of travel of the wavefronts. (b) The overlapping regions form a Mach stem between them in free space, meaning there is no rigid reflecting surface necessary to generate the stem. One of the Mach stem regions is labeled for clarity.

show the nonlinear amplification of the compressions in the focusing as observed here. In that paper, underwater sound is being focused mainly from a single direction of propagation. This should result in fewer Mach stem formations since there are fewer overlapping waves converging to the focal location. Whereas, in the reverberation chamber the sound waves are coming in from all directions, allowing for a large quantity of overlapping regions and therefore increased opportunity for a free-space Mach stem effect to amplify the TR focusing nonlinearly.

VI. CONCLUSIONS

This paper reports a peak amplitude obtained through clipping TR focusing of audible sound in a reverberation chamber of 200.6 dB_{pk}. Significant nonlinear amplification of compressions by as much as a factor of 1.9 were observed, along with nonlinear suppression of rarefactions by as much as a factor of 2.1. Significant waveform steepening was observed in these high-amplitude focused waves as well. The initial observations of nonlinear phenomena reported by Willardson *et al.*[28] were much smaller deviations from predicted linearity. A threshold of nonlinearity can now be defined for applications of the traditional TR process of 165 dB_{pk}, and for the application of clipping TR of 173 dB_{pk}. This provides a benchmark value for an assumed linear or nonlinear regime of measurement.

This paper has shown evidence to support the idea that the nonlinear growth of focus amplitudes is genuine, along with the nonlinear suppression of rarefaction peaks. The application of TR focusing to generate such a large-amplitude signal has played a unique role in generating overlapping wave fronts by allowing for the convergence of these waves in a reverberant environment, and the nonlinear amplification is clearly evident at the levels attained. Autospectral analysis of the linearly scaled focus signals shows that there is a large increase in the high frequency content as the focus amplitude is increased, which is characteristic of nonlinear waveform steepening in the propagation of high amplitude waves. Both shock wave interaction theory, and experimental data presented here, leads us to believe that free-space Mach stems are being generated in the final converging waves of the TR process, which leads to the nonlinear increase in the peak focal compression amplitudes. This is because the focusing generates a wavefront that is the superposition of many converging high-amplitude waves upon each other. Future and ongoing experiments are seeking to verify this hypothesis of the Mach stems being the cause of the nonlinear increase in compression amplitudes. Thus, we believe that both nonlinear waveform steepening and nonlinear free-space Mach stem formation is occurring in high amplitude TR focusing of sound at the amplitudes reported.

[1]M. Fink, "Time reversed acoustics," Phys. Today **50**(3), 34–40 (1997).
[2]B. E. Anderson, M. Griffa, C. Larmat, T. J. Ulrich, and P. A. Johnson, "Time reversal," Acoust. Today **4**(1), 5–16 (2008).
[3]B. E. Anderson, M. C. Remillieux, P.-Y. L. Bas, and T. J. Ulrich, "Time reversal techniques," in *Nonlinear Acoustic Techniques for Nondestructive Evaluation*, 1st ed., edited by T. Kundu (Springer, Berlin, 2018), Chap. 14, pp. 547-581.
[4]A. Parvulescu and C. S. Clay, "Reproducibility of signal transmissions in the ocean," Radio Electron. Eng. U.K. **29**(4), 223–228 (1965).
[5]C. S. Clay and B. E. Anderson, "Matched signals: The beginnings of time reversal," Proc. Mtgs. Acoust. **12**(1), 055001 (2011).
[6]S. Yon, M. Tanter, and M. Fink, "Sound focusing in rooms: The time-reversal approach," J. Acoust. Soc. Am. **113**(3), 1533–1543 (2003).
[7]J. V. Candy, A. W. Meyer, A. J. Poggio, and B. L. Guidry, "Time-reversal processing for an acoustic communications experiment in a highly reverberant environment," J. Acoust. Soc. Am. **115**(4), 1621–1631 (2004).
[8]G. Ribay, J. de Rosny, and M. Fink, "Time reversal of noise sources in a reverberation room," J. Acoust. Soc. Am. **117**(5), 2866–28720 (2005).
[9]J. V. Candy, D. H. Chambers, C. L. Robbins, B. L. Guidry, A. J. Poggio, F. Dowla, and C. A. Hertzog, "Wideband multichannel time-reversal processing for acoustic communications in highly reverberant environments," J. Acoust. Soc. Am. **120**(2), 838–851 (2006).
[10]B. Van Damme, K. Van Den Abeele, Y. Li, and O. Bou Matar, "Time reversed acoustics techniques for elastic imaging in reverberant and non-reverberant media: An experimental study of the chaotic cavity transducer concept," J. Appl. Phys. **109**(10), 104910 (2011).
[11]B. E. Anderson, M. Clemens, and M. L. Willardson, "The effect of transducer directionality on time reversal focusing," J. Acoust. Soc. Am. **142**(1), EL95–EL101 (2017).
[12]M. Scalerandi, A. S. Gliozzi, C. L. E. Bruno, and K. Van Den Abeele, "Nonlinear acoustic time reversal imaging using the scaling subtraction method," J. Phys. D: Appl. Phys. **41**(21), 215404 (2008).
[13]M. Scalerandi, A. S. Gliozzi, C. L. E. Bruno, D. Masera, and P. Bocca, "A scaling method to enhance detection of a nonlinear elastic response," Appl. Phys. Lett. **92**(10), 101912 (2008).
[14]T. J. Ulrich, A. M. Sutin, T. Claytor, P. Papin, P.-Y. L. Bas, and J. A. TenCate, "The time reversed elastic nonlinearity diagnostic applied to evaluation of diffusion bonds," Appl. Phys. Lett. **93**(15), 151914 (2008).
[15]B. E. Anderson, M. Griffa, T. J. Ulrich, P.-Y. L. Bas, R. A. Guyer, and P. A. Johnson, "Crack localization and characterization in solid media using time reversal techniques," in *Proceedings of the 44th U.S. Rock Mechanics Symposium and 5th U.S.-Canada Rock Mechanics Symposium*, paper No. ARMA-10-154 (2010).
[16]P.-Y. Le Bas, M. C. Remillieux, L. Pieczonka, J. A. Ten Cate, B. E. Anderson, and T. J. Ulrich, "Damage imaging in a laminated composite plate using an air-coupled time reversal mirror," Appl. Phys. Lett. **107**(18), 184102 (2015).
[17]B. E. Anderson, L. Pieczonka, M. C. Remillieux, T. J. Ulrich, and P.-Y. L. Bas, "Stress corrosion crack depth investigation using the time reversed elastic nonlinearity diagnostic," J. Acoust. Soc. Am. **141**(1), EL76–EL81 (2017).
[18]S. M. Young, B. E. Anderson, S. M. Hogg, P.-Y. L. Bas, and M. C. Remillieux, "Nonlinearity from stress corrosion cracking as a function of chloride exposure time using the time reversed elastic nonlinearity diagnostic," J. Acoust. Soc. Am. **145**(1), 382–391 (2019).
[19]F. Ciampa and M. Meo, "Nonlinear elastic imaging using reciprocal time reversal and third order symmetry analysis," J. Acoust. Soc. Am. **131**(6), 4316–4323 (2012).
[20]T. J. Ulrich, B. E. Anderson, P.-Y. L. Bas, C. Payan, J. Douma, and R. Snieder, "Improving time reversal focusing through deconvolution: 20 questions," Proc. Mtgs. Acoust. **16**, 045015 (2012).
[21]J.-L. Thomas, F. Wu, and M. Fink, "Time reversal focusing applied to lithotripsy," Ultrason. Imag. **18**(2), 106–121 (1996).
[22]M. Tanter, J.-L. Thomas, and M. Fink, "Focusing and steering through absorbing and aberating layers: Application to ultrasonic propagation through the skull," J. Acoust. Soc. Am. **103**(5), 2403–2410 (1998).
[23]J.-L. Thomas and M. Fink, "Ultrasonic beam focusing through tissue inhomogeneities with a time reversal mirror: Application to transskull therapy," IEEE Trans. Ultrason. Ferroelectr. Freq. Control **43**(6), 1122–1129 (1996).
[24]S. Dos Santos and Z. Prevorovsky, "Imaging of human tooth using ultrasound based chirp-coded nonlinear time reversal acoustics," Ultrasonics **51**(6), 667–674 (2011).
[25]M. H. Denison and B. E. Anderson, "Time reversal acoustics applied to rooms of various reverberation times," J. Acoust. Soc. Am. **144**(6), 3055–3066 (2018).

[26]M. H. Denison and B. E. Anderson, "The effects of source placement on time reversal focusing in rooms," Appl. Acoust. **156**, 279–288 (2019).
[27]M. L. Willardson, B. E. Anderson, S. M. Young, M. H. Denison, and B. D. Patchett, "Time reversal focusing of high amplitude sound in a reverberation chamber," J. Acoust. Soc. Am. **143**(2), 696–705 (2018).
[28]C. B. Wallace and B. E. Anderson, "High-amplitude time reversal focusing of airborne ultrasound to generate a focused nonlinear difference frequency," J. Acoust. Soc. Am. **150**, 1411–1423 (2021).
[29]B. D. Patchett, B. E. Anderson, and A. D. Kingsley, "The impact of room location on time reversal focusing amplitudes," J. Acoust. Soc. Am. **150**, 1424–1433 (2021).
[30]C. Appert, C. Tenaud, X. Chavanne, S. Balibar, F. Caupin, and D. d'Humieres, "Nonlinear effects and shock formation in the focusing of a spherical acoustic wave," Eur. Phys. J. B **35**, 531–549 (2003).
[31]G. Montaldo, P. Roux, A. Derode, C. Negreira, and M. Fink, "Ultrasound shock wave generator with one-bit time reversal in a dispersive medium, application to lithotripsy," Appl. Phys. Lett. **80**, 897–899 (2002).
[32]S. M. Young, B. E. Anderson, M. L. Willardson, P. E. Simpson, and P.-Y. L. Bas, "A comparison of impulse response modification techniques for time reversal with application to crack detection," J. Acoust. Soc. Am. **145**(5), 3195–3207 (2019).
[33]C. Heaton, B. E. Anderson, and S. M. Young, "Time reversal focusing of elastic waves in plates for educational demonstration purposes," J. Acoust. Soc. Am. **141**(2), 1084–1092 (2017).
[34]R. T. Beyer, *Nonlinear Acoustics* (Acoustical Society of America, Woodbury, NY, 1997), pp. 91–164, 165–203, 299–333.
[35]C. E. Needham, *Blast Waves* (Springer, New York, 2010). pp. 19–22.
[36]E. Mach, "Uber den Verlauf von Funkenwellen in der Ebene und im Raume" ("Over course radiowaves plane space)," Sitzungsbr. Akad. Wiss. Wien **78**, 819–838 (1878).
[37]G. Ben-Dor, *Shock Wave Reflection Phenomena* (Springer Verlag, New York, 1992), pp. 3–13.
[38]M. M. Karzova and V. A. Khokhlova, "Mach stem formation in reflection and focusing of weak shock acoustic pulses," J. Acoust. Soc. Am. **137**(6), EL436–EL442 (2015).
[39]J. N. Tjotta and S. Tjotta, "Nonlinear equations of acoustics, with application to parametric acoustic arrays," J. Acoust. Soc. Am. **69**(6), 1644–1652 (1981).
[40]E. C. Hansen, A. Frank, P. Hartigan, and K. Yirak, "Numerical simulations of Mach stem formation via intersecting bow shocks," High Energy Density Phys. **17**, 135–139 (2015).
[41]R. E. Reisler, L. W. Kennedy, and J. H. Kefer, "High explosive multiburst airblast phenomena (simultaneous and non-simultaneous detonations)," U.S. Army armament research and development command: Ballistic Research Laboratory, technical report (Department of Commerce, Springfield, VA), https://apps. dtic.mil/dtic/tr/fulltext/u2/a068462.pdf (1979) (Last viewed March 10, 2021).
[42]W. A. Willis III, C. E. Tinney, M. F. Hamilton, and J. M. Cormack, "Reduced-order models of coalescing Mach waves," *AIAA SCITECH 2022 Forum*, AIAA 2022-1792 (2021).
[43]A. B. Vaughn, K. M. Leete, K. L. Gee, B. R. Adams, and J. M. Downing, "Evidence for nonlinear reflections in shock-containing noise near high-performance military aircraft," J. Acoust. Soc. Am. **149**(4), 2403–2414 (2021).
[44]B. E. Anderson, T. J. Ulrich, and P.-Y. L. Bas, "Comparison and visualization of the focusing wave fields of various time reversal techniques in elastic media," J. Acoust. Soc. Am. **134**(6), EL527–EL533 (2013).

Chapter 4

Modeling of Nonlinear High-Amplitude Time Reversal Focusing

4.1 Abstract

In acoustics, time reversal processing is most commonly used to exploit multiple scattering in reverberant environments to focus sound to a specific location. Recently, the nonlinear characteristics of time-reversal focusing at amplitudes as high as 200 dB have been reported [Patchett and Anderson, J. Acoust. Soc. Am. **151**(6), (2022)]. These studies were experimental in nature and suggested that converging waves nonlinearly interact in the focusing of waves, leading to some surprising observations (e.g., nonlinear amplification). This chapter investigates the nonlinear interactions and subsequent characteristics from a model-based approach. Utilizing both the k-Wave© package for MATLAB©, and COMSOL Multiphysics©, it is shown that nonlinear interactions between high-amplitude waves leads to free-space Mach-wave coalescence of the converging waves. The number of waves used in both models represents a small piece of the full aperture of converging waves experimentally. Limiting the number of waves limits the number of Mach-stem formations and reduces the nonlinear growth of the focus amplitudes when compared to experiment. However, limiting the number of waves allows the identification of individual Mach waves. Mach wave coalescence leading to Mach-stem formation appears to be the mechanism behind nonlinear amplification of peak focus amplitudes observed in high amplitude time reversal focusing, as hypothesized in the previous work cited in this abstract.

4.2 Introduction

Time-reversal (TR) signal processing is a technique utilized in multiple fields of wave-based physics to focus sound to a chosen position in a given environment.[1-3] The TR process is comprised of two primary steps in order to achieve this focusing. First, in what is typically referred to as the forward step, a source is placed in the environment and an impulse response (IR) is obtained. A swept sine wave, often called a "chirp" signal, may be used as the input signal. The response of the environment to this chirp signal is recorded at a select receiver position. The recorded signal is referred to as the chirp response (CR). The CR is the convolution of the IR of the environment with the chirp that is broadcast by the source. In order to extract the IR, the input chirp signal is cross-correlated with the CR in order to calculate the band-limited IR of the environment. In this way, cross-correlation can be viewed as a practical method of deconvolution to obtain an IR.[10,18]

In the second part of the TR process, called the backward step, the IR is reversed on the time axis (hence the name time reversal) creating the time-reversed impulse response (TRIR). The TRIR can be broadcast into the environment from the original source position resulting in the convergence of the sound waves onto the receiver creating a focus of energy. Because the TR process utilizes reflections within the IR as virtual sources during the backward step, the TR process greatly benefits from reverberant environments when techniques such as beam forming do not benefit from the same environments. The time-symmetric focal signal[46] recorded at the receiver is equivalent to an auto-correlation of the IR.[19] The focused waves approximately create an acoustic impulse that could have created the IR directly in the forward step.

This type of acoustic focusing has been studied for many different applications. It began as a method of reproducible underwater communication that would be difficult to intercept during transmission.[4,5] The field of medicine was an early application of TR focusing research as an

effective means of kidney stone destruction via lithotripsy by utilizing an array of transducers known as a time-reversal mirror.[29] TR has also been used for the histotripsy destruction of tumors, biological soft tissues, and other inhomogeneous bio-materials.[30,31] It has been explored as a communication tool for audible sound in highly-reverberant, airborne environments.[7,9] TR has also been studied as an effective method of focusing sound in different room environments.[6,8] The field of nondestructive evaluation of materials has shown TR to be an effective method of evaluation in solid materials in which defects, or cracks, in the material can be identified by focusing to different locations in the material and observing differences in the nonlinear response of the focused waves.[3]

TR focusing of waves at high amplitudes has many promising applications. In a study conducted by Montaldo *et al.,*[47] the focusing of sound waves in an underwater environment was characterized. They showed that as TRIR amplitudes were increased, the characteristics of the focus waveform noticeably changed. Nonlinear attributes, including shock wave formation, harmonic generation, and reduction of peak amplitudes relative to linear scaling were observable in their work. A study done by Willardson *et al.*[41] made preliminary observations of a nonlinear increase in the peak amplitude of the focus generated using TR of airborne, audible sound at very loud sound levels (this is discussed more later on). High-amplitude focusing of ultrasound was studied by Wallace and Anderson[38] who showed that when ultrasonic waves in two primary frequency bands are co-focused at high levels, a difference frequency in the audible acoustic range can be generated. Recently, Patchett and Anderson[48] characterized the nonlinear features present in the signal when focusing at levels as high as 200 dB. They observed significant nonlinear amplification of peak amplitudes in the TR focusing and described a potential mechanism by which the nonlinearities were generated, known as free-space Mach-stem formation. Waveform steepening was also observed though this did not seem to be the cause of the nonlinear

amplification of compression peaks. These effects were studied and characterized primarily through experimental methods.

In addition to these studies of nonlinearities in TR focusing, several studies have aimed at maximizing the peak focus amplitude in TR. Derode *et al.*[42] introduced one-bit signal processing (a form of intentional clipping of the TRIR) to maximize the amplitude of the focus. A 12 dB increase in amplitude was achieved in an underwater experiment, albeit at the expense of focus quality. In a study done by Heaton *et al.,*[49] a variant of one-bit processing known as clipping, which preserves more energy in the TRIR leading to higher amplitude focusing, was investigated in solid materials. They were able to show an increase in peak focus amplitude employing the clipping method when compared to other TR methods, including one-bit processing. Anderson *et al.*[18] showed that the peak focus amplitude could also be increased by physically reducing the direct sound that arrives at the receiver and relying primarily on the convergence of reflected waves. They did this by pointing the sources away from the receiver position in a reverberant environment, which increased the peak amplitude of the focus signal. In a study by Denison and Anderson[35], the size of a reverberant room in relation to the peak amplitude of the focus was studied. They found that a smaller room would increase the focusing amplitude, even though previous studies had predicted that the shorter reverberation time would decrease it. This finding was confirmed by Patchett *et al.*[40] when they studied the effect of receiver placement on the peak focal amplitude in different environments and through modal summation modeling. The paper showed that when the focusing occurs near walls, edges, and corners of a room that the focal amplitude increases. In a separate study Denison and Anderson[36] found that placing sources further away from the focal location at distances greater than the critical distance, placing sources in the same plane as the focusing, and surrounding the focal location with a limited number of sources (rather than using

them in a line array) all contributed to a larger focal amplitude. A comparison of multiple signal processing methods was done by Willardson *et al.*[41] demonstrating that the clipping method was the most effective TRIR pre-processing technique to employ for maximizing the peak focus amplitude when focusing audible sound in air. Young *et al.*[43] conducted a similar investigation for applications in using ultrasound within solid materials, arriving at the same conclusion.

This chapter presents further work on high-amplitude (often called finite amplitude) focusing of sound through the creation of two types of models to compare qualitatively with the results seen experimentally by Patchett and Anderson.[48] These models demonstrate that, in addition to qualitatively verifying the characteristic nonlinearities already observed experimentally, free-space Mach-stem formation is the primary contributor to the nonlinear amplitude growth observed by Willardson *et al.*[41] and by Patchett and Anderson.[48]

The first model was designed using a well-known MATLAB© (Natick, MA, U.S.A.) package called k-Wave©.[50,51] k-Wave© is an open-source package that accounts for nonlinear wave propagation in custom scenarios. It employs a combination of the finite difference method (for times steps) and the k-space pseudospectral method (for spatial gradients). The k-space pseudospectral method is a frequency domain approach to solving the KZK equation, but it has been shown to provide greater accuracy than using the KZK equation alone through implementation of a correction operator. The KZK equation is primarily intended for plane wave propagation and is limited in modeling the superposition of waves up to an angle of incidence of 20˚ between them. Treeby *et al.*[52] showed that the correction operator within the pseudospectral method accurately models the superposition of waves at any angle of incidence, which is important for our model. The accuracy is limited by the bandwidth of the signal; a band-limited signal will

contain less computational dispersion.[53] The model considered here employs a band-limited signal to generate a propagating pulse.

The k-Wave© package allows the user to place a series of sources and receivers in any 3-dimensional configuration desired in a free-space environment. The properties of the environment are input independently to allow the user to define parameters such as density, sound speed, and the B/A nonlinearity parameter used in nonlinear acoutics.[54] Using these parameters, models can be generated in any type of fluid and the degree of nonlinearity may be modified. A perfectly matched layer (PML) boundary condition is defined to allow for the waves to propagate out of the defined area without reflection or undesirable interactions at the boundaries. At high amplitudes, waves traveling parallel along the boundaries did prove to create very small unnatural fluctuations near the PML, though this effect was minimal. Nonlinear wave propagation is controlled by entering the appropriate B/A value for the fluid. This nonlinear term can also be removed from the calculation for a direct comparison to linearly propagating waves. Utilizing these functions, it is then possible to simulate the convergence of high-amplitude waves as they propagate to a focus position from an array of receivers that are equally spaced from the focus location.

The second type of model employed finite element modeling using the COMSOL Multiphysics© (Burlington, MA, U.S.A.) software package. The COMSOL© package applies the Westervelt equation which employs less assumptions about the nonlinear propagation of waves than does the pseudospectral method. However, it is assumed that both equations are valid for our modeling. The Westervelt equation is known to accurately represent the cumulative effects of the intersecting waves far from the sources. This ability makes COMSOL© a good choice for calculating the complex interactions of the waves as they propagate.[55] The Westervelt equation is known to struggle in modeling the near field of sources. Fortunately, our results are not dependent

on accuracy in the near field of the sources. COMSOL© utilizes a highly complex finite-element mesh grid to create the desired geometry of a space and the desired boundary conditions. Thus it is more computationally efficient at simultaneously modeling the entire propagating wave field than k-Wave, which is intended to calculate the field at user-defined, discrete positions. The COMSOL© software then displays a time waveform animation of the propagating waves. These abilities make COMSOL© an excellent platform for viewing the spatial extent of wave interactions in high resolution.

Both models show that when nonlinearity is accounted for in the propagation of the waves, the wavefronts do indeed coalesce to form a region of higher overall pressure than expected with linear superposition and corresponding higher wave speeds of these finite amplitude waves. The k-Wave© model results indicate that a nonlinear increase relative to linearly scaled amplitudes in focused acoustic waves is present only when multiple high-amplitude acoustic waveforms are emitted. The waveforms also arrive earlier in time and become steeper on their leading edges as the TRIRs are amplified, due to waveform steepening. The waveform steepening also nonlinearly increases the high frequency content of the waves. The results of the COMSOL© modeling clearly show the formation of individual free-space Mach-stem events where the waves have coalesced to form higher than expected (relative to linear superposition) pressure wave fronts. These Mach stems travel at faster wave speeds than the direct waves and eventually the Mach stems and the direct waves coalesce to form one large wave front with peak amplitudes that are nonlinearly larger in amplitude than linearly scaling would predict. The peak focus amplitudes reported by the models are not as high as amplitudes measured in experiments, but the difference is caused by limiting the number of waves coalescing in the TR focusing. This limit occurs because virtual sources were not utilized in these free-space models in order to simplify the models, reduce computation time,

and observe the formation of individual Mach stems. The MATLAB© script used to generate the k-Wave© model is provided in Appendix D, along with helpful tips for correctly placing sources and receivers in a modeled space.

4.3 k-Wave© Model Design

In order to explore the interaction between high-amplitude waves, a simple model was constructed in the k-Wave© open-source software. A circular array of 18 sources was placed on a plane, along with a linear array of 121 receivers. The receivers were oriented in a straight line along the vertical y-axis, and the sources placed in such a way that they formed a full 360˚ circle about the array, with the center receiver being located at the center of the circle of sources (see Figure 4.1). A radial distance of 5 m from each source to the central receiver was used, along with a source radius of 0.25 m. This geometry allows for focusing of the array to the central receiver (from here on referred to as the focus location).

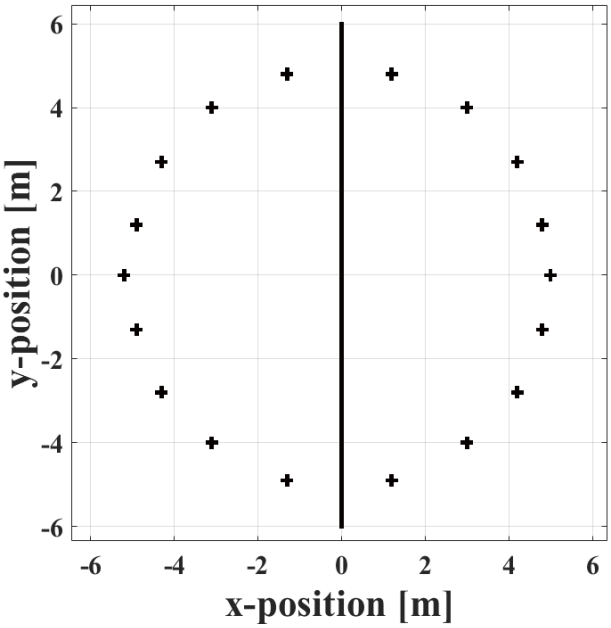

Figure 4.1: *Layout of sources (+) and receivers (|) in the initial 360˚ k-Wave© model.*

A single pulse is sent from each source simultaneously with equal initial pressure amplitude. The pulses all arrive at the focus location simultaneously, creating a focus wave similar in characteristics to a focus generated using TR in free space. To determine if the angle of incidence would affect the peak pressure measured at the focus location, the 18 sources are then moved to fit within a 180˚ aperture. The model is repeated and the results are compared to determine if a closer angle of incidence would increase the amplitudes of the focal signals more than when a 360˚ aperture is used. The angles are decreased again, and the process is repeated. The angles are decreased to the smallest separation that is mechanically possible between sources in the model. The initial source pressure amplitude broadcast from each source was 12,000 Pa, and the nonlinear coefficient of B/A was set to 0.4 for air. Figure 4.2 shows that as the angular spacing between sources is decreased, steepening of the converging wave begins to increase. The peak amplitude occurs at the total aperture angle of 106˚.

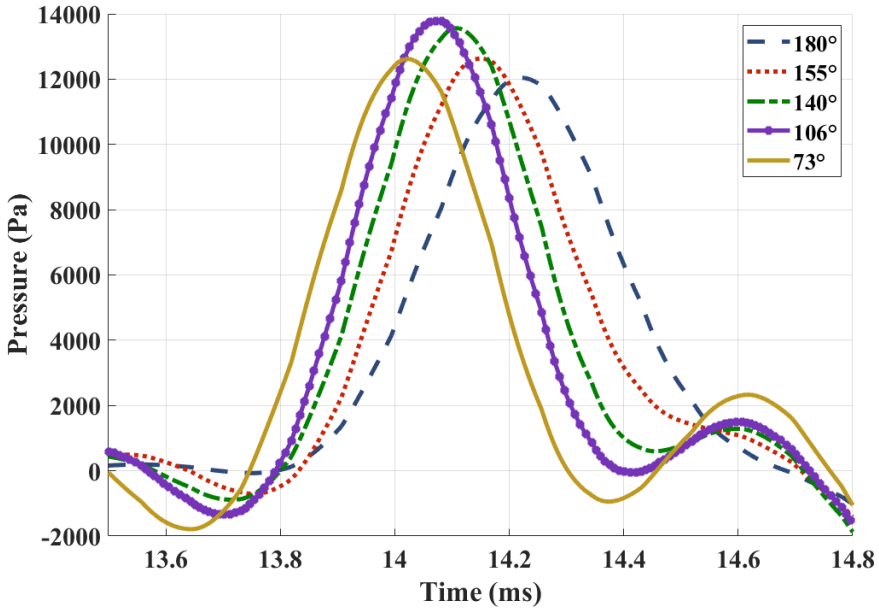

Figure 4.2: Comparison of five example focus signals at the focus location as the total aperture angle of the 18 sources is changed.

The total aperture angle was decreased in several increments, stopping at a total aperture angle of 32˚ as this was the limit in which the sources would fit without overlapping each other in the model. To determine the amount of peak pressure increase caused by the change in aperture angle of the 18 sources, the model was run again with the nonlinearity constant (B/A) removed from the k-Wave© function inputs. Then a comparison of the nonlinear peak amplitudes to the linear peak amplitudes at each aperture angle can be calculated. As expected, the linear model yielded focus signal amplitudes and waveforms that were identical to every other linear broadcast, irrespective of angle, because each source only contributes the primary direct sound wave amplitudes to the focus. The results of a ratio comparison of the nonlinear to linear results are shown in Figure 4.3.

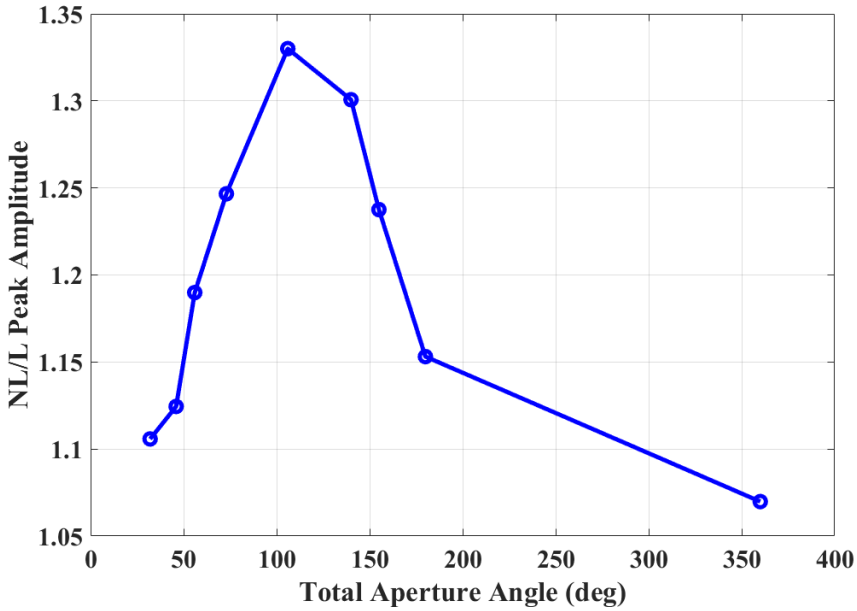

Figure 4.3: Ratio of the peak amplitudes for the nonlinear (NL) and linear (L) models as a function of total aperture angle.

The greatest increase in peak pressure due to nonlinearity happens at a total aperture angle of 106˚, or an optimal source separation angle of 6˚ between adjacent sources. Vaughn *et al.*[56] explored the Mach stems formed by ground reflections of jet noise and their dependence on the so-called critical parameter (that stems from the Khokhlov-Zabolotskaya equation[57]). Using Eq. 1 from Vaughn *et al.* to calculate the approximate critical parameter for the wave amplitudes considered here yields values of around $a \approx 0.2$, suggesting that these wave amplitudes fall within the weak von Neumann regime.

Two metrics for quantifying the degree of wave steepening of the focused waves were employed to show that the change in aperture angle also affects the steepening of the wavefronts generated at the focus location. First, the time of arrival of the peak pressure at the focus location

is compared to the total aperture angle for the sources, shown in Figure 4.4. From this data, we can see that as the total aperture shifts from 360˚ to 73˚ the wavefront advances forward in time, arriving earlier at the focus location. As the total aperture decreases below 73˚, the effect of wave steepening decreases. Thus, a total aperture of 73˚ (an angular spacing of 4˚ between adjacent sources) yields the largest wave steepening effects.

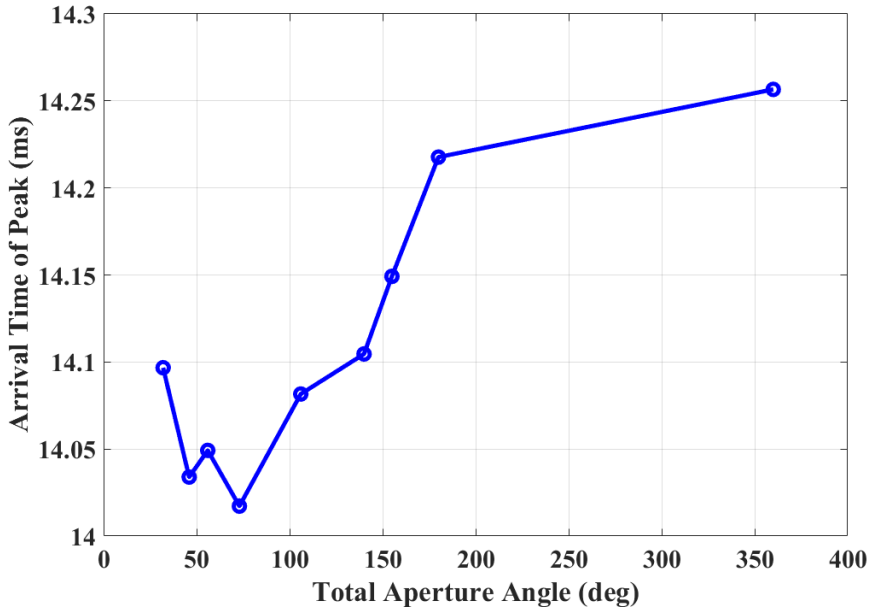

Figure 4.4: Comparison of the time at which the peak pressure point arrives at the focus location versus the total aperture angle that the 18 sources are arranged in.

The second metric used to monitor the differences in wave steepening is the maximum value of the temporal derivative of each time waveform on the leading edge of the wave. These maximal slope values are plotted versus total aperture angle in Figure 4.5. Again, a total aperture angle of 73˚ yields the largest slope due to waveform steepening. The largest slope occurring at a total aperture angle of 73˚ could be an indication that when the adjacent sources are closer than

~4˚ to each other, there is a coupling effect between them, causing the wavefront to move towards a more linearly characterized appearance. Naturally, these numbers can only be assumed for the two-dimensional case described by the model. A more empirical value for them in a real reverberant environment remains to be found.

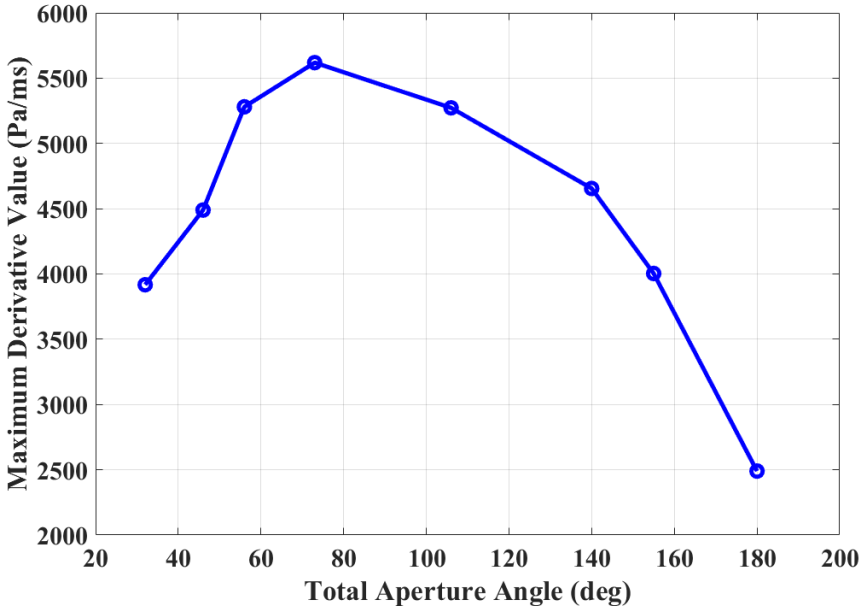

Figure 4.5: Comparison of the temporal derivative of the leading edge of the focusing wave at the focus location versus the total aperture angle that the 18 sources are arranged in.

Using the total angular aperture that generated the maximum nonlinear waveform steepening increase, we now show the increase in peak amplitude and waveform steepening as a function of the amplitude of the source pulses, just as was done in the experiment outlined in Chapter 3. The total aperture for the 18 sources was set to a constant 73˚, and the pressure is increased from 2 to 12 kPa in increments of 2 kPa. These values were chosen because the linear superposition of 18 waves with an initial source pressure value of 2000 Pa would linearly superpose at the focus to a sound pressure level of 174 dB. The experimental studies done by

Willardson *et al.*[41]. and Patchett and Anderson[48] indicate this level can be considered the threshold where nonlinear amplification of peak pressures begins for converging waves created using TR. Figure 4.6 shows the focal signals recorded at the focus. Each data set is scaled linearly by a constant value in order to show the relative nonlinear changes, such as the nonlinear increase of the peak amplitude as the source pressure is increased. As shown experimentally, increasing the output level of the sources does lead to an increasing level of nonlinear interactions between the waves as they converge at the focal location.

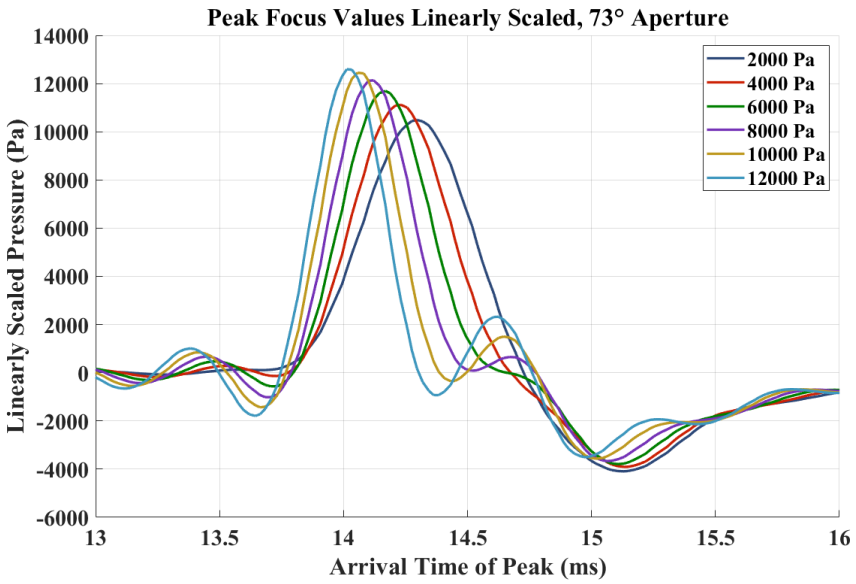

Figure 4.6: Linearly scaled focus peaks at a fixed total aperture angle of 73˚, as the output pressure of the source is increased.

4.4 Linearly Superposed vs. Simultaneously Broadcast Modeled Waves

In addition to the models outlined above, a recreation of the methods of focus generation outlined in Section III-D of Chapter 3 was simulated for comparison using k-Wave©. In this model, eight sources are arranged into a circular array with the same geometric dimensions used in the previous

section, with each source placed 45˚ from its neighbor. The initial source pressure of each is set to 25 kPa. For the first part of the experiment, the eight source broadcasts are done simultaneously, thereby summing together acoustically. In the second part, the eight source broadcasts are done individually and the results are summed electronically in post processing. The experiment now recreates the aforementioned experiment from Ch. 3 that ensures that the nonlinear effects are in fact a direct result of the acoustic mixing of the focus signals. Figure 4.7 shows the two resulting focus signals.

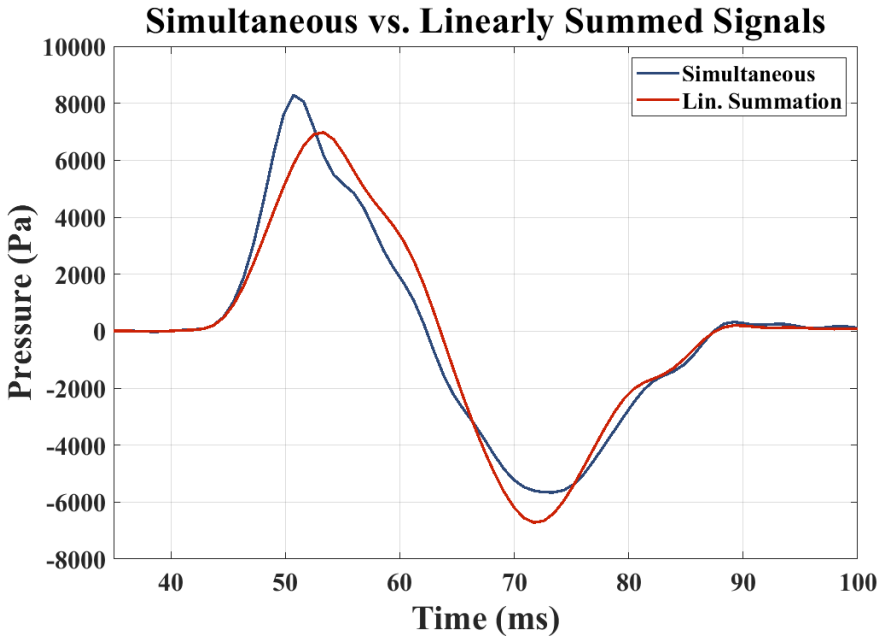

Figure 4.7: A comparison of the linearly summed signals (summed in post processing) from each source in the k-Wave© model, to the field created when all of the sources generate their signals simultaneously.

Figure 4.7 clearly shows that when the signals are generated simultaneously the nonlinear acoustic effects are more pronounced with the focus having a higher amplitude, arriving sooner in

time, and having a steeper leading edge, than it would if the signals were linearly superposed with each other. The result agrees with the experimental data from Chapter 3, though the effect appears to a greater extent in the experimental results due to the higher number of virtual sources from reflections in the reverberation chamber. Calculating the change in the nonlinear amplitude-dependent wave speed in the model for the acoustically mixed signal shows that a peak temperature increase of 2 °C occurs as the peak of the wave propagates. This temperature increase would allow the wave to propagate at such a speed that it would arrive 3 ms sooner than the linearly summed waves, which is the time difference seen in Fig. 4.7.

4.5 COMSOL Multiphysics© Model Design

In addition to the k-Wave© model, a similarly simple model was designed in COMSOL Multiphysics© to visualize individual Mach-stem formations in the focused waves for comparison to the k-Wave© results in two and three dimensions. Linear and nonlinear propagation simulations were conducted. The design of the model matched the dimensions and geometry of the k-Wave© model. Specifically, the radial distance from each source to the center point where the waves converge is 5 m, and each source has a radius of 0.25 m. To better visualize the interaction of the overlapping high-amplitude pulses, eight sources were placed equidistant from a central receiver (also referred to as the focus location here), in a circular arrangement with each source placed 45 degrees from the adjacent sources. Figure 4.8 shows the geometry of the arrangement. This arrangement benefits from COMSOL's ability to capture an entire field with a high-resolution mesh-grid. With the sources at a larger angle of incidence from each other, it is possible to view the individual interactions of overlapping waves with greater detail as they propagate across the region toward the focus location. The software allows observations of individual Mach wave

coalescence events and shows that they contribute to the nonlinear amplification of the peak focus amplitude by arriving at the same time as the initial wave.

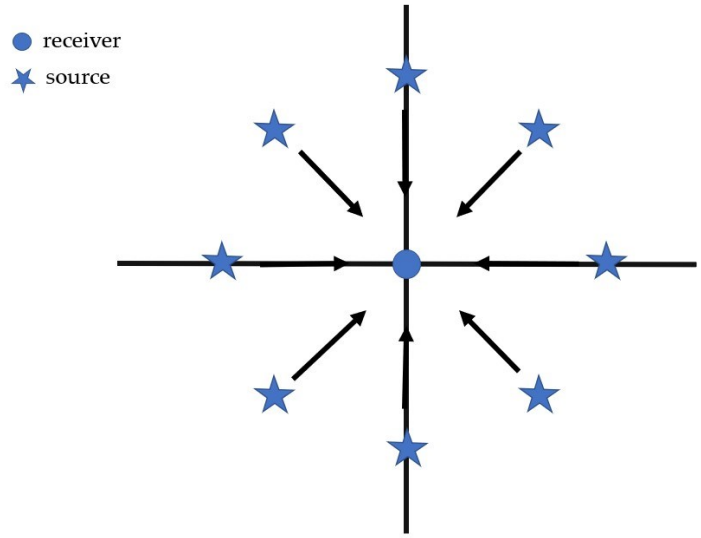

Figure 4.8: Arrangement of sources and receiver for the COMSOL Multiphysics© model of high-amplitude wave interference.

The images in Figures 4.9 and 4.10 are shown at the same time intervals after source emissions, for linear and nonlinear models respectively, to demonstrate that including nonlinear propagation significantly increases the speed of the converging waves. Figures 4.9 (a-c) and 4.10 (a-c) show the source locations as the array of white circles place equidistant from the center of the array. The initial waves propagating outward are shown in dark grey (Fig. 4.9 (a)), with the overlapping regions shown in light grey (constructive interference). Figure 4.9 (b) shows an image 0.7 ms later in time. Additional regions of overlap have happened as the waves converge to the center. And finally, the last image (Fig. 4.9 (c)) shows the propagation an additional 0.7 ms later in time, and has multiple regions of overlap as the waves propagate into the center. The primary

purpose of the zoomed in images (d-f) is to show that the leading edge of the converging waves continues to have a convex shape that maintains a very distinct point where the waves overlap.

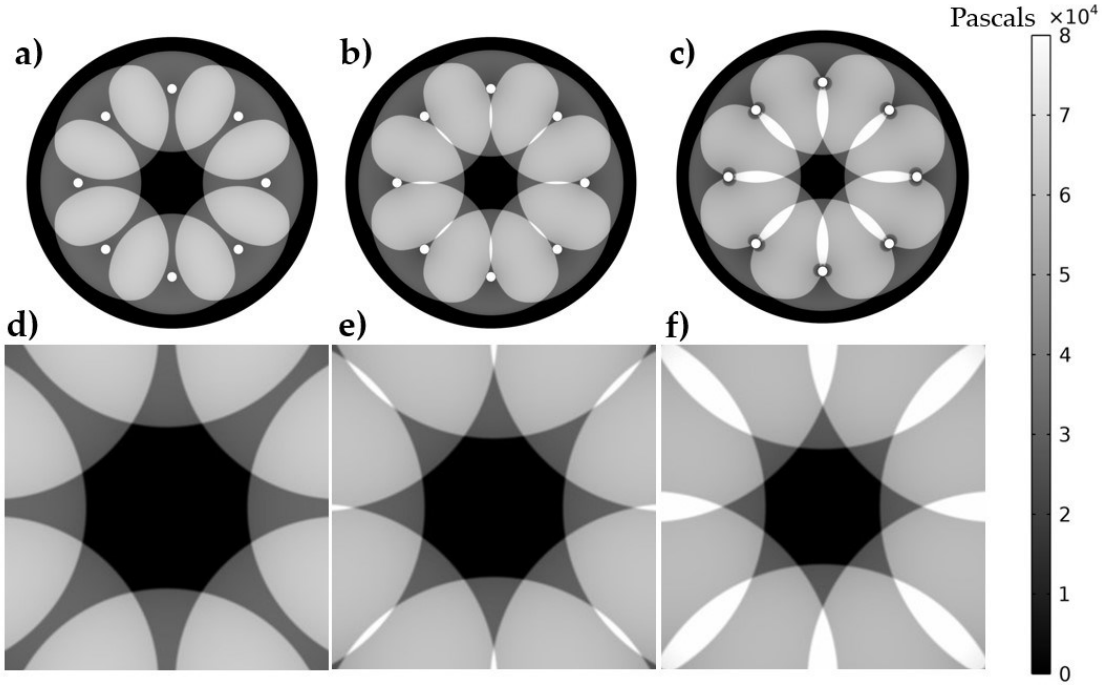

Figure 4.9: COMSOL© images of linear waves propagating from the eight sources. The top row (a-c) shows the full view of the modeled region at 9.3, 10.0, and 10.3 ms respectively, while the second row (d-f) are blown-up images of the center of each above image, respectively.

Essentially, Fig. 4.9 shows that the pressures arriving at the focus are simply the linear superposition of the individual broadcasts, and the shape of the leading edge of the wave is not changed, nor is the expected peak pressure nonlinearly amplified when it reaches the focus.

A comparison of Figs. 4.9 and 4.10 show that the waves in the nonlinear model are traveling faster than the waves in the linear model as evidenced by the smaller black void in the middle of the converging waves for the nonlinear model results. When looking at the zoomed in images of Fig. 4.10 (d-f) one can see that as the waves begin to converge, the overlapping regions

of the leading edges generate a gradient of higher pressure where they interact with the adjacent waves (seen as light grey to white gradations in the overlap regions going left to right through the images). Figure 4.10 is showing that free-space Mach waves are formed in this region and due to the finite amplitude of the coalescing waves, the wave speed of the overlapping amplitudes increases relative to the wave speed of the direct waves from the sources, and that these Mach waves eventually overtake the leading waves and dominate the resulting leading edge of the converging wave front.

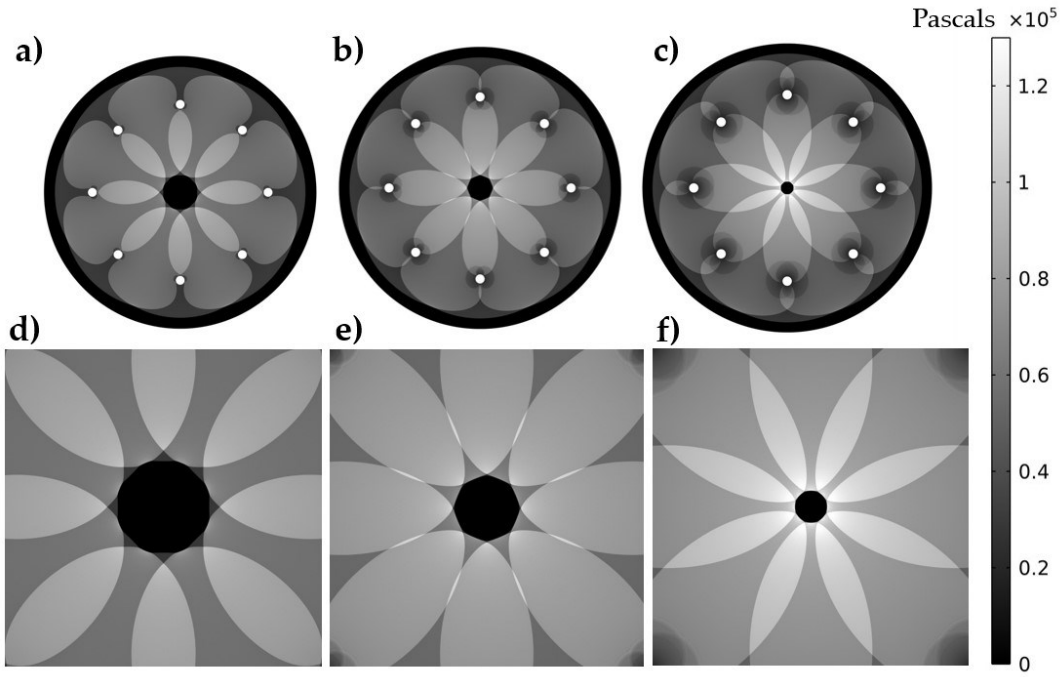

Figure 4.10: COMSOL© images of nonlinear waves propagating from the eight sources. The top row (a-c) shows the full view of the modeled region at 9.3, 10.0, and 10.3 ms respectively, while the second row (d-f) are blown-up images of the center of each above image, respectively.

Because Mach stems take over the leading wavefront, the pressure at the location of focusing has a higher peak amplitude than linear superposition would predict. As the wavefront converges, it also takes on a more circular shape due to the increased number of Mach coalesced wavefronts overtaking the initial leading wave. Figure 4.11 compares the circular shape formed in Figure 4.10 with the convex wavefronts in Figure 4.9. The black central color has been replaced with white to better show the wavefronts that are being compared. Specifically, Fig. 4.11 (a) is a closer look at the linear waves in Fig. 4.9 (b), with the addition of some markers to help the reader clearly identify the waves presented. The waves labeled 'primary waves' in Fig. 4.11 (a) are the initial waves that emanated from the sources.

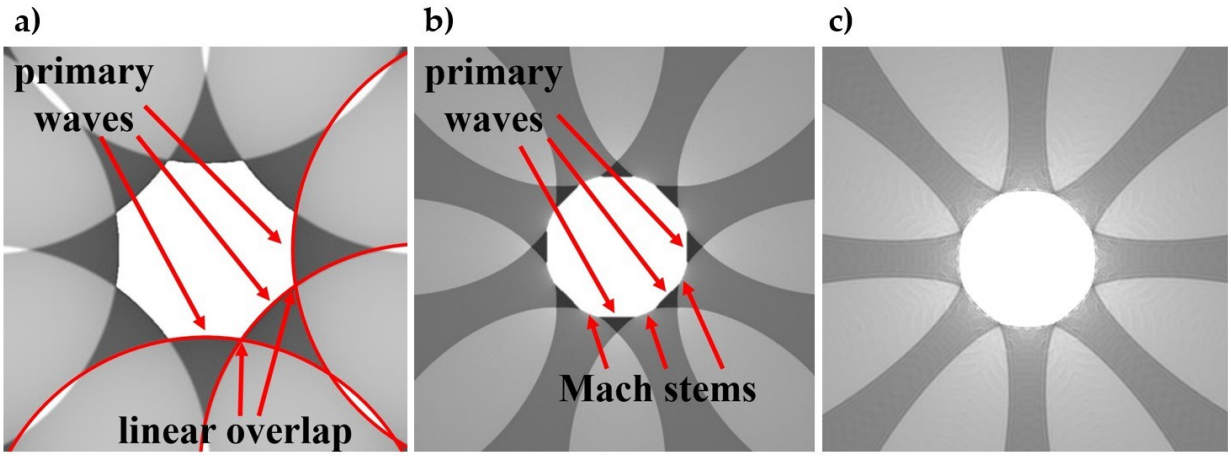

Figure 4.11: a) A zoomed in view of Fig. 4.9 (b) where the linear interaction of the wavefronts is clearly visible. b) A zoomed in view of Fig. 4.10 (a), which happens earlier in time than a), where nonlinear propagation is accounted for, and Mach stems begins to form between each adjacent pair of overlapping primary waves. c) A zoomed in view of Fig. 4.10(c), where the nonlinear propagation has led to the Mach stem waves creating a circular convergence pattern. This image is later in time and not to scale with images a) and b).

The curvature of three of these waves is outlined in red to illustrate better the entire wavefront propagating from each source. The points labeled as 'linear overlap' are the points of intersection between the primary waves, where they begin to overlap. In Fig. 4.11 (b), we see a zoomed in look at the nonlinearly propagating waves shown in Fig. 4.10 (a). The initial wavefronts are again labeled as 'primary waves'. The difference in this image is that where the points of intersection should be, a high-pressure Mach stem has begun to form. These are labeled as 'Mach stems'. This figure more clearly illustrates the differences between the linear superposition of the waves, and the nonlinear superposition of them when all other variables are held the same. In Fig. 4.11 (c) we see a closer view of Fig. 4.10 (c), where the nonlinear high-amplitude waves have converged to form a circle almost completely comprised of Mach stems.

4.6 Conclusion

The results from the k-Wave© model, while limited in scope, show direct evidence that the convergence of high-amplitude waves to a focus location leads to a similar nonlinear increase of peak amplitudes as seen in experimental data by Patchett and Anderson.[48] It is clear that when finite amplitude waves are focused, the peak focus amplitude increases nonlinearly and shifts forward in time. This verifies qualitatively that the nonlinear increases seen in the experimental results are not the result of equipment artifacts. Though not reported here, the spectrum of the focal signals also shows a nonlinear increase in high frequency content, as was also observed experimentally, which is a sign of waveform steepening. The k-Wave© model recreation of the experiment conducted by Patchett and Anderson[48] further verifies that a nonlinear acoustic mixing of the waves leads to the nonlinear increase of the peak focus amplitude as the waves converge. The results support the free-space Mach stem hypothesis that the converging waves are interacting

in such a way that peak focus amplitudes are nonlinearly larger than linear superposition would predict. This interaction was hypothesized by Patchett and Anderson.[48]

This free-space Mach stem hypothesis was confirmed with modeling done in COMSOL Multiphysics©. The geometric arrangement and ability to finely mesh the region of focusing allowed for clear high-resolution images of the formation of Mach stems. These models showed that Mach-stem formations in free space do indeed occur when high-amplitude waves converge toward a focus location. The effect is so dramatic that in fact the coalescing waves become the primary contributions to the circular wavefront that reaches the focal location, overtaking the initial wavefronts produced by the sources. Wave steepening is observed in both of the two models, which results in the peak focal amplitude arriving earlier in time and with a steeper leading edge of the peak wave. These two modeling methods have also confirmed that the formation of free-space Mach stems through Mach wave coalescence also occurs and is the mechanism behind the nonlinear amplification of the focus peak growth seen in the high amplitude TR focusing reported by Willardson *et al.*[41] and Patchett and Anderson.[48]

Chapter 5

Conclusion

5.1 Summary

In Chapter 1 of this dissertation, an introduction and overall view of time reversal (TR) signal processing is given from both a practical and theoretical perspective. Experimental techniques are outlined in conjunction with the fundamental mathematical principles that underlie the computational aspects of doing TR in most general circumstances. The most commonly known applications of signal processing techniques are outlined with a brief description of the expected outcome from each one, and the two common modeling methods of image source and modal summation are then outlined with details as to any benefits or drawbacks when using either.

Chapter 2 is a reproduction (under copyright license) of an article published in the Journal of the Acoustical Society of America. This article outlines an observed experimental phenomenon related to using TR focusing near a reflective surface in a reverberant environment. This work shows that when focusing near a single solid surface the peak of the focus is increased by approximately 3 dB. An additional 3 dB is gained on top of that when near two solid surfaces, and yet another 3 dB for being near three solid surfaces, totaling an approximate increase of 9 dB when comparing a focus in the free-field of the environment to a focus in the corner. Multiple measurements are taken in both a large and small reverberation chamber, also confirming a prior finding by Denison and Anderson[35] that a smaller volume room will contribute to a higher peak focus amplitude as well. The two reverberation chambers are then modeled using the modal summation method, and the experimental results are confirmed in the modeling. A theoretical solution is proposed with the accompanying mathematics to show that theory, experiment, and

modeling all align. The results of the article contained in this chapter confirm the empirical experimental results of focusing near solid surfaces in a reverberant environment. Specifically, that one can expect an increase in the peak focus amplitude when focusing near one or more surfaces compared to the free-field environment of the space.

An overall characterization of the nonlinear effects of high-amplitude TR focusing is the subject of Chapter 3. This chapter is also a reproduction (under copyright license) of an article published in the Journal of the Acoustical Society of America. In this article, the nonlinear characteristics of the focus are investigated as the source output level is increased in the reverberant environment. Techniques for high-amplitude focusing are covered, and an explanation of the effect of each is given. As the source output level is increased, the peak amplitude of the focus grows faster than the linear approximation would suggest. This difference implies that some change in the acoustic wave propagation at high amplitude is happening at the focus. A confirmation of the measurement values is done by comparing the results with multiple microphone/transducers. An experiment is done comparing the linear superposition of each focus created by individual sources with the focus generated when all sources are used simultaneously. The result confirms that the nonlinear growth of the peak focus amplitude is directly correlated to the acoustic mixing of the waves as they propagate simultaneously to the focus position. This result led to the definition of a nonlinear threshold value, a value which can define where the nonlinearity of the propagation becomes significant. This experiment leads to the hypothesis of a free-space Mach stem formation, or Mach wave coalescence, that would increase the pressure of the focus beyond a simple linear approximation value. A linear 1D scan of the focus is made to observe the convergence of the focus waves as they propagate inward and then outward after focusing. This allows for an approximation of the spatial width, density, and temperature at the focus. The results of this paper

confirm several nonlinear characteristics of high-amplitude TR focusing. A definition for a nonlinear threshold that can determine if one is working in a linear or nonlinear regime is defined to guide future investigators who may explore high-amplitude focusing. The hypothesis of free-space Mach stem formation is put forward as an explanation for the nonlinear increase in peak focus amplitudes observed experimentally.

Chapter 4 is a draft of a paper to be submitted for publication in the Journal of the Acoustical Society of America. The modeling done furthers the experimental work done in Chapter 3 by modeling the focusing of high-amplitude waves in both k-Wave© and COMSOL Multiphysics©. The results of the k-Wave© model show that when nonlinear propagation is included in the calculations for the source waves, the peak focus amplitudes grow beyond the linear approximations just as they do experimentally. Additional work shows that the aperture angle of the sources used for focusing has a significant effect on the peak amplitudes as well. These results indicate the existence of an optimal angle of incidence at which the converging waves coalesce to generate an increase in the peak pressure at the focus. The experiment in Chapter 3 is recreated in k-Wave© to confirm the experiment through modeling. The model produces qualitatively similar results to experiment, showing that the simultaneous broadcast of the focus signals leads to nonlinear acoustic effects. Increasing the peak focus amplitude beyond a linear superposition of the waves individually. COMSOL Multiphysics© is then used to design a simple model of nonlinear waves converging to a focus point at the center of a circle of eight sources. This model produces a high-resolution image of the wave as it propagates, showing clearly that a free-space Mach stem does indeed form where the high-amplitude waves intersect with each other. These waves have both a higher speed of sound due to the breakdown of linear adiabatic assumptions and a higher pressure than the linear superposition of the waves individually.[58] The higher speed

of sound creates a converging wavefront that arrives sooner in time (due to wave steepening) and at higher pressure than expected, confirming that the mechanism behind the nonlinear growth in the peak of the focus is due to the formation of these free-space Mach stems when high-amplitude acoustic waves intersect each other while converging to the focus.

Appendix A is the reproduction (under copyright license) of an article published in the Journal of the Acoustical Society of America, in which I was a contributing author. My primary contribution to this work was in the collection of high-amplitude focusing data, the refining of the focusing process, and the empirical finding of several variable values of interest to the authors. The results show that of all of the signal processing techniques available, the clipping technique is the most effective at maximizing the peak amplitude of the focus, and that placing the receiver in the corner of a room produces the highest possible pressure of any other position in the space. The article was also the first to report an observation of nonlinear increase of the peak focus amplitude when focusing at high levels.

Appendix B is the reproduction (under copyright license) of an article published in Applied Acoustics, in which I was a contributing author. In this article, active noise control, (ANC), is used to reduce the sound of an MRI for patients undergoing a scan. A comparison to the TR inverse filter approach is given and is shown to be equivalent to the stationary ANC approach. My primary contribution to this work included a full exploration of experimental measurements using various TR techniques to determine if it was more/less/equal to ANC. The resulting data showed that the TR inverse filter is equivalent to stationary ANC. In addition, the incorporation of TR techniques, (shorter reverberation times, multiple sources of control), into the ANC process could help to reduce the noise generated at a given location with greater temporal accuracy, and amplify the noise outside of the control location less than stationary ANC.

Finally, Appendices C and D contain the MATLAB© scripts used for the majority of the modeling simulations used throughout the chapters of this dissertation.

5.2 Conclusion

The work put forward in this dissertation has characterized the effects of room geometry, receiver placement, signal processing techniques, and multiple methods of modeling for high-amplitude TR focusing of acoustic waves in a highly reverberant environment. It has been shown that focusing near a reflecting surface increases the peak pressure and that focusing near additional surfaces increases the pressure again by the same amount. Focusing in rooms of smaller volume also increases the peak focus amplitude when compared to those of larger volumes. Even though longer reverberation times (within a given room) have been shown to increase the amplitude, the effect of a smaller room outweighs the negative effect of a shorter reverberation time on the focus in that smaller room. When a chirp signal, which is logarithmically weighted, is used as the input to the system for calculating the impulse response (IR), the focus amplitude also increases due to the longer time spent at lower frequencies where the reverberation time is longer, allowing the lower frequency modes to develop more strength in the focusing. The pre-processing technique known as clipping also contributes a significant amount to the peak focus amplitude when compared to other techniques. The contribution is due to the increase in overall acoustic energy when the time reversed impulse response (TRIR) is broadcast by the sources. When combined in experimental practice, or in modeling, these techniques have been shown to produce the highest possible peak focus amplitude using TR.

The most significant discovery made in this work is that the formation of free-space Mach stems does indeed occur due to the coalescence of high-amplitude acoustic waves at shallow angles

of incidence, (approximately 4˚ as shown in Chapter 4). The confirmation of this hypothesis was shown in both the k-Wave© and COMSOL Multiphysics© modeling done in Chapter 4. The interaction between high-amplitude acoustic waves being the main factor in the nonlinear amplification of the focus was confirmed in both experiments (Chapter 3) and modeling using k-Wave© (Chapter 4). This work has led to a clearer understanding of how high-amplitude focusing can lead to significant nonlinear characteristics, and this understanding can be accounted for when applying these techniques to applications of TR such as focusing limited bandwidth signals to a large face of a structure, inciting mechanical vibration.

5.3 Ongoing and Future Work

Current work in high amplitude focusing is exploring several paths toward expanding our understanding both experimentally and theoretically.

In order to verify empirically that it is the convergence of waves in 3D that leads to the nonlinear amplification of the TR focus peaks (allows Mach stems to form), a TR experiment in 1D is being conducted by an undergraduate student, Michael Hogg. This experiment is done using a pipe system with several branches, each with a source, that allows for high-amplitude plane waves to be focused in 1D. The hypothesis is that if the waves converging to the focus do not have the opportunity to interact at any finite-aperture angle, then the nonlinear growth of the peak focus amplitude should not occur. If confirmed, this work would verify that it takes an angular aperture of interaction for Mach stems to form in the focus with more pressure than is predicted with linear scaling. Nonlinearity due to high-amplitude is still expected to be present in the form of waveform steepening. This indicates that the speed of sound is increasing for the finite-amplitude focusing

waves and results in an increase in high frequency content. Preliminary results are showing exactly what we expect.

To expand upon the linear scan performed in the article comprising Chapter 3, a set of two-dimensional spatial scans of the focus are being studied by undergraduate student Jay Clift. The hope is that these scans can be used to better investigate the particle velocity as the focus waves converge. Viewing the convergence of the focus in two dimensions is currently yielding insights previously unknown concerning how the focus is formed at very high amplitudes. Additionally, focusing among several Styrofoam™ beads has led to the discovery that an uneven flow is present in the convergence and divergence of the waves in the focus. Current work is being done to investigate why, when a focus is centered among the beads, there is a net flow outward from the focus location. If the process were linear, the converging waves during focus generation would balance the forces in all directions of the diverging waves after the focus event, leaving the beads in their original locations. But observations show that the outgoing waves apply a greater force to the Styrofoam™ beads than the incoming waves, as the beads have a net displacement *away* from the center of focusing. The net displacement could be an indicator of several things happening during the focusing, one of the likely candidates being a net flow of fluid caused by the focusing event. There are plans for me to use high speed video equipment (available through Utah Valley University) to image these Styrofoam™ beads. On a related topic, we have been investigating the cause for how TR focusing can be used to blow out a candle with the lit wick placed at the focus location after obtaining the IR. Investigations into the exact cause are still ongoing. The current thought is that the net flow outward caused by a temporary and partial vacuum at the focus location starves the candle of oxygen to put it out.

Clift has also expanded upon the work described in Chapter 2 by revisiting the modal summation modeling, the image source modeling, and experiments. He found through careful investigation that the increase near each additional wall boundary was a doubling of pressure or a 6 dB increase. I was heavily involved in the planning and discussions of the results and there were many subtleties discovered during Clift's work that were not obvious to us from the outset. His work did not invalidate the work published in Chapter 2; rather he found that the doubling occurs only when the time-reversed impulse response is not normalized, whereas the work in Chapter 2 employed normalization (since normalization is almost always used in experimental implementations of TR). Clift wrote a draft of a manuscript, that I am a coauthor on, and we intend to revise and submit it at some point.

The most significant work currently underway is a project funded by Sandia National Laboratory. This study is intended to see if it is possible to remotely focus high-amplitude sound with very specific frequency content and long time duration to a large cross-section of an object, thereby exciting vibrations in the object with a very specific bandwidth. This project has some very promising applications in remotely exciting objects with sound to study the object's structural integrity and could lead to extended funding in the future.

The future of this research has multiple paths of investigation open to it. One of the important studies would be to determine the exact amount of nonlinear amplification that can be expected when focusing at known high-amplitude levels in a given room. Data can be collected empirically by comparing linear focusing levels and nonlinear focusing levels in varying environments and with multiple source configurations. One could then extrapolate an expected value for the increase caused by Mach stem formation. These experiments could potentially be modeled using k-Wave© or COMSOL© as well to verify the empirical findings.

Another idea would be to determine if it's possible to measure the temperature at the time of focus with a fast enough thermocouple or other measurement device. The measured temperature could be compared to the estimates of temperature given in Chapter 3. With the temperature and pressure measured, a value for the density of the focus could be calculated. A better estimate of the temperature and pressure would allow for a more accurate estimate of the potential energy that is present at the time of focus.

Additionally, further study into the details of the kinetic and potential energy of the waves as they converge to the focus and then diverge away as a singular spherically propagating wave are underway. By understanding these energies better additional insight into the mechanisms at work in the formation of nonlinearities present in the focus.

Development of metrics for determining the nonlinearities involved in high amplitude focusing have been initiated, including a mathematical definition for the spatial steepness of the wave as it converges toward the focus. The difficulty has been that all common nonlinear equations contain the assumption that the acoustic wave is continuous, whereas the waves approaching the focus in TR experiments are often transient in nature. Likely a new equation needs be derived from the Navier-Stokes equations for transient nonlinear events.

Optimization of the MATLAB© script that was created for the modal summation model described in Chapter 2 is currently being studied by undergraduate student Bryce Lundstrom. It should be possible to reduce the number of modes being summed at each position to just those nearest the central frequency that contribute amplitudes of significance, thus drastically reducing the computational time required while remaining accurate in its calculations.

Originally the potential of using TR for replicating the acoustics of explosive events was hypothesized. This idea still seems valid and would prove valuable to the study of hearing

protection for military personnel that are exposed to high levels of impulsive sound. By focusing near the KEMAR mannequin, it would be possible to test the amplitude dependent effectiveness of all sorts of hearing protection when loud impulsive sound is near the subject.

Finally, the idea of using Schlieren imaging to identify the Mach stem has proved difficult. But I believe it is a possible task. While this approach may not lead to any scientific or quantitative insights, it would serve as an excellent visual for future publications and presentations, and may prove quantitatively valuable if captured correctly.

References

1 M. Fink, “Time reversed acoustics,” *Phys. Today* **50**(3), 34-40 (1997).

2 B. E. Anderson, M. Griffa, C. Larmat, T. J. Ulrich, and P. A. Johnson, “Time reversal,” *Acoust. Today* **4**(1), 5-16 (2008).

3 B. E. Anderson, M. C. Remillieux, P.-Y. Le Bas, and T. J. Ulrich, “Time reversal techniques,” Chapter 14 in *Nonlinear Acoustic Techniques for Nondestructive Evaluation, 1st Edition*, Editor Tribikram Kundu, ISBN: 978-3-319-94476-0 (Springer and Acoustical Society of America), pp. 547-581 (2018).

4 A. Parvulescu and C.S. Clay, “Reproducibility of Signal Transmissions in the Ocean,” *Radio Electron. Eng.* **29**(4), 223-228 (1965).

5 C. S. Clay and B. E. Anderson, “Matched signals: The beginnings of time reversal,” *Proc. Meet. Acoust.* **12**(1), 055001 (2011).

6 S. Yon, M. Tanter, and M. Fink, “Sound focusing in rooms: The time-reversal approach,” *J. Acoust. Soc. Am.* **113**(3), 1533–1543 (2003).

7 J. V. Candy, A. W. Meyer, A. J. Poggio, and B. L. Guidry, “Time-reversal processing for an acoustic communications experiment in a highly reverberant environment,” *J. Acoust. Soc. Am.* **115**(4), 1621–1631 (2004).

8 G. Ribay, J. de Rosny, and M. Fink, "Time reversal of noise sources in a reverberation room," *J. Acoust. Soc. Am.*, **117**(5), 2866-28720 (2005).

9 J. V. Candy, D. H. Chambers, C. L. Robbins, B. L. Guidry, A. J. Poggio, F. Dowla, and C. A. Hertzog, “Wideband multichannel time-reversal processing for acoustic communications in highly reverberant environments,” *J. Acoust. Soc. Am.* **120**(2), 838–851 (2006).

10 B. Van Damme, K. Van Den Abeele, Y. Li, and O. Bou Matar, "Time reversed acoustics techniques for elastic imaging in reverberant and nonreverberant media: An experimental study of the chaotic cavity transducer concept," *J. Appl. Phys.* **109**(10), 104910 (2011).

11 M. Scalerandi, A. S. Gliozzi, C. L. E. Bruno, and K. Van Den Abeele, “Nonlinear acoustic time reversal imaging using the scaling subtraction method,” *J. Physics D: Appl. Phys.* **41**(21), 215404 (2008).

12 M. Scalerandi, A. S. Gliozzi, C. L. E. Bruno, D. Masera, and P. Bocca, “A scaling method to enhance detection of a nonlinear elastic response,” *Appl. Phys. Lett.* **92**(10), 101912 (2008).

13 T. J. Ulrich, A. M. Sutin, T. Claytor, P. Papin, P.-Y. Le Bas, and J. A. TenCate, "The time reversed elastic nonlinearity diagnostic applied to evaluation of diffusion bonds," *Appl. Phys. Lett.* **93**(15), 151914 (2008).

14 B. E. Anderson, M. Griffa, T. J. Ulrich, P.-Y. Le Bas, R. A. Guyer, and P. A. Johnson, "Crack localization and characterization in solid media using time reversal techniques," *Am. Rock Mech. Assoc.*, #10-154 (2010).

15 P.-Y. Le Bas, M. C. Remillieux, L. Pieczonka, J. A. Ten Cate, B. E. Anderson, and T. J. Ulrich, "Damage imaging in a laminated composite plate using an air-coupled time reversal mirror," *Appl. Phys. Lett*. **107**(18), 184102 (2015).

16 B. E. Anderson, L. Pieczonka, M. C. Remillieux, T. J. Ulrich, P.-Y. Le Bas, "Stress corrosion crack depth investigation using the time reversed elastic nonlinearity diagnostic," *J. Acoust. Soc. Am*. **141**(1), EL76–EL81 (2017).

17 S. M. Young, B. E. Anderson, S. M. Hogg, P.-Y. Le Bas, and M. C. Remillieux, "Nonlinearity from stress corrosion cracking as a function of chloride exposure time using the time reversed elastic nonlinearity diagnostic," *J. Acoust. Soc. Am.*, **145**(1), 382-391 (2019).

18 B. E. Anderson, M. Clemens, and M. L. Willardson, "The effect of transducer directionality on time reversal focusing," *J. Acoust. Soc. Am*., **142**(1), EL95-EL101 (2017).

19 M. Tanter, J.-L. Thomas, and M. Fink, "Time reversal and the inverse filter," *J. Acoust. Soc. Am.,* **108**(1), 223–234 (2000).

20 D. M. Pepper, "Nonlinear optical phase conjugation," *Opt. Eng*. **21**, 156-183 (1982).

21 *Optical Phase Conjugation*, edited by R. A. Fisher (Academic, New York, 1983).

22 A. Yariv, *Optical Electronics* (Holt, Rinehart, and Winston, New York, 1985), pp. 499-526.

23 M. I. Skolnik and D. D. King, "Self-phasing array antennas," *IEEE Trans. Antennas Propag*., **AP-12**, 142-149 (1964).

24 W. L. Weeks, *Antenna Engineering* (McGraw-Hill, New York, 1968), pp. 129-131.

25 0. Ikeda, "An image reconstruction algorithm using phase conjugation for diffraction-limited imaging in an inhomogeneous medium" *J. Acoust. Soc. Am.* **85**, 1602-1606 (1989).

26 D. R. Jackson and D. R. Dowling, "Phase Conjugation in Underwater Acoustics," *J. Acoust. Soc. Am.* **89**(1), 171–181 (1990).

27 A. Sutin, B. Libbey, V. Kurtenoks, D. Fenneman, and A. Sarvazyan, "Nonlinear detection of land mines using wide bandwidth time-reversal techniques," *Proc. of SPIE,* **6217**, 62171B1- 62171B12 (2006).

28 F. Ciampa and M. Meo, "Nonlinear elastic imaging using reciprocal time reversal and third order symmetry analysis," *J. Acoust. Soc. Am*. **131**(6), 4316–4323 (2012).

29 J.-L. Thomas, F. Wu, and M. Fink, "Time reversal focusing applied to lithotripsy," *Ultrasonic. Imag.* **18**(2), 106–121 (1996).

30 M. Tanter, J.-L. Thomas, and M. Fink, "Focusing and steering through absorbing and aberating layers: application to ultrasonic propagation through the skull," *J. Acoust. Soc. Am.* **103**(5), 2403–2410 (1998).

31 J.-L. Thomas and M. Fink, "Ultrasonic beam focusing through tissue inhomogeneities with a time reversal mirror: application to transskull therapy," *IEEE Trans. Ultrason. Ferroelect. Freq. Contr.* **43**(6), 1122–1129 (1996).

32 S. Dos Santos and Z. Prevorovsky, "Imaging of human tooth using ultrasound-based chirp-coded nonlinear time reversal acoustics," Ultrason. **51**(6), 667–674 (2011).

33 C. S. Larmat, R. A. Guyer, and P. A. Johnson, "Time-reversal methods in geophysics," *Phys. Today* **63**(8), 31–35, (2010).

34 C. S. Larmat, J. Tromp, Q. Liu, and J.-P. Montagner, "Time reversal location of glacial earthquakes," *J. Geophys. Res.*, **113**(B9), B09314-B09323 (2008).

35 M. H. Denison and B. E. Anderson, "Time Reversal Acoustics Applied to Rooms of Various Reverberation Times." *J. Acoust. Soc. Am.* **144**(6), 3055–3066 (2018).

36 M. H. Denison and B. E. Anderson, "The effects of source placement on time reversal focusing in rooms," *Appl. Acoust*. **156**, 279-288 (2019).

37 B. E. Anderson, M. Clemens, and M. L. Willardson, "The effect of transducer directionality on time reversal focusing," *J. Acoust. Soc. Am*. **142**(1), EL95-EL101 (2017).

38 C. B. Wallace and B. E. Anderson, "High-amplitude time reversal focusing of airborne ultrasound to generate a focused nonlinear difference frequency," *J. Acoust. Soc. Am.***, 146**(4), 1411-1423 (2021).

39 T. S. Furlong, B. E. Anderson, B. D. Patchett, and S. D. Sommerfeldt, "Active noise control using remotely placed sources: Application to magnetic resonance imaging noise and equivalence to the time reversal inverse filter," *Appl. Acoust.*, **176**, 107902 (2020).

40 B. D. Patchett, B. E. Anderson, and A. D. Kingsley, "The impact of room location on time reversal focusing amplitudes," *J. Acoust. Soc. Am.,* **150**(2)**,** 1424-1433 (2021).

41 M. L. Willardson, B. E. Anderson, S. M. Young, M. H. Denison, and B. D. Patchett, "Time reversal focusing of high amplitude sound in a reverberation chamber," *J. Acoust. Soc. Am.***, 143**(2), 696-705 (2018).

42 A. Derode, A. Tourin, M. Fink, "Limits of time-reversal focusing through multiple scattering: Long-range correlation." *J. Acoust. Soc. Am.*, **107**(6), 2987–2998 (2000).

43 S. M. Young, B. E. Anderson, M. L. Willardson, P. E. Simpson, and P.-Y. Le Bas, "A comparison of impulse response modification techniques for time reversal with application to crack detection," *J. Acoust. Soc. Am.*, **145**(5), 3195-3207 (2019).

44 A. S. Gliozzi, M. Scalerandi, and P. Antonaci, "One-channel time-reversal acoustics in a highly attenuating media," *J. Phys. D: Appl. Phys.*, **46**, 135502 (2013).

45 J. B. Allen and D. A. Berkley, "Image method for efficiently simulating small-room acoustics," *J. Acoust. Soc. Am.* **65**(4), 943–950 (1979).

46 T. J. Ulrich, M. Griffa, and B. E. Anderson, "Symmetry-based imaging condition in time reversed acoustics," J. Appl. Phys. **104**(6), 064912 (2008).

47 G. Montaldo, P. Roux, A. Derode, C. Negreira, and M. Fink, "Ultrasound shock wave generator with one-bit time reversal in a dispersive medium, application to lithotripsy," Appl. Phys. Lett. 80, 897–899 (2002).

48 B. D. Patchett and B. E. Anderson, "Nonlinear characteristics of high amplitude focusing using time reversal in a reverberation chamber," J. Acoust. Soc. Am. **151**, 3603-3614 (2022). https://doi.org/10.1121/10.0011517

49 C. Heaton, B. E. Anderson, and S. M. Young, “Time reversal focusing of elastic waves in plates for an educational demonstration,” J. Acoust. Soc. Am. **141**(2), 1084-1092 (2017).

50 B. E. Treeby, J. Budisky, E. S. Wise, J. Jaros, and B. T. Cox, "Rapid calculation of acoustic fields from arbitrary continuous-wave sources," J. Acoust. Soc. Am., **143**(1), 529-537, 2018.

51 B. E. Treeby, J. Jaros, D. Rohrbach, and B. T. Cox, "Modelling elastic wave propagation using the k-Wave MATLAB toolbox," IEEE Int. Ultrason. Symp., pp. 146-149, 2014.

52 B. E. Treeby, J. Jaros, A. P. Rendell, and B. T. Cox, “Modeling nonlinear ultrasound propagation in heterogeneous material using a k-space pseudospectral method,” J. Acoust. Soc. Am., **131**(6), 4324-4336 (2012).

53 J. L. Robertson, B. T. Cox, and B. E. Treeby, “Quantifying numerical errors in the simulation of transcranial ultrasound using pseudospectral methods,” IEEE Int. Ultrason. Symp., Chicago, USA, 2014. http://www.k-wave.org/papers/2014-Robertson-IEEEIUS.pdf , accessed 11/10/2022.

54 R. T. Beyer, Nonlinear Acoustics (Acoustical Society of America, Woodbury, NY, 1997), pp. 91–164, 165–203, 299–333.

55 Y. Jing, D. Shen, and G. T. Clement, “Verification of the Westervelt equation for focused transducers,” IEEE Transac. On Ultrason., Ferroelec., and Freq. Contr., **58**(5), 1097-1101 (2011).

56 A. B. Vaughn, K. M. Leete, K. L. Gee, B. R. Adams, and J. M. Downing, “Evidence for nonlinear reflections in shock-containing noise near high-performance military aircraft,” **149**(4), 2403-2414 (2021). https://doi.org/10.1121/10.0003932

57 E. A. Zabolotskaya and V. R. Khokhlov, “Quasi-plane waves in the non-linear acoustics of confined beams,” Sov. Phys. Acoust. **15**, 35–40 (1969)

58 G. Ben-Dor, Shock Wave Reflection Phenomena (Springer Verlag, New York, 1992), pp. 3–13.

Appendix A

A.1 Introduction

The following article, in which I am a co-author, represents my initial work in high-amplitude focusing using time reversal. In it the authors are able to define the most effective set of parameters, pre-processing techniques, and spatial placement of elements to maximize the peak pressure of the focus event. My contribution to this work included refining the high-amplitude focusing process, defining the most effective parameters, and increasing the focus levels to look for preliminary evidence of apparent nonlinear growth in the peaks as the output from the generator cards is increased.

A.2 Required Copyright Notice

Citation:

M. L. Willardson, B. E. Anderson, S. M. Young, M. H. Denison, and B. D. Patchett, "Time reversal focusing of high amplitude sound in a reverberation chamber," J. Acoust. Soc. Am. **143**(2), 696-705 (2018).

Time reversal focusing of high amplitude sound in a reverberation chamber

Matthew L. Willardson, Brian E. Anderson,[a] Sarah M. Young, Michael H. Denison, and Brian D. Patchett

Acoustics Research Group, Department of Physics and Astronomy, Brigham Young University, Provo, Utah 84602, USA

(Received 29 September 2017; revised 11 January 2018; accepted 23 January 2018; published online 6 February 2018)

Time reversal (TR) is a signal processing technique that can be used for intentional sound focusing. While it has been studied in room acoustics, the application of TR to produce a high amplitude focus of sound in a room has not yet been explored. The purpose of this study is to create a virtual source of spherical waves with TR that are of sufficient intensity to study nonlinear acoustic propagation. A parameterization study of deconvolution, one-bit, clipping, and decay compensation TR methods is performed to optimize high amplitude focusing and temporal signal focus quality. Of all TR methods studied, clipping is shown to produce the highest amplitude focal signal. An experiment utilizing eight horn loudspeakers in a reverberation chamber is done with the clipping TR method. A peak focal amplitude of 9.05 kPa (173.1 dB peak re 20 μPa) is achieved. Results from this experiment indicate that this high amplitude focusing is a nonlinear process.
 https://doi.org/10.1121/1.5023351

[HCS] Pages: 696–705

I. INTRODUCTION

Time reversal (TR) is a signal processing technique that may be used to achieve intentional sound focusing from remotely placed sources.[1,2] The TR process includes a forward step and a backward step. During the forward step, an impulse response (or transfer function in the frequency domain) is obtained between a source and a receiver. The impulse response is then reversed in time and additional processing may be applied at this stage. During the backward step, the reversed impulse response is broadcast from the source and a focusing of sound is achieved at the receiver location. TR has been used in biomedical applications such as lithotripsy of kidney stones and of brain tumors.[3–5] Researchers optimized the strength and spatial confinement of focused waves in these applications by exploiting the complicated wave propagation in the body. It has also been used in the nondestructive evaluation of solid media, to locate and characterize cracks within a sample.[6–10] Some of the applications of TR to nondestructive evaluation, such as the time reversed elastic nonlinearity diagnostic,[8] are similar to lithotripsy except that instead of destroying tissue with intense sound the focused waves are used to excite nonlinear signatures of cracks. Additionally, TR was used to create a high amplitude focusing of ultrasound for a noncontact source used for nondestructive evaluation.[11,12]

This paper describes the use of TR processing to create a high amplitude focus of sound in a reverberation chamber. The purpose of these experiments is to create a virtual source of spherical waves that are of sufficient intensity to study nonlinear acoustic propagation. TR focuses waves to a selected location that converge from all directions to produce the focus, and then diverge from that location.[13] The divergence of the waves after TR focusing may be considered a virtual source.[14] To achieve the highest possible amplitude of TR focusing several methods are explored here, including deconvolution (or inverse filtering), one-bit, clipping, and decay compensation. The comparison of these methods has not been shown to date.

While the TR process has also been applied to room acoustics applications, the authors are not aware of a similar study that seeks to maximize the amplitude of the focusing of sound in a room. Yon *et al*. compared the performance of beamforming to TR focusing in a highly reverberant room with communications applications in mind.[15] Candy *et al*. compared the performance of TR receivers to an optimal linear equalization receiver in extracting a transmitted signal propagating in a highly reverberant environment, with the purpose of improving communications in reverberant environments.[16] Ribay *et al*. performed a time-domain, finite-difference simulation of TR in a two-dimensional (2-D) reverberation room model, also for communications applications, in order to determine the relationship between the signal-to-noise ratio and the number of physical sources, N, used in TR.[17] They concluded that the focal amplitude depends on N, the length of the impulse response T (in units of time), and the reverberation time of the room. In another study, Candy *et al*. examined the functionality of wideband communications with TR receivers in a tunnel with many obstructions, echoes, and bends.[18]

This paper presents a parameterization study to optimize the TR processing methods mentioned previously for high amplitude focusing and temporal signal focus quality. The parameterization study shows that clipping is the method that produces the highest amplitude focus. A final measurement is then presented in which a TR experiment is

[a]Electronic mail: bea@byu.edu

performed with eight loudspeaker horn sources in a reverberation chamber. A peak focal amplitude of 9.05 kPa (173.1 dB peak re 20 μPa) is achieved. Results from this test indicate that the waves that collapse at these high amplitudes are sufficiently high amplitudes to observe nonlinear wave propagation effects.

II. TIME REVERSAL METHODS

This section will review the basics of the deconvolution (inverse filtering), one-bit, clipping, and decay compensation methods. Each of these methods alters the impulse response/transfer function in order to achieve improved focal amplitude or focal quality. The standard TR process involves a time reversal of the impulse response, $ir(t)$ to obtain the time reversed impulse response (TRIR), $ir(-t)$. In the standard TR process, the TRIR is broadcast from each source simultaneously to produce a focus. It should be noted here that prior to the broadcast of a TRIR or a modified TRIR, this signal is normalized to maximize the available amplification.

A. Deconvolution

Deconvolution or inverse filtering has previously been used in TR experiments to achieve a higher quality focal signal, typically at the expense of the focal amplitude.[19–22] Tanter *et al.* found that inverse filtering reduces the amplitude of the side lobes in a TR experiment.[19] The inverse filter method has also been shown to improve the retrieval of the Green's function between the source and receiver in a TR experiment, leading to a cleaner focus (in a signal-to-noise ratio sense, see Sec. III B) than one obtained via standard TR.[21]

One purpose of the deconvolution method, as outlined by Anderson *et al.*, is to obtain a delta function like focal signal.[22] Thus the desired signal to broadcast during the backward step of the TR process is the frequency domain inverse of the transfer function obtained in the forward step,

$$g(\omega) = \frac{1}{R(\omega)} = \frac{R^*(\omega)}{|R(\omega)|^2}, \tag{1}$$

where $g(\omega)$ is the deconvolution transfer function used to obtain focusing, $R(\omega)$ is the transfer function between the source and receiver, and * denotes a complex conjugate. To avoid potentially dividing by 0 in Eq. (1), a regularization constant is added to the denominator,

$$g(\omega) = \frac{R^*(\omega)}{|R(\omega)|^2 + \gamma\,\mathrm{mean}\left(|R(\omega)|^2\right)}, \tag{2}$$

where γ is a unitless, regularization parameter that can be optimized to produce the cleanest focal signal. Equations (1) and (2) were given by Anderson *et al.* though similar equations were given in Refs. 19–21. Figures 1(a) and 1(b) provide examples of an impulse response used for standard TR and an example of a signal obtained after deconvolution, respectively (the deconvolution method is applied to the standard impulse response shown in this figure with $\gamma = 0.9$). The value of γ is optimized later in this study (Anderson *et al.* used a value of $\gamma = 0.9$).

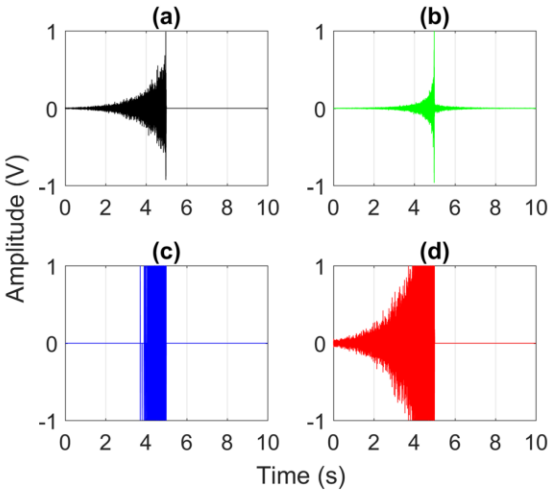

FIG. 1. (Color online) (a) Standard impulse response. (b) Impulse response after deconvolution. (c) Impulse response after one-bit. (d) Impulse response after clipping.

B. One-bit

Derode *et al.* introduced the use of the one-bit method in TR experiments.[23] Their experiments in a water tank achieved an increase of 12 dB in the peak focal amplitude after implementing the one-bit method. The increase in focal amplitude was achieved at the expense of lowering the quality of the time reversal focusing (see Sec. III B).

The one-bit method involves keeping only the phase information of the TRIR signal. For a normalized TRIR, a certain value between 0 and 1 is selected as a threshold and everything above the threshold gets set to $+1$, and everything below the negative value of the threshold gets set to -1. For the purposes of noise rejection, everything in between the positive threshold and the negative threshold is set to 0. The resulting signal for the backward step only contains values of $+1$, 0, and -1. Because the phase information is preserved, the one-bit method still focuses energy. An example one-bit processed signal, with a threshold of 0.2, is shown in Fig. 1(c), with this method applied to the standard impulse response shown in this figure. The threshold value is optimized later in this study.

C. Clipping

Clipping was introduced by Heaton *et al.* as a processing method for TR that is very similar to the one-bit method.[24] Like the one-bit method, clipping of the normalized TRIR signal also involves a threshold value. A value between 0 and 1 is selected as a threshold and everything above the threshold gets set to $+1$, everything below the negative value of the threshold gets set to -1. The difference between the one-bit method and clipping is that for clipping, the signal that lies between the threshold and the negative value of the threshold remains unchanged. An example signal with clipping applied, with a threshold of 0.2, is shown in Fig. 1(d) with the clipping applied to the standard impulse

response shown in this figure. The threshold value is optimized later in this study.

D. Decay compensation

The idea of decay compensation was introduced by Gliozzi *et al.*[25] They sought to compensate for severe attenuation in an impulse response by fitting an exponential decay curve to the impulse response, inverting this decay curve, and then multiplying the square of the inverted decay curve by the impulse response. They argued that this form of decay compensation allowed each reflection arrival in the reversed impulse response to contribute equal amplitude to the TR focus. Each reflected arrival corresponds to an image source and since the energy from each image source must travel the same path that was traveled in the forward step, the same decay rate of energy will occur in the backward step. We will term this form of decay compensation "second order decay compensation" since the inverse of the decay is multiplied by the impulse response twice.

Here we will use what we term "first order decay compensation." Instead of fitting an exponential to the decay in the impulse response, the envelope, $e(t)$, of the normalized TRIR signal is obtained (through a Hilbert transform of the TRIR),

$$e(t) = \sqrt{[ir(-t)]^2 + [\hat{ir}(-t)]^2}, \tag{3}$$

where $\hat{}$ represents a Hilbert transform operator.[26,27] $e(t)$ may be smoothed (for each time sample, the sample and neighboring samples may be averaged). The inverse of the envelope is calculated and multiplied once by the original TRIR signal to obtain the decay compensation signal, $dc(t)$,

$$dc(t) = \frac{1}{e(t)} ir(-t). \tag{4}$$

A threshold value is chosen, such that samples above the threshold (or below the negative value of the threshold) are multiplied by the inverse envelope value while samples below that threshold are unchanged. Figure 2(a) displays $e(t)$ for the $ir(-t)$ given in Fig. 2(a) with a smoothing function. The inverse of $e(t)$ is given in Fig. 2(b). $dc(t)$ is given in Fig. 2(c), with a threshold of 0.05. The threshold value is optimized later in this study.

Thus first order decay compensation multiplies by the inverse decay once while second order decay compensation multiplies by the inverse decay twice. Note that it does not matter whether the inverse decay is multiplied by the forward impulse response or the reversed impulse response so long as the inverse decay information used corresponds to the appropriate forward or backwards direction in time. The focusing in first order decay compensation does not receive equal amplitude contributions from each image source, but the advantage of this technique is that the energy broadcast through the amplifier may be maximized. When one desires to achieve the highest possible focal amplitude then first order decay compensation should be used, since typically the input signals for the backward step are normalized prior to broadcasting them to maximize the available amplifier gain. The use of the envelope of the impulse response also maximizes the available amplification, relative to just using an exponential decay curve, since fluctuations in the impulse response are smoothed out with the envelope approach. In second order decay compensation the late arrivals (which have a lower signal-to-noise ratio) are the highest amplitude portions of the signal broadcast in the backward step, and therefore the earlier reflected arrivals and direct sound are therefore the lower amplitude portions of the signal broadcast in the backward step.

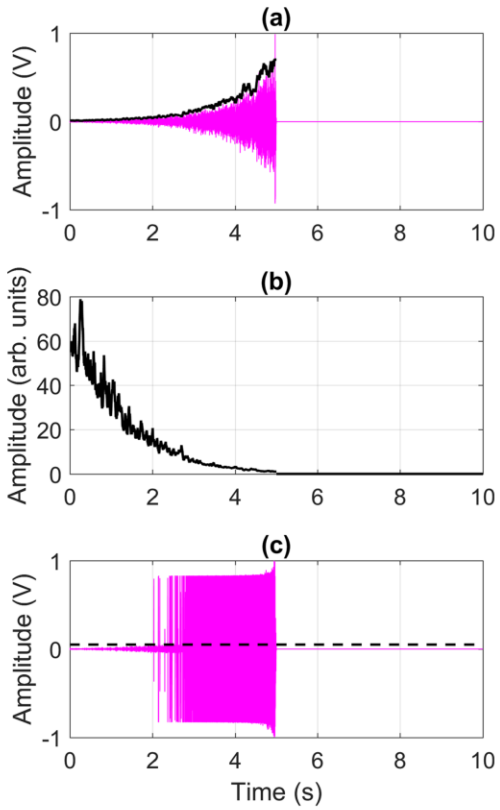

FIG. 2. (Color online) (a) Envelope (black) of the impulse response signal (magenta). (b) Inverse of the envelope in (a). (c) Impulse response after applying decay compensation with the threshold value (dashed black line).

III. FOCAL SIGNAL OPTIMIZATION

This section describes parameterization experiments that are conducted in a reverberation chamber. The TR methods described in Sec. II are each optimized. The length and frequency content of the TRIR are also optimized.

A. Experimental setup

The focal signal optimization tests are performed in a large reverberation chamber (204 m^3) on the Brigham Young University campus. This room is chosen because the hard wall reflections, and therefore long reverberation time,

contribute to a high amplitude focus as shown by Ribay *et al.*[17] The measured reverberation time for the room was found to be 6.89 s and the Schroeder frequency of the room was determined to be 385 Hz.[27] All experiments are performed at frequencies above the Schroeder frequency to ensure a diffuse sound field in the chamber.

The experiments presented in this section employ a single Mackie HR824MK2 loudspeaker as the source and a 1.27 cm (1/2 in.), 46AQ GRAS random incidence microphone with a 53.03 mV/Pa sensitivity as the receiver. A random incidence microphone is chosen for the expected diffuse field in the chamber. Source signals are generated within MATLAB and broadcast from the headphone output on a Dell Latitude E4300 laptop. Data are acquired with a National Instruments PXI-4462 card, housed in a National Instruments 1042 PXI Chassis, with a 204.8 kHz sampling frequency and 24-bit resolution and a LabView program. A photograph of the experimental setup in the room is shown in Fig. 3.

Anderson *et al.* have shown that in rooms, pointing a source directly away from a receiver in a TR experiment yields the highest focal amplitude.[28] Thus the loudspeaker's face is pointed 180° away from the microphone. The loudspeaker's position in the room is 1.54 m from the west wall, 1.85 m from the south wall, and 1.5 m off the ground since room acoustics standards suggest staying at least 1.5 m from any wall to best ensure a diffuse field.[29] Similarly the microphone is placed at least 1.5 m from any wall and is located 1.65 m from the north wall, 1.59 m from the east wall, and 1.61 m off the ground. The distance between the speaker and the microphone is 3.18 m.

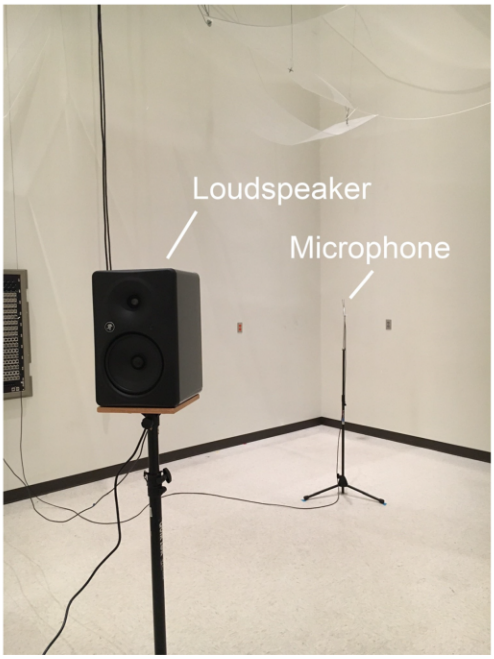

FIG. 3. (Color online) Photograph of the setup used in the optimization experiments in the reverberation chamber.

The source signal, $s(t)$, in the forward step is a logarithmic chirp signal. The pressure response, $r(t)$, is recorded at the microphone. The recording time is set for 10 s to be long enough to exceed the reverberation time. A cross-correlation between $s(t)$ and $r(t)$ is used to estimate the impulse response, $ir(t)$.[28] Depending on the particular experiment, additional processing to implement deconvolution, one-bit, etc. is then applied at this stage to the normalized $ir(t)$. The TRIR was then broadcast from the loudspeaker to produce a focus at the microphone location.

B. Optimization metrics

The peak amplitude and temporal quality are two metrics used here to characterize the focal signal. Peak amplitude, A_P, is a measure of the maximum pressure magnitude (in Pa) achieved in the focal signal. Temporal quality, defined by Heaton *et al.*, compares the squared peak focal amplitude to the average squared pressure present in the signal.[24] Because these experiments involve discrete time signals, the following adapted equation is used to calculate the temporal quality,

$$\xi_T = \sqrt{\frac{[A_P]^2}{\frac{T}{M}\sum_{m=0}^{M}\left[A(x_0, y_0, z_0, m)\right]^2}}, \tag{5}$$

where M is the length of the signal in samples, and $A(x_0, y_0, z_0, m)$ is the amplitude of the mth sample at the microphone focal position (x_0, y_0, z_0). ξ_T is a unitless metric that, with the square root, effectively gives a ratio of peak amplitude to the average pressure magnitude throughout the signal. A delta function signal would have $\xi_T = \sqrt{M}$, a sine wave signal would have $\xi_T = \sqrt{2}$, and a random noise signal would have $\xi_T = \sqrt{3}$.

C. Results of optimization experiments

A total of six sets of optimization experiments are conducted to optimize the TRIR processing: source bandwidth, impulse response length, deconvolution, one-bit, clipping, and decay compensation.

The source bandwidth is varied to determine the bandwidth of the chirp signal that will maximize A_P for standard TR. Thirty-three different bandwidths are tested ranging from 500 Hz to 16 kHz. Frequencies below 500 Hz are not examined due to the Schroeder frequency limit of 385 Hz. The reverberation time in rooms is typically smaller for high frequencies than for low frequencies, thus higher frequency content may not contribute much to TR focusing. The only variable changed in this experiment is the bandwidth of the initial chirp signal, $s(t)$. The first experiment is done over a bandwidth of 7–8 kHz, and the subsequent experiments include more frequency content until a bandwidth of 500 Hz to 16 kHz is reached. The experiments show that adding higher frequency content generally improves ξ_T of the focal signal, while adding lower frequency content degrades ξ_T. However, it is also found that adding lower frequency content does more to boost A_P of the resulting focal signal. This

is likely partly due to the fact that at higher frequencies the absorption is higher and therefore the reverberation would be less significant resulting in lower amplitude image sources in the backward step. The band from 500 to 9500 Hz produced the highest A_P of 17.2 Pa and a ξ_T of 93.3. The rest of the sets of optimization experiments are performed with the optimal 500–9500 Hz band.

The length of the impulse response using standard TR is varied to determine the minimum length of the impulse response needed before A_P is maximized. A nearly 5 s long TRIR is obtained and prior to the broadcast of the TRIR from the loudspeaker, the length of the TRIR was changed. A total of 7 different TRIR lengths were tested, ranging from 0.5 s to the full TRIR length of 4.97 s. The results in Fig. 4 show that shortest length to achieve maximal A_P is around 2.0 s. The minimum length needed in a given room likely depends on the reverberation time in that room. These results confirm those found by Ribay *et al.*, that the length of the impulse response affects A_P.[17]

The experiments optimizing deconvolution are done by obtaining a TRIR and then changing the γ parameter in the deconvolution processing [see Eq. (2)] before broadcasting the modified TRIR from the loudspeaker. One-hundred, logarithmically spaced γ values are tested, ranging from 10^{-6} to 10^{3}. The modified TRIR signal is then broadcast from the loudspeaker and a focal signal is recorded at the microphone for each of the 100 γ values. The results of the deconvolution experiments are shown in Fig. 5. As γ approaches infinity, the deconvolution processing becomes equivalent to standard TR since the magnitude squared term in the denominator of Eq. (2) is small compared to the very large γ term. The modified TRIR is then normalized and Eq. (2) becomes just a standard TRIR. A γ value of zero results in an amplification of noise and therefore a low ξ_T. As described earlier in this section in the literature, deconvolution produces signals with higher ξ_T (ξ_T is related to the signal-to-noise ratio used in the literature) at the expense of a reduction in A_P.

Since the purpose of using deconvolution is to produce focal signals with higher ξ_T, and no value of γ results in a higher A_P than using standard TR, the optimum γ value of 0.1 is selected. This value differs from the γ value of 0.9

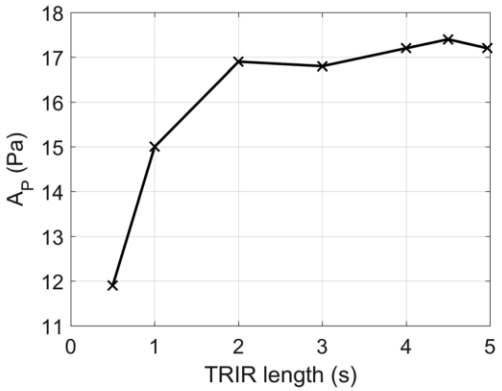

FIG. 4. Peak focal amplitude of a standard time reversal experiment as a function of the length of the impulse response used.

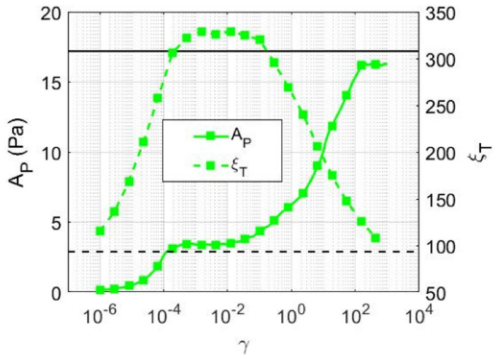

FIG. 5. (Color online) Results of the optimization of deconvolution processing. The focal amplitude, A_P, (solid line) and the temporal quality, ξ_T, (dashed line) are each plotted as a function of the regularization parameter, γ. The solid black line represents the A_P for standard TR, and the dashed black line represents the ξ_T for standard TR.

given by Anderson *et al.*[22] The optimal value for γ may well depend on the available signal-to-noise ratio in the system. Gamma values below 0.1 do not produce focal signals with significantly higher ξ_T, and ξ_T begins to decrease with γ values larger than 0.1. Smaller γ values could be used at the expense of further reductions in A_P. A γ value of 0.1 produced a focal signal with $A_P = 4.4$ Pa and $\xi_T = 320$. Compared to standard TR, the optimal deconvolution focal signal has a ξ_T that is 3.43 times greater, but a A_P that is 3.91 times lower. For the purposes of maximizing A_P, the significant amplitude reduction does not make deconvolution the optimal technique for producing a high amplitude focus.

In the optimization of the one-bit, clipping, and decay compensation signal processing methods, the threshold value is the parameter modified to find the optimum value for high amplitude focusing. Section II described the manner in which the threshold is applied for these methods. For each of these experiments, a TRIR signal is obtained, processed according to the method employed, and then broadcast from the loudspeaker to achieve a focus at the microphone. One-hundred, logarithmically spaced threshold values are tested for each processing method, ranging from 10^{-5} to 1.

The results of the one-bit, clipping, and decay compensation sets of experiments are shown in Figs. 6 and 7. Figure 6 compares A_P for the three methods, and Fig. 7 compares ξ_T for the three methods. These results show that decreasing the threshold value generally creates focal signals with a higher A_P for all three types of signal processing. Also, the increase in A_P is gained generally at the expense of decreasing ξ_T.

Of the three processing methods, clipping produces the highest A_P. This makes sense since more energy is broadcast when clipping is used because the low amplitude samples are not zeroed out as they are in one-bit processing. The optimum clipping threshold value of 0.03 produces a focal signal with $A_P = 110.8$ Pa. This means that with the optimum clipping threshold, the A_P of a standard TR focal signal of 17.2 Pa can be amplified by a factor of 6.44. In terms of dB, clipping processing produces a gain of 16.2 dB. There is a

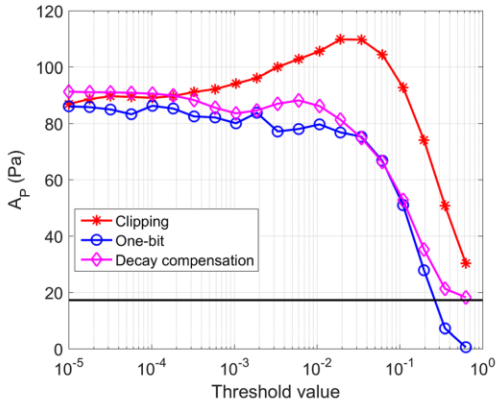

FIG. 6. (Color online) Comparison of the peak focal amplitude, A_P, of the clipping, one-bit, and decay compensation methods over 100 threshold values. The solid black line represents the A_P for standard TR.

decrease in ξ_T, from 93.3 with standard TR down to 72.9 with clipping processing, a 21.9% reduction. The drop in ξ_T is offset by the significant gain in A_P.

The decay compensation method performs better than the one-bit method both in terms of A_P and ξ_T across nearly every threshold value. The optimum threshold value for decay compensation is found to be 0.005. This optimum threshold for decay compensation produced a focal signal with $A_P = 88.5$ Pa and $\xi_T = 61.9$. The A_P of 88.5 Pa is 5.15 times greater than the A_P for standard TR, but it is accompanied with a 33.7% reduction in ξ_T. The optimum threshold value for the one-bit method is found to be 0.02. This optimum threshold for the one-bit method produced a focal signal with $A_P = 78.7$ Pa and $\xi_T = 63.5$. The A_P of the optimal one-bit focal signal is 4.58 times greater than the A_P for standard TR, but ξ_T is 31.9% less than ξ_T achieved with standard TR.

Though not presented here in detail, the clipping, one-bit, and decay compensation methods are applied to the deconvolution modified TRIR signals. The results indicate that both ξ_T (inherited from the deconvolution) and A_P (inherited from the clipping, one-bit, and decay compensation) of the focusing improve compared to standard TR. For clipping with deconvolution, the optimum threshold value is 0.01, slightly lower than the optimum threshold of 0.03 for clipping with standard TR. The optimum threshold for clipping with deconvolution produces a focal signal with $A_P = 43.5$ Pa and $\xi_T = 162.2$. Compared to standard TR, A_P increases by a factor of 2.5 and ξ_T increases by a factor of 1.7. This increase in both A_P and ξ_T shows the robustness of combining deconvolution with clipping techniques to achieve better focusing than standard TR. However the reduction in A_P, relative to when deconvolution is not used, is a drawback to using deconvolution and clipping, for example, to achieve the highest possible focusing amplitude.

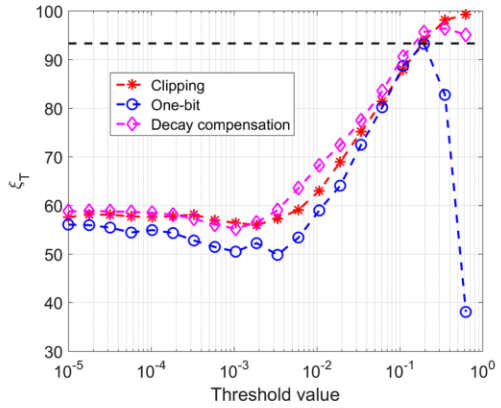

FIG. 7. (Color online) Comparison of the temporal quality, ξ_T, of the clipping, one-bit, and decay compensation methods over 100 threshold values. The dashed black line represents the ξ_T for standard TR.

Before the high amplitude experiments are conducted, a seventh optimization experiment is done to determine the best placement of the sources to achieve the highest possible amplitude for TR focusing. Experiments are conducted with a microphone in the same location as it was in the other optimization experiments (on a stand, 1.61 m off the ground). The loudspeaker is moved to different locations in the room, and a standard TR experiment is done at each location to determine optimum speaker placement for the highest amplitude focus. The results show that the highest amplitude is achieved when the speaker and the microphone are in the same horizontal plane (the primary axis of the loudspeaker is directed in the plane of the microphone), and when the loudspeaker and microphone are placed in corners of the room. These gains due to source and receiver placement in the room are on the order of up to 6 dB gains and likely result from a significant change to the radiation impedance loading (specifically an increase in the radiation resistance) seen by the compression driver horns. When the horns are placed facing the wall they radiate into a smaller open area between the horn opening and the wall as compared to the case when the horn is facing the center of the room.

IV. HIGH AMPLITUDE FOCUSING

Building off the results of Sec. III, a new set of experiments are designed to achieve a high focal amplitude by using the optimal processing of the TRIR, more efficient sound sources, and larger N. The high amplitude focusing measurements are performed in the same reverberation chamber as the optimization experiments. The setup consists of eight BMS 4590 coaxial compression drivers with horns attached to the drivers. One 0.3175 cm (1/8 in.) 40DP GRAS free-field microphone with a 26AC GRAS preamplifier is used for these measurements. Random incidence microphones were unavailable for this size microphone. The microphone has a sensitivity of 0.76 mV/Pa. The microphone has a specified dynamic range upper limit of 175 dB (178 dB peak or 15.9 kPa) for a ± 1 dB precision. A 12AA GRAS microphone power supply is used to power the microphone. The signals presented in this section are the result of using 10 averages.

The signals used for these experiments are created in MATLAB and output via two, 4-channel Spectrum M2i.6022-exp generator cards. The acquisition is done with one, 4-

channel Spectrum M2i.4931-exp digitizer card. A sampling frequency of 50 kHz is used and the digitizer has 16 bit precision. The output from the Spectrum cards is amplified with two, 4-channel Crown CT4150 amplifiers. The eight amplified signals are routed through patch panels via Speakon cables into the reverberation chamber and then to the horn drivers. A panoramic photograph of the setup for the high amplitude focusing experiments is shown in Fig. 8.

Based on the results of the optimization experiments, the drivers are placed close to the corners of the room or close to the adjoining boundary of a wall and the floor. The orientation of each driver is facing nearly 180° away from the microphone. The microphone is placed 3 cm away from a corner in the room in order to achieve the highest possible A_P.

Due to constraints on the upper frequency limit of the mid-range coaxial compression driver, the bandwidth of the initial chirp signal is 500–7500 Hz. This is not a significant issue in terms of amplitude reduction however, because in the earlier optimization experiments the difference in A_P is minimal between the optimal bandwidth of 500–9500 Hz and the bandwidth of 500–7500 Hz. The Crown amplifiers are set to zero attenuation and the output voltage on the Spectrum M2i.6022-exp generator cards is set to 0.6 V peak. The amplifiers provide a 27 dB gain creating an output voltage signal of 8.78 V peak with a 0.392 V peak input signal, which should draw 9.63 W of power in a nominal 8 Ω load. The horns are rated for 150 W of continuous power, thus the amplifier and horns were used well within their linear operating ranges. The clipping TR processing was used throughout this section to create the highest focal amplitude possible within the linear range of the microphone.

In order to observe whether the TR focusing at these amplitudes is a linear or a nonlinear process, four experiments are performed with the clipping method, each with a different input voltage. The input voltages are 0.049 V (Level 1), 0.098 V (Level 2), 0.196 V (Level 3), and 0.392 V (Level 4). Note that each level increase in voltage represents an increase by a factor of 2. For each case the input attenuation knobs are fixed at 0 dB attenuation. If the focusing is a linear process then the lower amplitude focal signals should be identical to the highest amplitude focal signal when scaled up linearly, aside from background noise. The four focal signals obtained with each input voltage level are shown in Fig. 9(a). One can observe the impulsive focusing at the 10.4856 s mark. Figure 9(b) shows the same data with a different time interval to see the amplitudes around the time of peak focusing. The peak compression (positive peak) magnitudes are 0.951, 1.96, 4.10, and 9.05 kPa, respectively, or 153.5, 159.8, 166.2, and 173.1 dB peak, respectively. Note that the differences between successive levels are 6.1, 6.3, 6.4, and 6.9 dB, when a 6.0 dB, representing a pressure doubling, would be expected for a linear system. Thus all recorded amplitudes are within the microphone's specified ±1 dB range.

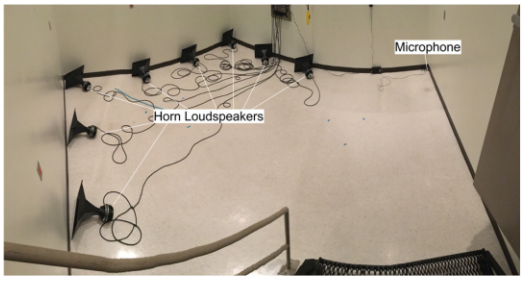

FIG. 8. (Color online) Panoramic photograph of the high amplitude focusing experimental setup in the reverberation chamber.

Linearly scaled versions of these focal signals are shown in Fig. 9(c). Linear scaling is done by multiplying each focal signal by the highest input voltage level, $A_4 = 0.392$ V, and dividing by the corresponding ith input voltage level, $A_i, = 0.049$, 0.098, 0.196, and 0.392 V such that if the focusing were a linear process, all focal signals would match the highest voltage level focal signal. The linearly scaled peak compression magnitudes are 7.61, 7.82, 8.20, and 9.05 kPa, respectively. If the scaled, Level 1 peak compression magnitude is assumed as a reference scaled magnitude then the scaled magnitudes of the compression peaks of the four different focal signals are 1.00, 1.03, 1.08, and 1.19 times the reference scaled magnitude, respectively, meaning that the Level 4 peak magnitude is 19% more the magnitude it should be if it scales linearly. Interestingly, on either side of the peak compression one can observe that the rarefactions nonlinearly decrease in magnitude. This nonlinear increase in the magnitude of the peak compression as the input voltage is increased and the nonlinear decrease in the magnitude of the rarefactions (negative peaks) on either side of the peak compression requires further study. Figure 9(d) shows a segment of the scaled focal signals displayed in Fig. 9(c) at a time before the focal time. This figure shows that the signals scale linearly at these lower amplitudes before the maximal focusing occurs. In fact, all of the focal signals linearly scale before the time of focus, but linear scaling does not hold when the amplitudes rise significantly near the time of focus [the time window shown in Fig. 9(c)] nor does linear scaling hold after the time of focus. A more in depth study of the spatial dependence of this focusing of high amplitude waves is planned for future work. However, because the instantaneous amplitudes of the scaled focal signals linearly scale before the time of focusing, one would expect linear scaling elsewhere in the room before the time of focusing since the energy that arrives at the focal location before the focal time had traveled elsewhere in the room before it arrived there. Therefore it is logical to assume that linear scaling would exist everywhere else in the room before the time of focusing as long as the amplitudes are low in other room locations.

While a more complete study of these nonlinear effects is beyond the scope of this paper, it is interesting to observe changes in the frequency spectra of the focal signals. Figure 10(a) shows scaled sound pressure level spectra for the entire focal signals. These spectra have been smoothed with a 20 ms sliding window to more easily observe changes in the spectra. Only frequency content between 400 Hz and 2 kHz are shown since the majority of the amplitude in these spectra are contained within this band. Note that the Level 1 background noise is approximately at a level of 53 dB. This noise level is highest in the Level 1 spectrum because of the

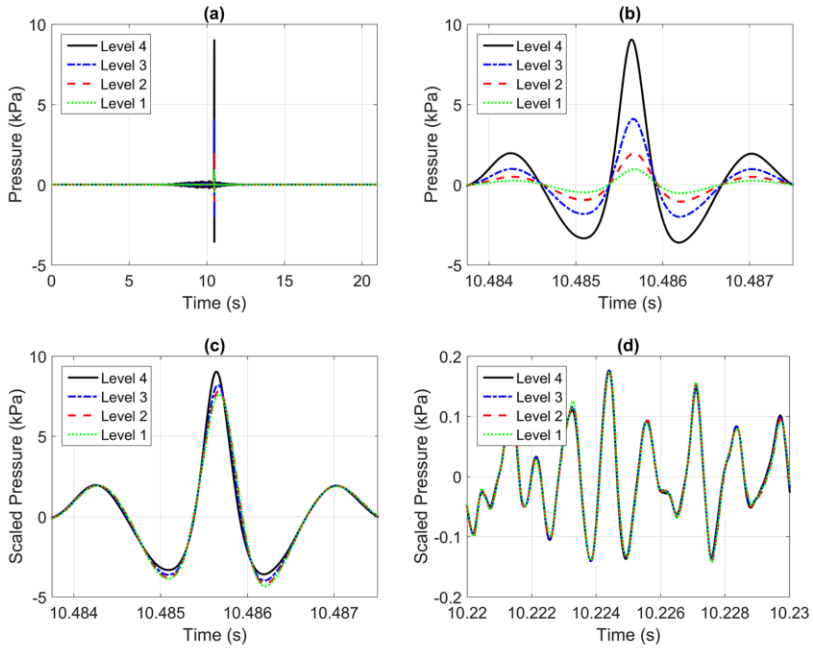

FIG. 9. (Color online) Focal signals obtained from the clipping TR method at high amplitudes. (a) Unscaled focal signals for Levels 1–4. (b) Zoomed in version of (a). (c) Scaled focal signals for Levels 1–4 at a zoomed in time scale. (d) Scaled segment of the focal signals away from the time of peak focusing for Levels 1–4.

linear scaling of the focal signals. In order to more easily see the changes in the spectra with increased input amplitude, the scaled spectra are compared to the Level 1 spectrum by subtracting the Level 1 spectrum from a given scaled spectrum, similar to the procedure proposed by Scalerandi *et al.*[30] These spectral differences are shown in Fig. 10(b). One can observe the decrease in the spectral amplitudes with increased input amplitude between 530 and 1065 Hz by as much as 0.4 dB when comparing the Level 4 spectrum to the Level 1 spectrum. Between 1065 and 2000 Hz there is a noted increase in spectral amplitudes by as much as 7.4 dB when comparing the Level 4 spectrum to the Level 1 spectrum. Note that below 500 Hz it is expected that the signal would drop off because that was the starting frequency of the original chirp signal. The scaled and subtracted spectra should not be reliable below 500 Hz. The low frequency

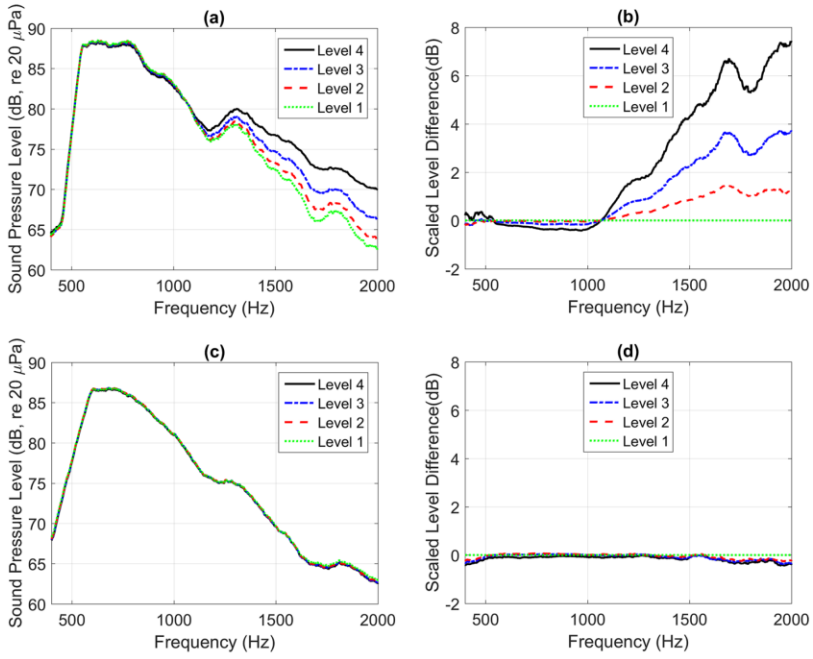

FIG. 10. (Color online) Focal signal spectra obtained from the clipping TR method at high amplitudes. (a) Scaled, focal signal spectra for Levels 1–4 (spectra obtained using the full focal signals). (b) Results of a subtraction of the scaled spectra from Levels 1–4 minus the scaled spectrum of Level 1. (c) Shortened, scaled, focal signal spectra for Levels 1–4 (spectra obtained using the only the portions of the focal signals before the focal time). (d) Results of a subtraction of the shortened, scaled spectra from Levels 1–4 minus the shortened, scaled spectrum of Level 1.

(500–1065 Hz) amplitudes in the higher input amplitude spectra are decreased while the high frequency (1065–2000 Hz) amplitudes in the higher input amplitude spectra are increased. If we now only consider the portion of each focal signal before the focal times, from time zero up until 10.4 s, we can plot their scaled spectra in Fig. 10(c). As before we can then use the Level 1 spectrum as a reference and subtract each spectrum from the Level 1 reference spectrum to obtain Fig. 10(d). Note that the spectra displayed in Fig. 10(c) appear to be identical and indeed in Fig. 10(d), we find a maximum deviation of 0.4 dB between the Level 4 spectrum and the Level 1 spectrum at 2000 Hz where the background noise is likely to blame for the differences in scaled spectra. This shows that linear scaling of the focal signals occurs before the time of focus, but when the amplitudes increase at the time of focus then linear scaling no longer is observed.

To put the focal amplitudes we observe in context of the shock formation distance, we assume a nonlinearity parameter of $\beta = 1.2$. For a peak pressure amplitude of 9 kPa, we obtain an acoustic Mach number of $M = 0.06$. Using the lowest frequency, 500 Hz, for our study we obtain an acoustic wave number of $k = 9\,\mathrm{m}^{-1}$ and using the highest frequency, 2000 Hz, for our study we obtain $k = 37\,\mathrm{m}^{-1}$. The plane wave shock formation distance is known to be $\bar{x} = 1/(\beta M k)$, or in relative terms, $\bar{x}/\lambda = 1/(2\pi\beta M)$. If we assume these expressions are applicable to our results, since a shock formation distance for spherical waves is not well established in the literature, $\bar{x}(500\,\mathrm{Hz}) = 1.4\,\mathrm{m}$, $\bar{x}(2000\,\mathrm{Hz}) = 0.38\,\mathrm{m}$, and $\bar{x}/\lambda = 0.47$. This relative shock formation distance calculation suggests that nonlinear wave steepening effects are expected, despite the limitations of our use of the plane wave shock formation distance. One would not expect that shock waves would be well established for our results. It should be noted that the Mach number used in this analysis is valid at the focus location and thus one would expect a longer shock formation distance as a result since the converging waves are of less amplitude than 9 kPa.

A similar analysis of the results of Montaldo *et al.*[31] would suggest $\bar{x}/\lambda = 24$. Shock waves appear to be well established in their focal signal. For their low amplitude result, an input of 0.25 V was used and a peak focal amplitude of about 0.85 bar was observed. For their high amplitude result, an input amplitude of 17 V was used and a peak focal amplitude of about 45 bar was observed. Linear scaling of the 0.85 bar result would suggest an amplitude of 58 bar. Thus Montaldo *et al.* observed a decrease in the focal amplitude, relative to linear scaling, rather than an increase as we observe in our reverberation chamber results. However, the well formed shocks in the results of Montaldo *et al.* suggest that significant attenuation of the focal amplitude may have happened due to losses at the shocks. Our results did show a tendency to steepen the leading edge of compression peaks and a broadening of rarefaction peaks as was observed to a greater extent by Montaldo *et al.*[31] and by Ganjehi *et al.*[32]

In Provo, Utah the elevation is 1387 m (4551 feet) and the measured temperature on the day of the measurements presented in this section is 21.1 °C. Notably, the measured atmospheric pressure is 85.7 kPa instead of the standard value of 101.3 kPa given at sea level. Thus the peak acoustic compression pressure value of 9.05 kPa above atmospheric pressure is 1.11 times atmospheric pressure in Provo (94.7 atm).

V. CONCLUSION

A parameterization study has been presented, seeking to optimize the peak amplitude, A_P, of TR focusing and the temporal quality, ξ_T, of the TR focal signals for deconvolution, one-bit, clipping, and decay compensation TR methods. First order decay compensation is a variant of a previously proposed method that seeks to amplify later arrivals in an impulse response signal in order to maximize the energy broadcast in the backward step. First order decay compensation performed better than the one-bit method both in terms of focal amplitude, A_P, and temporal quality, ξ_T. The optimal regularization parameter, γ, value was found for the deconvolution method, and optimal threshold values were found for the clipping, one-bit, and decay compensation methods. It has been shown that the clipping method is the impulse response modification method that produces the highest amplitude focus of sound in a reverberation chamber.

With eight horn loudspeaker sources in a reverberation chamber and the optimal clipping threshold, $A_P = 9.05$ kPa (173.1 dB peak) was achieved. Experiments conducted at lower amplitudes and scaled appropriately to the highest amplitude result provide evidence that TR focusing at these high amplitudes is a nonlinear process. Compression magnitudes are nonlinearly increased with higher focusing amplitudes whereas rarefaction magnitudes are nonlinearly decreased with higher focusing amplitudes. A decrease in low frequency energy and an increase in high frequency energy in the spectra of the linearly scaled focal signals, along with linear scaling observed before the time of focusing, suggests that the observed distortions are due to amplitude-dependent wave steepening effects. These experiments will be studied in more detail in future work, including spatial scanning of the focus and creating a louder focus with a microphone that can accurately record higher levels. A theoretical model of nonlinear wave propagation for spherically converging waves of high amplitude might be able to help illustrate and predict these nonlinear effects observed as high amplitude waves collapse to provide a time reversal focus.

ACKNOWLEDGMENTS

This work was made possible through the resources provided by the BYU Department of Physics and Astronomy. The authors want to thank Brent Reichman and Kent Gee for their assistance.

[1]M. Fink, "Time reversed acoustics," Phys. Today **50**(3), 34–40 (1997).
[2]B. E. Anderson, M. Griffa, C. Larmat, T. J. Ulrich, and P. A. Johnson, "Time reversal," Acoust. Today **4**(1), 5–16 (2008).
[3]J.-L. Thomas, F. Wu, and M. Fink, "Time reversal mirror applied to litotripsy," Ultrason. Imaging **18**, 106–121 (1996).

[4]J.-L. Thomas and M. Fink, "Ultrasonic beam focusing through tissue inhomogeneities with a time reversal mirror: Application to transskull therapy," IEEE Trans. Ultrason. Ferroelectr. Freq. Control **43**(6), 1122–1129 (1996).
[5]M. Tanter, J.-L. Thomas, and M. Fink, "Focusing and steering through absorbing and aberating layers: Application to ultrasonic propagation through the skull," J. Acoust. Soc. Am. **103**(5), 2403–2410 (1998).
[6]C. Prada, E. Kerbrat, D. Cassereau, and M. Fink, "Time reversal techniques in ultrasonic nondestructive testing of scattering media," Inverse Probl. **18**, 1761–1773 (2002).
[7]E. Kerbrat, C. Prada, D. Cassereau, and M. Fink, "Ultrasonic nondestructive testing of scattering media using the decomposition of the time reversal operator," IEEE Trans. Ultrason. Ferroelectr. Freq. Control **49**, 1103–1113 (2002).
[8]T. J. Ulrich, P. A. Johnson, and A. Sutin, "Imaging nonlinear scatterers applying the time reversal mirror," J. Acoust. Soc. Am. **119**(3), 1514–1518 (2006).
[9]B. E. Anderson, M. Griffa, T. J. Ulrich, P.-Y. Le Bas, R. A. Guyer, and P. A. Johnson, "Crack localization and characterization in solid media using time reversal techniques," in *44th U. S. Rock Mechanics Symposium and 5th U. S.–Canada Rock Mechanics Symposium*, 27–30 June 2010, Salt Lake City, Utah, document no. 10-154.
[10]B. E. Anderson, L. Pieczonka, M. C. Remillieux, T. J. Ulrich, and P.-Y. Le Bas, "Stress corrosion crack depth investigation using the time reversed elastic nonlinearity diagnostic," J. Acoust. Soc. Am. **141**(1), EL76–EL81 (2017).
[11]P.-Y. Le Bas, T. J. Ulrich, B. E. Anderson, and J. J. Esplin, "A high amplitude, time reversal acoustic non-contact excitation (TRANCE)," J. Acoust. Soc. Am. **134**(1), EL52–EL56 (2013).
[12]P.-Y. Le Bas, M. C. Remillieux, L. Pieczonka, J. A. Ten Cate, B. E. Anderson, and T. J. Ulrich, "Damage imaging in a laminated composite plate using an air-coupled time reversal mirror," Appl. Phys. Lett. **107**, 184102 (2015).
[13]B. E. Anderson, T. J. Ulrich, and P.-Y. Le Bas, "Comparison and visualization of the focusing wave fields of various time reversal techniques in elastic media," J. Acoust. Soc. Am. **134**(6), EL527–EL533 (2013).
[14]M. Scalerandi, A. S. Gliozzi, B. E. Anderson, M. Griffa, P. A. Johnson, and T. J. Ulrich, "Selective source reduction to identify masked sources using time reversal acoustics," J. Phys. D Appl. Phys. **41**, 155504 (2008).
[15]S. Yon, M. Tanter, and M. Fink, "Sound focusing in rooms: The time-reversal approach," J. Acoust. Soc. Am. **113**(3), 1533–1543 (2003).
[16]J. V. Candy, A. W. Meyer, A. J. Poggio, and B. L. Guidry, "Time-reversal processing for an acoustic communications experiment in a highly reverberant environment," J. Acoust. Soc. Am. **115**(4), 1621–1631 (2004).
[17]G. Ribay, J. de Rosny, and M. Fink, "Time reversal of noise sources in a reverberation room," J. Acoust. Soc. Am. **117**(5), 2866–2872 (2005).
[18]J. V. Candy, D. H. Chambers, C. L. Robbins, B. L. Guidry, A. J. Poggio, F. Dowla, and C. A. Hertzog, "Wideband multichannel time-reversal processing for acoustic communications in a tunnel-like structure," J. Acoust. Soc. Am. **120**(2), 838–851 (2006).
[19]M. Tanter, J.-L. Thomas, and M. Fink, "Time reversal and the inverse filter," J. Acoust. Soc. Am. **108**(1), 223–234 (2000).
[20]M. Tanter, J.-F. Aubry, J. Gerber, J.-L. Thomas, and M. Fink, "Optimal focusing by spatio-temporal filter. I. Basic principles," J. Acoust. Soc. Am. **110**(1), 37–47 (2001).
[21]T. Gallot, S. Catheline, P. Roux, and M. Campillo, "A passive inverse filter for Green's function retrieval," J. Acoust. Soc. Am. **131**(1), EL21–EL27 (2012).
[22]B. E. Anderson, J. Douma, T. J. Ulrich, and R. Snieder, "Improving spatio-temporal focusing and source reconstruction through deconvolution," Wave Motion **52**(9), 151–159 (2015).
[23]A. Derode, A. Tourin, and M. Fink, "Ultrasonic pulse compression with one-bit time reversal through multiple scattering," J. Appl. Phys. **85**(9), 6343–6352 (1999).
[24]C. Heaton, B. E. Anderson, and S. M. Young, "Time reversal focusing of elastic waves in plates for an educational demonstration," J. Acoust. Soc. Am. **141**(2), 1084–1092 (2017).
[25]A. S. Gliozzi, M. Scalerandi, and P. Antonaci, "One-channel time-reversal acoustics in highly attenuating media," J. Phys. D: Appl. Phys. **46**, 135502 (2013).
[26]J. Vanderkooy and S. P. Lipschitz, "Uses and abuses of the energy-time curve," J. Audio Eng. Soc. **38**(11), 819–836 (1990), available at http://www.aes.org/e-lib/browse.cfm?elib=6007.
[27]J. J. Esplin, B. E. Anderson, T. W. Leishman, and B. T. Thornock, "The effects of non-cardioid directivity on incidence estimation using the polar energy time curve," J. Acoust. Soc. Am. **130**(4), EL244–EL250 (2011).
[28]B. E. Anderson, M. Clemens, and M. L. Willardson, "The effect of transducer directionality on time reversal focusing," J. Acoust. Soc. Am. **142**(1), EL95–EL101 (2017).
[29]ISO 3741:2010, "Acoustics-Determination of sound power and sound energy levels of noise sources using sound pressure—Precision methods for reverberation test rooms" (International Organization for Standardization, Geneva, Switzerland, 2010).
[30]M. Scalerandi, A. S. Gliozzi, C. L. E. Bruno, D. Masera, and P. Bocca, "A scaling method to enhance detection of a nonlinear elastic response," Appl. Phys. Lett. **92**(10) 101912 (2008).
[31]G. Montaldo, P. Roux, A. Derode, C. Negreira, and M. Fink, "Ultrasound shock wave generator with one-bit time reversal in a dispersive medium, application to lithotripsy," Appl. Phys. Lett. **80**(5), 897–899 (2002).
[32]L. Ganjehi, R. Marchiano, F. Coulourat, and J.-L. Thomas, "Evidence of wave front folding of sonic booms by a laboratory-scale deterministic experiment of shock waves in a heterogeneous medium," J. Acoust. Soc. Am. **124**(1), 57–71 (2008).

Appendix B

B.1 Introduction

The following article, in which I am a co-author, represents a significant amount of experimental work done by me in order to verify claims that time reversal was successful at reducing MRI noise for patients receiving a scan. My work helped to define the process, and to find the most effective methods of time reversal focusing for application to active noise control.

B.2 Required Copyright Notice

Citation:
T. S. Furlong, B. E. Anderson, B. D. Patchett, S. D. Sommerfeldt, “Active noise control using remotely placed sources: Application to magnetic resonance imaging noise and equivalence to the time reversal inverse filter,” Appl. Acoust. **176**, 107902 (2020).

Applied Acoustics 176 (2021) 107902

Contents lists available at ScienceDirect

Applied Acoustics

journal homepage: www.elsevier.com/locate/apacoust

Active noise control using remotely placed sources: Application to magnetic resonance imaging noise and equivalence to the time reversal inverse filter

Trent S. Furlong, Brian E. Anderson *, Brian D. Patchett, Scott D. Sommerfeldt

Acoustics Research Group, Department of Physics and Astronomy, Brigham Young University, N283 Eyring Science Center, Provo, UT 84602, United States

ARTICLE INFO

Article history:
Received 24 March 2020
Received in revised form 15 December 2020
Accepted 23 December 2020

Keywords:
Time reversed
Magnetic resonance imaging
Active noise control
Active control
Time reversal

ABSTRACT

This paper explores the feasibility of active control of noise from magnetic resonance imaging (MRI) systems using control sources placed outside of the region that MRI scanners are sensitive to ferrous materials. Active noise control (ANC) is shown here to be equivalent to the time reversal (TR) inverse filter technique with a 180° phase shift. Since TR is capable of remotely focusing sound energy to a point in space, it follows that ANC may also be remotely focused. This paper explores the remote delivery of a noise-canceling signal to a desired location (e.g. a patient's ears). A parameterization study testing frequency dependence and signal length is conducted to determine the effectiveness of the remote delivery. The reduction of MRI noise using ANC is demonstrated using recordings of MRI noise. The parameterization and MRI noise reduction studies are conducted in a reverberation chamber and in a laboratory room with a lower reverberation time. Frequencies below 1 kHz and narrowband signals are easier to control, with reductions up to 20 dB. MRI noise is reduced by up to 18 dB in overall sound pressure level. These results utilized a single control loudspeaker; further reductions should be possible with multiple control sources.

1. Introduction

Noise from magnetic resonance imaging (MRI) equipment puts patients at risk for hearing damage [1]. Lee *et al.* measured sound pressure levels up to 130 dB from a 3 Tesla MRI [1]. Active noise control (ANC) systems have been implemented to reduce the noise patients perceive by using non-ferromagnetic equipment next to the patient's ears, inside the bore [1–3]. These studies cancelled sound at the patient's ears without requiring the patient to wear headphones. Additionally, conducting MRI scans on patients who are hyper sensitive to noise, such as those with Autism Spectrum Disorder (ASD), can present a major challenge. The noisy scanning environment makes functional magnetic resonance imaging (fMRI) studies of auditory processing in ASD very difficult [4] and is a key confound for interpretation of ongoing studies of the neural mechanisms of anxiety in ASD [4–5]. MRI compliant noise cancelling headphones have also been developed and produced commercially [6]. High-fidelity dynamic loudspeakers would be ideal to use for ANC, however not only do the magnetic fields from dynamic loudspeakers pose a problem, but stray eddy currents generated in conductors as a result of Lenz's law also can corrupt the imaging [7–8]. The small bore of the MRI machine also limits the size of ANC systems, further restricting usable equipment. Other issues for ANC systems applied to MRI noise include, but are not limited to, the fundamental frequency produced by a scanning sequence, the speed of a scan, and noise conduction through the body [3,9].

ANC systems reduce noise by broadcasting a signal that, upon propagation to a desired control location, creates an equal amplitude and opposite-phase sound at the desired control location to attenuate the expected noise at the desired control location when these sounds are superposed. A typical ANC system is comprised of a reference sensor, a control source (loudspeaker) to broadcast a noise-canceling (or "control") signal, and an error sensor. The noise signal detected by the reference sensor is passed through a filter that creates the control signal. The control signal is then broadcast through the loudspeaker and the two sounds cancel each other out by linear superposition at the error microphone. Ideally the error microphone location is the same location as the patient's ears. In adaptive ANC systems (not considered here), the result detected by the error microphone is used to adaptively update control filter coefficients in order to obtain further noise reduction and adapt to changing conditions.

* Corresponding author.
E-mail address: bea@byu.edu (B.E. Anderson).

https://doi.org/10.1016/j.apacoust.2020.107902
0003-682X/

Traditionally utilized time reversal (TR) techniques represent a matched signal process [10–11]. However, Tanter *et al.* showed that an inverse filter (i.e. deconvolution) could be used in conjunction with TR to provide a cleaner focusing signal because the inverse filter compensates for the frequency response of sound delivered from one point to another [12]. This paper will show that a 180° phase shifted, TR inverse filter is equivalent to the creation of an ANC control signal. Thus, when ANC is used with remotely placed sources, the principles of inverse filter TR focusing apply.

This paper reports some preliminary experiments that explore the effectiveness of using ANC for the remote delivery of a control signal. Various parameters are explored here, including the frequency content, the bandwidth of the signal (whether it is broadband or narrowband), and the reverberation time. The general process used here for proof of concept experiments involves using a microphone to record the sound emitted from one loudspeaker, the "noise" loudspeaker, and then inverting the phase of the response to allow for the creation of a control signal. A simulated version of the filtered-x LMS algorithm for ANC is done in post processing. The control signal comprises a convolution of the inverted noise recording and the reversed impulse response between another loudspeaker, the "control" loudspeaker, and the microphone. Any adaptive updating of the ANC filter coefficients is ignored in these proof of concept experiments and will be explored in future research. In traditional ANC, the control signal is broadcast from the control source and applying TR processing will cause the control response to arrive much later in time than is possible in traditional applications of ANC. Since it takes time for the time-reversed sound to traverse several room reflections before focusing, the noise signal needs to be known *a priori* to some degree. Fortunately, many MRI scan sequences are known *a priori*. The recorded responses are manually manipulated in post-processing to determine the optimal conditions for effective ANC, whereas a controller would be used in an actual implementation. The purpose of this study is to demonstrate that ANC can be done with remotely placed sources and to show an equivalence to the TR inverse filter, not to develop the necessary control algorithms and hardware needed for an actual implementation.

A parameterization study is conducted to control the noise produced by sinusoidal pulses played in a reverberation chamber and in a standard laboratory room with different center frequencies and pulse lengths. Additional results for the reduction of MRI noise recorded in an MRI facility and played back in the two aforementioned rooms (not in the MRI facility) will also be reported. Data was collected and analyzed in the Brigham Young University MRI facility and played back in other room environments for convenience. Reductions in the overall sound pressure level of MRI noise of up to 21 dB show the effectiveness of ANC using remotely placed sources in handling complex sound signals.

2. Equivalence of active control and the time reversal inverse filter

Time reversal (TR) is a signal processing technique capable of focusing sound energy to a selected position in space from a remote location [10–11,13–14]. In a room, TR can focus sound energy by first broadcasting a signal, for the purpose of this explanation, an impulse signal, from a loudspeaker for the forward step. This impulsive sound follows various paths in the room, with the direct sound path arriving at the microphone first and the reflected paths arriving at later times. During the backward step, this impulse response can then be flipped in time (time-reversed), and then broadcast from the original loudspeaker. The last arrivals in the impulse response are played first and the direct path arrival is played last. These emissions partially retrace their original traversed paths, and the timing is such that they simultaneously converge at the microphone, the focus point. The resulting response is a matched signal to the original impulse signal [10–11]. The implementation of TR just outlined is called reciprocal time reversal [14] and does not include the inverse filter step. Several researchers have explored the use of TR with audible sound in rooms [15–22], though none have explored ANC applications.

The aim of the forward step of TR is to obtain the impulse response, $h(t)$, between the loudspeaker at point A and the microphone at point B. Traditional TR involves simply a time reversal of $h(t) \rightarrow h(-t)$ prior to the backward step. However, the TR inverse filter, or deconvolution, constructs a signal that attenuates frequencies emphasized (e.g. room resonances) in the forward step and amplifies non-emphasized frequencies attenuated in the forward step. Thus, the ideal inverse filter is $H^{-1}(\omega)$. Note that signals represented in the time domain are denoted by lower case letters while the Fourier transforms of these signals are denoted by upper case letters. If the goal is to communicate a certain signal, $s(t)$ or $S(\omega)$, to point B, then the signal broadcast from point A during the backward step is

$$R(\omega) = S(\omega)H^{-1}(\omega) = S(\omega)\frac{\bar{H}(\omega)}{|H(\omega)|^2} \tag{1}$$

and the focal signal recorded by the microphone, $f(t)$ or $F(\omega)$, during the backward step of the TR inverse filter process is

$$F(\omega) = S(\omega)H^{-1}(\omega)H(\omega) = S(\omega)\frac{\bar{H}(\omega)}{|H(\omega)|^2}H(\omega) \tag{2}$$

To explicitly show the time reversal involved, the equality on the right-hand side of Eqs. (1) and (2) is included (since a complex conjugation, denoted by the $\bar{}$ operator, in the frequency domain is a reversal of time in the time domain). Note that to avoid dividing by zero in the inverse filter process, a regularization parameter (a small finite number) is typically added to the denominator term.

ANC aims to generate a signal at a desired location, that upon propagation from the control loudspeaker to that location, is the 180° phase shifted version of the noise at that location. Fig. 1 depicts a typical flow chart visualization of the ANC process. The noise signal generated by the MRI, $x(t)$, at point C propagates to the patient's ear location and a recording of that noise at the ear location (the error sensor location, which we'll also denote as point B) is

$$D(\omega) = X(\omega)P(\omega) \tag{3}$$

where $P(\omega)$ is the so called "plant" transfer function ($p(t)$ is the impulse response) from the noise source location to the error sensor location. An active controller is provided with $x(t)$ and given the goal of generating a signal from the control source located at point A that upon propagation to the error sensor is $-d(t)$. The so called "control filter", $w(t)$ or $W(\omega)$, is what the controller can modify

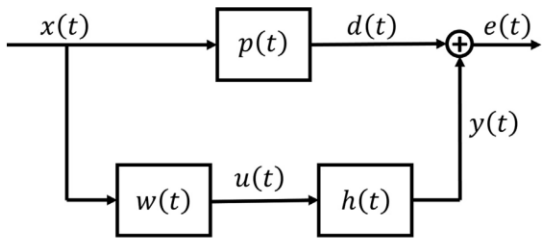

Fig. 1. Schematic drawing of the active noise control flow chart used in the filtered-x LMS algorithm.

and is what can be made adaptable based on feedback from the error sensor (adaptive control is not considered here). The signal from the controller, $u(t)$ or $U(\omega)$, is broadcast from the control loudspeaker located at point A. Traveling from point A to point B, $u(t)$ is convolved with the impulse response between these two locations, $h(t)$ (or the transfer function $H(\omega)$). The ideal control filter is

$$W(\omega) = -P(\omega)H^{-1}(\omega). \tag{4}$$

The signal that arrives at point B from the ideal control source is $y(t)$ or $Y(\omega)$,

$$Y(\omega) = -X(\omega)P(\omega)H^{-1}(\omega)H(\omega) = -D(\omega). \tag{5}$$

Thus, at point B, the location of the error sensor, the signal $e(t)$ is

$$e(t) = d(t) + y(t) = d(t) - d(t) = 0 \tag{6}$$

If the TR inverse filter is used to deliver $-d(t)$ to point B then we would set

$$S(\omega) = -X(\omega)P(\omega). \tag{7}$$

The focal signal when using the TR inverse filter becomes

$$F(\omega) = -X(\omega)P(\omega)H^{-1}(\omega)H(\omega) = Y(\omega) = -D(\omega). \tag{8}$$

This demonstrates that the TR inverse filter is equivalent to the non-adaptive ANC approach. The remotely placed source may be used with ANC since it is the same principle as using TR to focus energy at a remotely placed error sensor. It should be noted that the TR inverse filter process is used to reduce the amplitude of the side lobes in the TR focal signal, making the focal signal appear more like a delta function, thereby improving its spatio-temporal focusing capabilities [12,23].

In the above derivation assumptions were made. In order to construct the ideal control filter for ANC, $P(\omega)$ and $H(\omega)$ must both be known. In practice, this has been done both *a priori* as well as adaptively in real time. These transfer functions are also needed for the TR inverse filter to be equivalent to ANC in the construction of $S(\omega)$. In the case of MRI noise, if sequences are known in advance, they may be run *a priori* without a patient in the room, or with a mannequin in place of the patient, and the signal $d(t)$ can then be recorded ahead of time, allowing $P(\omega)$ to be known. Several sized mannequins may be used in this procedure to mimic different sized patients. With the MRI machine turned off, $H(\omega)$ may also be measured *a priori*. This procedure would provide the information needed to construct $W(\omega)$. Changes to the speed of sound in the room due to temperature or humidity changes would result in variations to $P(\omega)$ and $H(\omega)$ from the measured values, which would reduce the performance of ANC, although the reduction in performance would generally be pretty minimal. On the other hand, if desired, $P(\omega)$ and $H(\omega)$ could be obtained adaptively in real time, which would also allow the system to adapt to any changes that occur in the acoustic field. However, since the implementation proposed in this paper would have the control sources a significant distance away from the error sensors, this would imply that the adaptive system identification process would need to adapt fairly slowly. Reframing the problem with a TR perspective, to achieve optimal focusing of $y(t)$ at point B, the impulse response $h(t)$ must be of a finite length such that several reflections are included besides just the direct sound arrival. It is conceivable that ANC with remotely placed sources could be done with just the direct sound, but this would almost certainly result in amplifying the noise elsewhere in the room away from point B. If several reflections are included in $h(t)$ and/or if multiple control sources are used, then, just like with TR, the emissions from the control source(s) would be focused to point B and the use of the control source(s) would not be expected to increase the noise elsewhere in the room by much.

3. Experimental setup and procedure

In order to determine the limitations in using ANC with remotely placed sources, a parameterization study is conducted with pulse signals of different center frequencies and pulse lengths, with the results reported in Section 4. These parameterization experiments are first conducted in a reverberation chamber with dimensions 4.96 × 5.89 × 6.98 m. The reverberation chamber has a reverberation time equal to 6.89 s, and utilizes hanging scattering panels to diffuse sounds throughout the room. The second set of parameterization experiments is conducted in a standard laboratory room to determine if ANC is more effective in rooms with different reverberation times. The laboratory room measures 7.66 × 6.44 × 3.67 m and has a reverberation time of 0.68 s. A set of experiments to simulate the control of recorded MRI noise is then conducted in both of the aforementioned rooms and is reported on in Section 5. The setup for all of these experiments consists of two Mackie (Woodinville, WA) HR824 MK2 loudspeakers, one as the noise source and the other as the control source, and a 1.27 cm (1/2 in.) 46AQ GRAS (Holte, Denmark) random incidence microphone with a sensitivity of 53.03 mV/Pa. These are all connected to a data acquisition system for analysis. Fig. 2 shows a photograph of this setup in the reverberation chamber. Note that the loudspeakers are pointed away from the microphone as suggested by Anderson *et al.* for maximum focal amplitude in TR experiments [19].

The loudspeakers receive their respective input signals from Spectrum (Grosshansdorf, Germany) M2i.6022-exp signal generation cards that have 14-bit resolution. The microphone is powered by a GRAS 12AX 4-channel CCP power supply and is then connected to a Spectrum M2i.4931-exp acquisition card with 16-bit resolution and a sampling frequency of 100 kHz (the high sampling rate is not practical for actual ANC applications and was chosen such that it wouldn't impose any limiting factors here). The generation and acquisition are synchronized through custom developed LabVIEW software that was designed for TR experiments and can simultaneously broadcast multiple output signals and record from multiple input signals.

For this proof of concept study, a real-time ANC system is not used, but is simulated through post-processing. This is done by broadcasting a noise signal and a control signal separately from their corresponding loudspeakers and using the microphone to record each response individually. The noise signal, $d(t)$, is described in Eq. (3) while the control signal, $y(t)$, is described in Eq. (5). An appropriate time delay is then calculated between the noise signal and the control signal, and the amplitude of the control response is optimized to maximize the noise reduction through post-processing. This process simulates the simultaneous

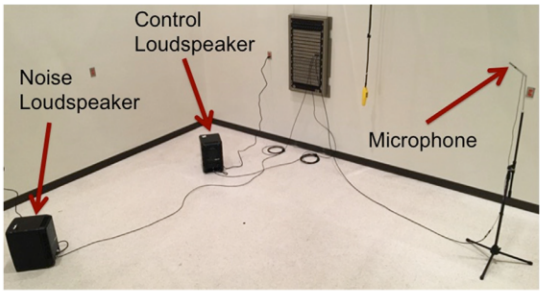

Fig. 2. Photograph of the experimental setup in a reverberation chamber with a noise loudspeaker, control loudspeaker, and microphone.

arrival of amplitude-matched noise and control signals at the microphone, assuming linear superposition.

It should be noted that the time delay in this case is several seconds, which depends on the length of the reversed impulse response used. Willardson *et al.* found that impulse responses longer than 2 s did not result in a larger peak amplitude of the TR focusing in this reverberation chamber [21]. It is likely that even a 2 s long impulse response is not necessary to achieve a focused control signal. The study by Willardson *et al.* did not explore the length of time necessary to achieve a certain quality of ANC. Certainly it is expected that shorter times could be used in rooms with lower reverberation times. A delay greater than a second is too long for real time ANC controllers to have any ability to control unknown noise signals. Fortunately, as described previously, the MRI sequence is often known *a priori* and the noise can be anticipated by assuming a linear, time-invariant system. As such, the time delay may not present as severe of a problem for this application as it would for an ANC system attempting to control unknown noise signals. The controller should still have the ability to make delayed adjustments for small system changes to update $W(\omega)$, or new measurements of the impulse response may be needed, for example with a new patient or a significant temperature change in the room. Delays of this length would also imply that an adaptive controller for ANC would have to converge very slowly, but fortunately many possible changes to the room for this application, such as temperature changes, would be expected to happen slowly.

3.1. Impulse response measurement

The impulse response(s), $h(t)$, needed to deliver an appropriate control signal from point A to point B is first obtained. A chirp signal, $c(t)$, a linear frequency sweep over a finite period of time, is broadcast from the control loudspeaker and its response, $r(t)$, is recorded at the microphone. In order to avoid the problems of dividing by zero using a deconvolution operation with frequency domain spectra, we instead take the cross-correlation, whose operation is denoted by$\star$, of $c(t)$ with $r(t)$ to obtain a scaled version (with a scale factor A) of the band-limited impulse response, $h(t)$, of the room between the control loudspeaker and the microphone [19] (see Fig. 3),

$$h(t) = Ac(t)\star r(t) \tag{9}$$

The impulse response then can be used to construct the ideal control filter (see Eq. (4)).

3.2. Generate control signal

The ideal control signal consists of the convolution of the noise signal, $x(t)$, the impulse response between the noise loudspeaker and the microphone, $p(t)$, and the deconvolution impulse response between the control loudspeaker and the microphone, $h_d(t)$, all multiplied by -1 to invert the phase. $h_d(t)$ is obtained from the inverse Fourier transform of $H^{-1}(\omega)$. Thus, in the frequency domain, the ideal control signal is $-X(\omega)P(\omega)H^{-1}(\omega) = X(\omega)W(\omega)$. From a TR perspective, the broadcast of this ideal control signal from the control loudspeaker would result in a focusing of $-X(\omega)P(\omega)$ at the microphone, which should cancel the noise, $X(\omega)P(\omega)$, at the microphone location.

Fig. 4(a) and 4(b) display the recorded noise signal, $d(t)$, and the control signal, $y(t)$, respectively, and while the two signals appear to be visually similar in shape, they reach the microphone at different times and with different amplitudes. This is because, as discussed previously, the TR process requires some finite amount of time for the reversed emissions to propagate along their original

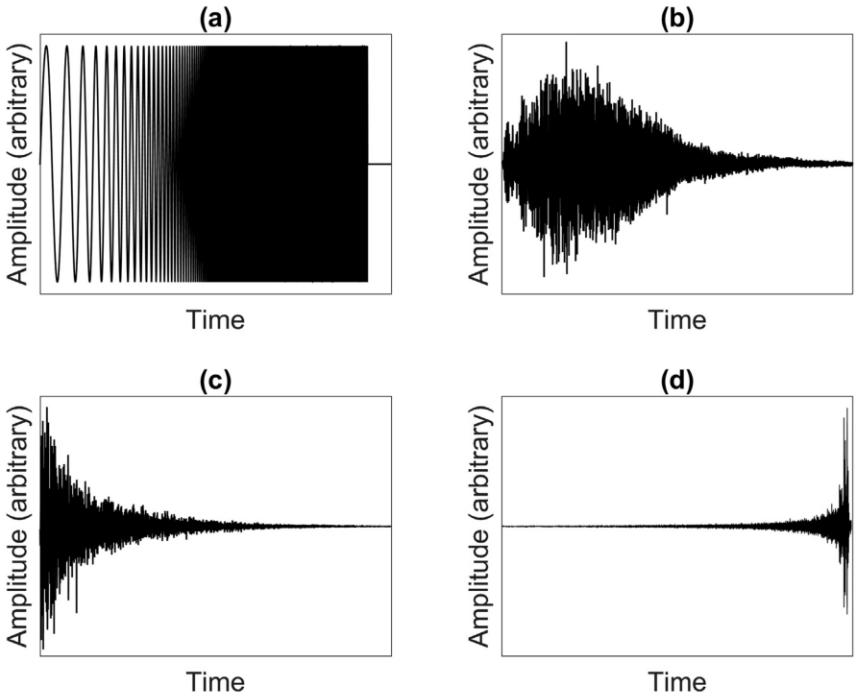

Fig. 3. Illustration of the cross-correlation of (a) the chirp signal and (b) the chirp response to obtain (c) an impulse response. The impulse response is time-reversed and using the deconvolution method, a (d) time-reversed impulse response is obtained. Signals have been normalized for illustrative purposes.

paths before they constructively interfere upon arrival at the microphone.

The signals $d(t)$ and $y(t)$ need to be time aligned to achieve cancelation. One of the issues is that these are discrete time signals and it is probable that the most accurate time delay is not an integer number of time samples. To account for this, an interpolation function is applied to these signals to increase the number of samples for each signal, creating $\hat{d}[n]$ and $\hat{y}[n]$. A discrete time cross-correlation between $\hat{d}[n]$ and $\hat{y}[n]$, allows the integer number of interpolated samples between them, k, to be determined for optimal alignment, $\hat{d}[n] \rightarrow \hat{d}[n-k]$, as if the two signals arrived at the microphone at the same time. The interpolation and time delays used here are not practical but are used for this proof of concept study. This helps to ensure that the ANC reductions are not due to any signal processing artifacts. In practice, $y(t)$ would need to be broadcast in advance by a time that corresponds to k, and an optimal k would need to be determined *a priori* that is as short as possible to still achieve the desired amount of noise reduction.

With the determined k-value, $\hat{d}[n-k]$ becomes the time delayed noise response. This is done by adding k-number of zeros in front of $\hat{d}[n]$ (see Fig. 4(c)). Though $\hat{d}[n-k]$ and $\hat{y}[n]$ are time aligned, $\hat{y}[n]$ needs to be amplitude matched to $\hat{d}[n-k]$ in order to achieve the greatest noise reduction. An optimal weight factor, μ, is determined such that, when multiplied by $\hat{y}[n]$, will provide the greatest reduction in overall sound pressure level (OASPL). Fig. 4(d) displays the weighted control response, $\mu\hat{y}[n]$, and Fig. 4(e) displays the summation signal, $\hat{e}[n] = \hat{d}[n-k] + \mu\hat{y}[n]$, simulating the result of the ANC process. The OASPL of $e[n]$ (control on) is calculated and compared to the OASPL of $\hat{d}[n-k]$ (control off) to determine the overall noise reduction. The OASPL for both situations is

$$L_{\mathrm{OASPL}} = 10\log_{10}\left(\frac{\sum p[n]^2}{{p_{ref}}^2}\right) \tag{10}$$

where $p[n]$ is the root mean squared pressure of a signal (either $\hat{e}[n]$ or $\hat{d}[n-k]$), and $p_{ref} = 20$ μPa.

4. Parameterization study results

Following the procedures outlined in Section 3, the frequency and pulse length of a pulse signal, used as $\hat{x}[n]$, are varied to quantify the capabilities of ANC to reduce different types of noise. This parameterization study is performed in the reverberation chamber, where TR is expected to have the greatest focal amplitude due to its longer reverberation time [18], and in a standard laboratory room with a much lower reverberation time and 10% smaller volume, where TR is expected to have a higher temporal focus quality [19–20]. A higher amplitude focus just means the μ gain doesn't need to be as large, but a higher temporal focus quality should allow the most accurate available delivery of $-d(t)$ to point B. The pulse length, which is doubled for every successive test, ranges from a pulse consisting of simply a half cycle of a sine wave to a maximum length of 2.048 s. The center frequency of the pulse ranged from 63 Hz to 16 kHz. Center frequencies were chosen to line up with the standardized octave band center frequencies [24]. These signals help determine the ability of ANC to control different frequencies and whether narrowband or broadband signals are easier to control over the audible range of hearing. Performing these experiments in rooms with different reverberation times also

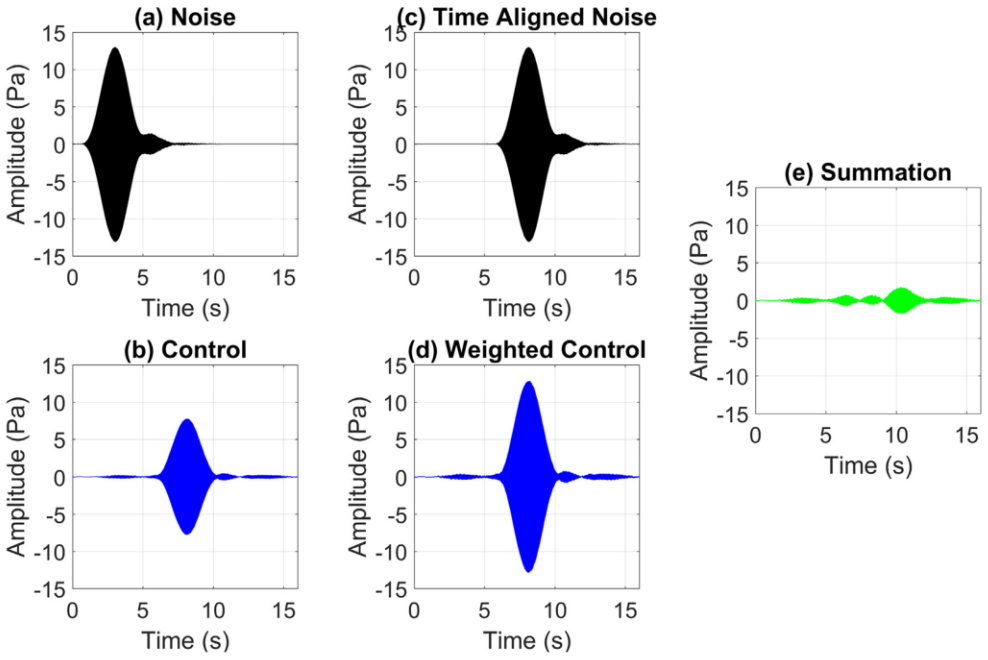

Fig. 4. Overview of the simulation of active noise control. (a) Noise response $\hat{d}[n]$ from the noise loudspeaker. (b) Control response $\hat{y}[n]$ from the control loudspeaker. (c) Time aligned noise response $\hat{d}[n-k]$. (d) Amplitude weighted control response $\mu\hat{y}[n]$. (e) The summation of $\hat{d}[n-k]$ and $\mu\hat{y}[n]$,$\hat{e}[n]$, to achieve noise cancelation.

helps determine if reverberation time is an important factor for implementing ANC. The results for the OASPL noise reductions for the two rooms are found in Fig. 5.

It is clear from the results depicted in Fig. 5 that greater reductions are found with lower frequency signals for all pulse lengths. This is a common finding, that ANC is better able to attenuate low frequencies, because the phase mismatch errors are typically smaller [25–28]. A trend is also observed at almost all frequencies when the pulse length exceeds 1 ms, as reductions increase as the pulse length increases, even at the highest frequencies. This implies that narrowband signals are easier to control, which is also commonly seen for ANC implementations [25–28]. It is also clear from Fig. 5 that reverberation time is an important factor for implementing ANC with remotely placed sources, as the results from the laboratory room show that narrowband signal reductions are still comparable to the reverberation chamber and that even broadband signals are easier to control in a less reverberant environment.

5. Active control of MRI noise results

The noise reducing capability of ANC for MRI noise will now be explored. The noise from four MRI scanning sequences were recorded in the MRI facility on the campus of Brigham Young University. The MRI is a Siemens (Munich, Germany) TIM-Trio scanner with a magnetic field strength of 3 T. The scanning sequences used for this study are the Constructive Interference Steady State (CISS), Echo Planar Imaging (EPI) Diffusion, Magnetization-Prepared Rapid Gradient-Echo (MP-RAGE), and True Fast Imaging with Steady Precision (TrueFISP or TRUFI) sequences.

The MRI noise signals were obtained by placing the same microphone used previously outside of the MRI's active, magnetic-field cancellation zone with an approximate distance of 4.57 m (15 ft.) between the microphone and the MRI scanner. Though the measured sound level at the microphone is less than the level inside the bore, where a patient's head would be during a scanning sequence, the purpose of the current study is to quantify the performance of ANC for actual MRI noise signals, irrespective of how loud they are or if it is done in the optimal location for the reductions. If reductions are achieved in one part of the room, then similar reductions should be possible to obtain in other room locations as well (though the bore presents a more confined space). Placing the microphone outside of the magnetic-field cancellation zone was done for convenience to avoid any danger with placing a metallic object near the MRI scanner. After the recordings were made in the room with the MRI scanner, the ANC proof of concept experiments were conducted in facilities without equipment constraints and to avoid interruption of actual scans for medical purposes. These ANC experiments were conducted in the reverberation chamber and the laboratory room, described previously, with the laboratory room having a comparable reverberation time as the room with the MRI scanner.

Given that a scan sequence can run for long periods of time producing periodic noise, the noise signals used in the experiments were shortened to 6–8 *s*, depending on the signal, to contain the representative periodicity of each signal. It is expected (due to this periodicity) that any noise reductions within these time intervals should translate over into reductions over the entire duration of however long the MRI scan actually takes. Though the noise signals were shortened to differing lengths of time, the noise response of each signal was trimmed such that each had the same time duration. The same holds true for the control signals' responses, and when the OASPL reductions were calculated for each MRI scan, all signals were of equal length; this way the OASPL calculation is over the same length in time for each scan. Fig. 6 displays the recorded noise waveforms for each of the 4 scan sequences.

Both the CISS and TRUFI scans have low frequency tones that remain throughout the duration of the scan. One of the main differences between the two is that the TRUFI scan has an audible, short-duration, buzzing sound that occurs every few seconds. The MP-RAGE scan also has the characteristic of a prominent lower frequency tone, but only for just over a second at a time, followed by brief silence. This is an important signal to analyze as well because of those silent pauses, since added noise, when there should be silence, is undesirable. The EPI Diffusion scan has very quick bursts of sound that repeat in a small amount of time.

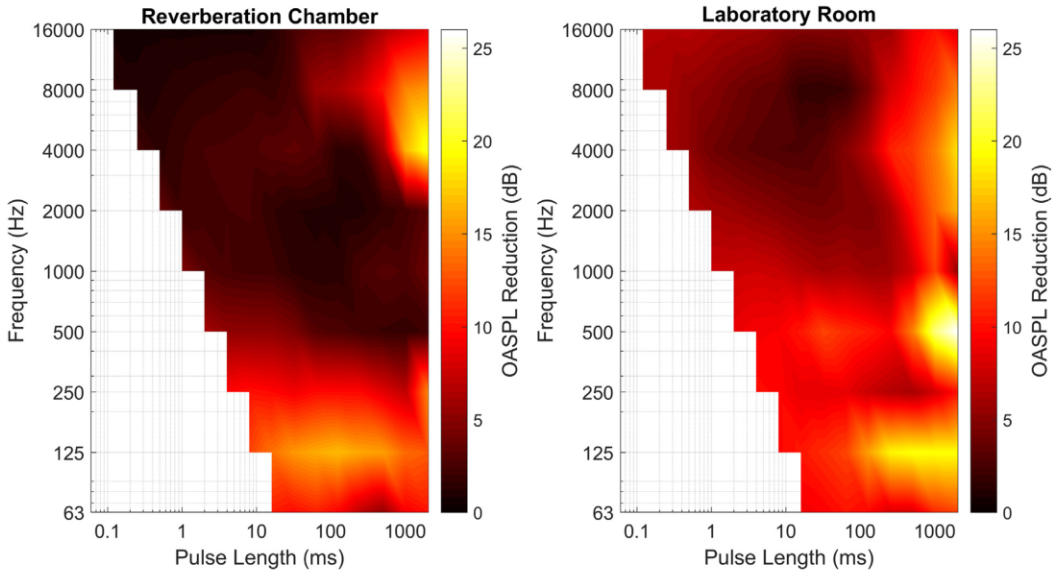

Fig. 5. Comparison between the OASPL noise reductions of pulse signals played in a reverberation chamber and a laboratory room expressed versus frequency and pulse length (s) using active noise control. The color bar represents OASPL noise reductions in dB. The white area indicates no data.

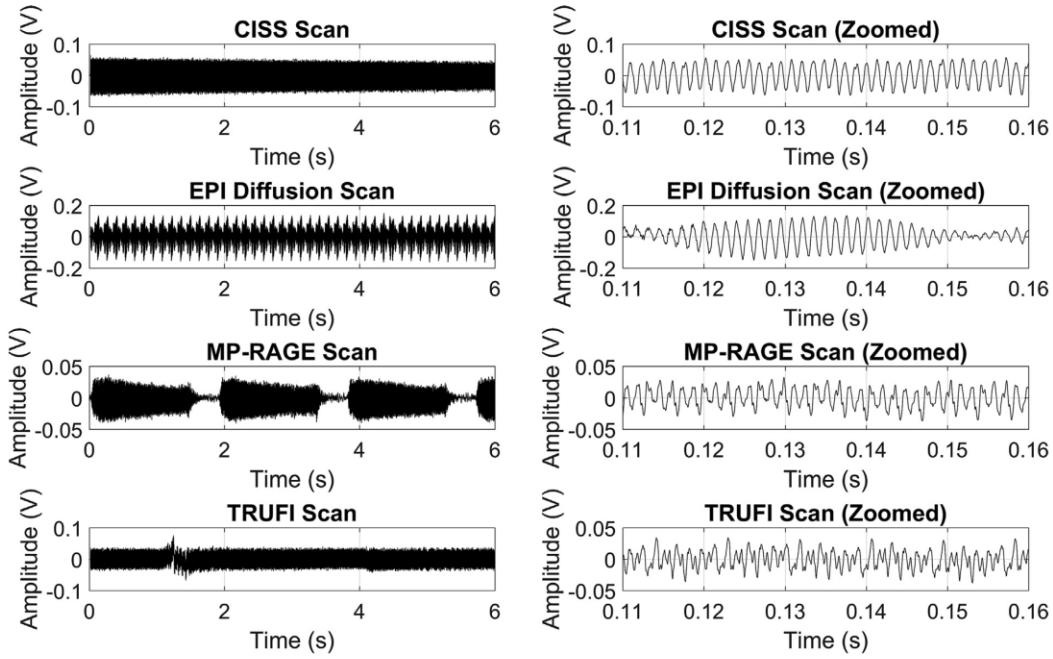

Fig. 6. Recorded MRI noises from the BYU MRI facility. The left column shows the full length of each noise signal. The right column shows zoomed in portions of the same signals to show respective signal behavior and periodicity.

Though these are not all the signals that an MRI scanner is able to produce, this set contains a variety of behaviors that are representative of typical MRI scans.

5.1. Influence of room reverberation

The recordings of the aforementioned MRI noise were broadcast through the noise loudspeaker in the reverberation chamber and in a standard laboratory room to quantify the ANC reductions using the procedure described in Section 3. As before, the control loudspeaker attempts to reduce the noise recorded at the microphone. Fig. 7 shows the time-domain view of the four aforementioned signals comparing when the control signal is on and off in the reverberation chamber. Likewise, Fig. 8 shows the results from the standard laboratory room. The OASPL reduction results of these experiments are shown in Fig. 9.

It is apparent that a room's reverberation time greatly impacts the effectiveness of ANC in reducing MRI noise. Even though TR is able to provide a higher amplitude focus in a more reverberant environment, it appears that a room with a lower reverberation time, and thus a higher temporal quality for TR, allows greater noise reductions to be achieved with ANC. These results are promising in that ANC is capable of reducing complex noise signals with various behaviors using a remotely placed control source. It should be noted that these results are obtained with a single control loudspeaker, but since the control loudspeakers may be placed at locations away from the MRI scanner, more loudspeakers should be able to be used to achieve greater reductions.

5.2. Spatial extent of control

The CISS scan recording was selected to quantify the spatial extent of the noise reduction in the standard laboratory room. In this case the CISS noise recording was trimmed down to a duration of 4.4 s. A custom built Macron Dynamics Inc. (Croydon, PA) microphone positioning system was setup to measure the noise and the ANC control response over a 170 cm span with measurements every 17 cm, with each measurement position at a height of 1.45 m from the floor. The recordings at each microphone position are time synchronized with the emissions to simulate 11 microphones simultaneously recording at the 11 scan positions. The noise loudspeaker is setup 3.1 m away from the selected control location, while the control loudspeaker is setup 2.7 m away from the control location. Both loudspeakers are pointed away from the microphone and both are approximately at the same height as each of the microphone positions. The noise and control loudspeakers were setup 3.0 m apart from each other. Again, the same procedure outlined in Section 3 was carried out, using the recorded CISS noise as the signal broadcast from the noise loudspeaker.

Fig. 10 displays the results of the ANC simulations. Fig. 10(a) displays the results with control off versus control on at the selected control location while Fig. 10(b) displays the OASPL reduction results at each of the microphone positions. The OASPL for the CISS noise is 76.6 dB, while the OASPL with ANC is 60.5 dB. At other spatial locations the OASPL is increased, showing that the reduction of OASPL is only achievable at one location, as expected. This experiment was actually conducted a few different times and different time delays were utilized as well to ensure repeatability of the results. We note that these reduction results include the transient portions of the recorded signals. In the steady state, between times 1.6 s and 4.4 s, the OASPL of the CISS noise is 77.1 dB and the ANC control result has an OASPL of 56.1 dB.

In this application, reduction is only needed at the location of the patient's ears to provide a zone of reduced noise. An increase of noise at other locations, while not desirable, may be tolerable since no other listeners would be in the room. A higher temporal quality focal signal in TR applications implies that more energy is focused at the selected control location (the error microphone

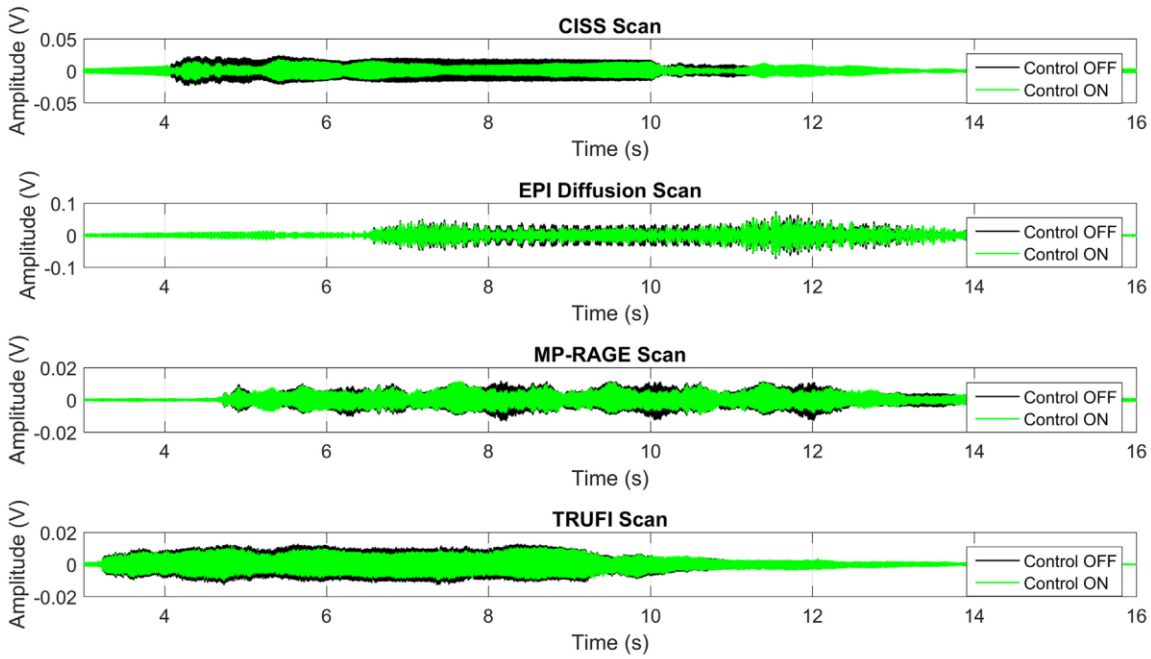

Fig. 7. Time-domain comparison of the selected four MRI scanning sequences when the control signal is on and off in the reverberation chamber.

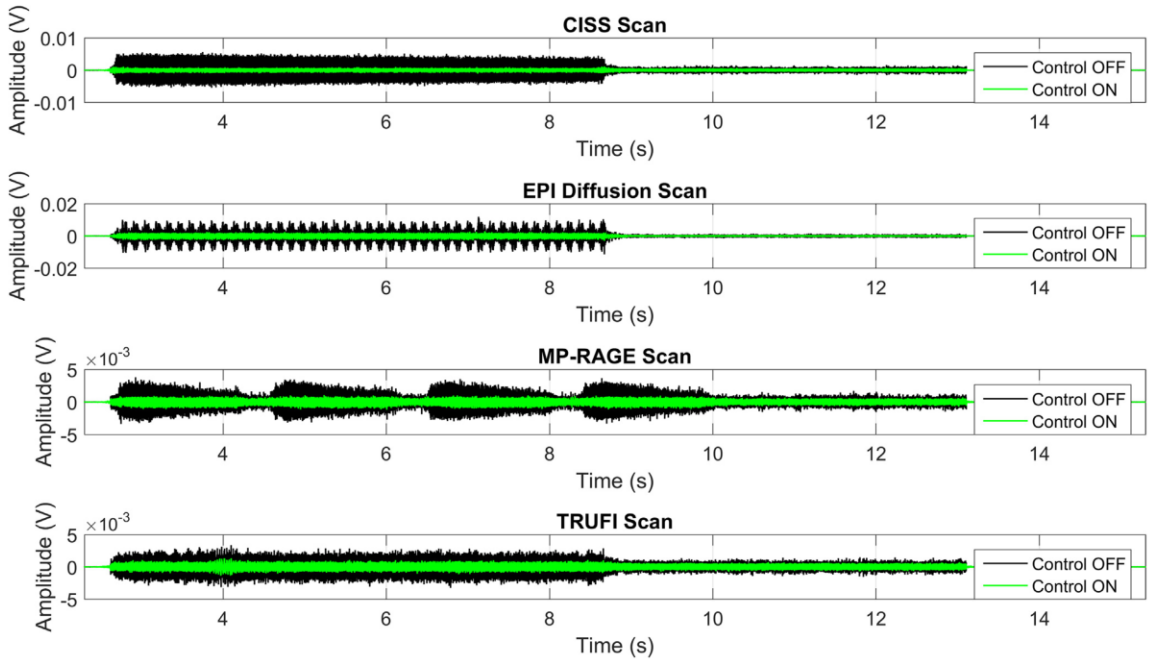

Fig. 8. Time-domain comparison of the selected four MRI scanning sequences when the control signal is on and off in the standard laboratory room.

and location of the patient's ears) and less energy is delivered elsewhere. The correlation of improved temporal quality with improved spatial confinement of the focusing was discussed by Anderson *et al.* [23]. It is well known in TR research that the more physical sources that are used to generate the TR focusing, the higher the temporal quality of the focusing. The increased spatial confinement of the TR focusing means that the ANC process should be better able to deliver the control signal only to the selected control location. It should then be expected that the noise would not be increased away from the selected control location when more

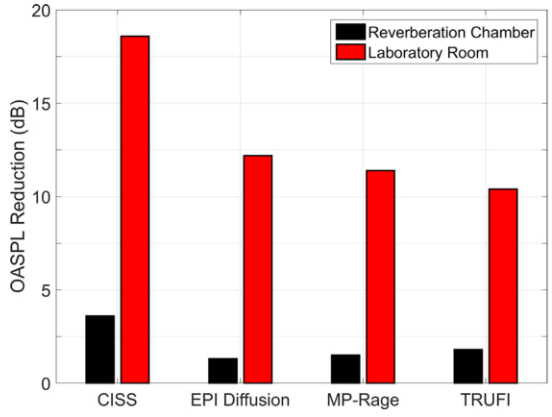

Fig. 9. Comparison of different MRI scans and their corresponding OASPL noise reductions in rooms with different reverberation times.

control loudspeakers are used, and when the technique is used in less reverberant rooms.

The experiments presented in this paper utilized a single error sensor to achieve control over a spatial extent of approximately 17 cm. The spacing between a typical person's ears is typically greater than 17 cm. Thus it may not be possible to use one error sensor and expect significant noise reduction at both ears of the patient. In order to achieve control at both ears of the patient, two error sensors may be utilized, placed near each of the patient's ears. This type of approach would incorporate the transfer function associated with each of the two error sensors at both error sensors and hence simultaneous control at both ears would be possible. Thus, noise reduction of up to 16 dB may still be possible with a dual error sensor scheme. Further, the spatial extent of the noise reduction depends on the frequency content utilized in the control algorithm. The use of less high frequency content should broaden the control region at the expense of being unable to reduce that high frequency content. Additional control algorithms may be explored for future research.

6. Conclusion

This paper provides proof of concept experiments that demonstrate the feasibility of using active noise control (ANC) with remotely placed sources for MRI noise control applications. A parameterization study explored the frequency dependence and signal duration (i.e. narrowband or broadband) for pulse signals in a reverberation chamber and in a less reverberant laboratory room. The results show that low frequency signals allow for more consistent reductions, and longer duration signals (narrowband) also achieve greater noise reductions.

MRI noise from four different scan sequences were recorded and ANC simulations were demonstrated in a reverberation chamber and a standard laboratory room, each with very different reverberation times. These noises are representative of various MRI scan sequences and illustrate that ANC used in this application can reduce complex signals. Results from the parameterization study and the MRI noise control study show that ANC is capable of reducing both simple and complex signals up to 20 dB. Results from both studies, namely the MRI study, show that a room with a smaller reverberation time yields greater noise reductions than results in a more reverberant room. This is a promising result because MRI facilities are not typically as reverberant as reverberation chambers.

The paper also demonstrated the equivalence of ANC and the time reversal (TR) inverse filter. In TR research, the longer the reversed impulse response and the more sources used, the higher the amplitude of the focused of sound. It follows then that if longer time impulse responses are incorporated into the ANC control filter then the cancellation may be done more efficiently since the TR inverse filter is able to focus high amplitude energy with longer reversed impulse responses. The lower reverberation time of the laboratory room allows for a higher temporal quality focal signal with TR. A higher temporal quality focal signal implies that the energy at other spatial locations away from the focal location will be less. The use of additional loudspeakers is also well known in TR research to provide higher temporal quality focusing. Thus, the combination of a lower reverberation time room and more loudspeakers used is expected to provide a more spatially confined ANC reduction, which would amplify the noise outside of the selected control location by less. Utilizing two error sensors should allow a wider spatial extent of the control region to obtain control at both of the patient's ears.

Research on using real time controllers would need to be done and incorporation of the controller with *a priori* scan sequence information would need to be developed. The controller would automatically provide the time delay and amplitude adjustment necessary to optimize the noise control. Additionally, the required amount of reverberation to include in the TR process would need

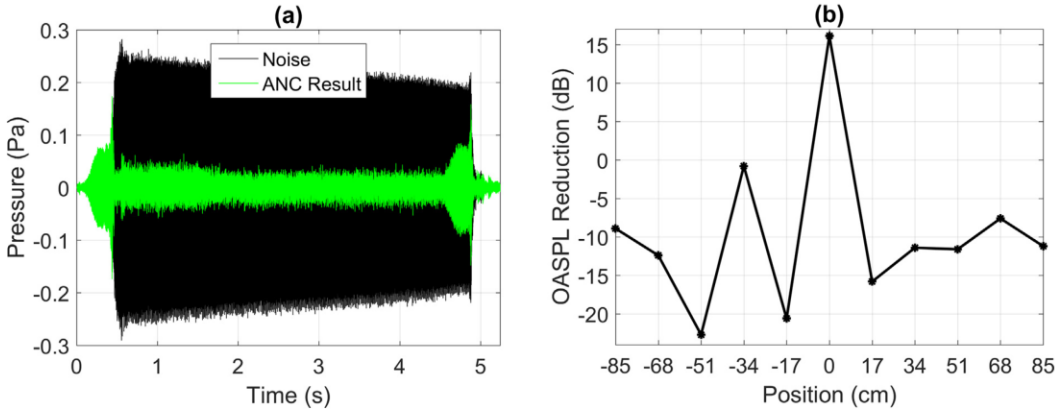

Fig. 10. (a) Noise at the desired control location with the ANC off and on. (b) OASPL reduction at each microphone position with ANC on.

to be optimized for brevity while still maintaining adequate control at the desired location. The control signal must be broadcast before the noise has been generated, limiting the range of applications. Fortunately for MRI noise, signal information is often known *a priori* and the environment is quite stable.

Declaration of Competing Interest

The author declare that there is no conflict of interest.

Acknowledgements

This work was funded by the BYU Office of Research and Creative Activities, the BYU MRI facility, and the BYU College of Physical and Mathematical Sciences.

References

[1] Lee N, Park Y, Lee GW. Frequency-domain active noise control for magnetic resonance imaging acoustic noise. Appl Acoust 2017;118:30–8.
[2] Pla FG, Sommerfeldt SD, Hedeen RA. Active control of noise in magnetic resonance imaging. In: Proc Active 95, Newport Beach, CA, USA; 1995. p. 537–582.
[3] Ravicz ME, Melcher JR, Kiang NY. Acoustic noise during functional magnetic resonance imaging. J Acoust Soc Am 2000;108(4):1683–96.
[4] Wigham S, Rodgers J, South M, McConachie H, Freeston M. The interplay between sensory processing abnormalities, intolerance of uncertainty, anxiety and restricted and repetitive behaviours in autism spectrum disorder. J Autism Dev Disord 2014;45(4):943–52.
[5] Kana RK, Libero LE, Moore MS. Disrupted cortical connectivity theory as an explanatory model for autism spectrum disorders. Phys Life Rev 2011;8:410–37.
[6] Optoacoustics, LTD. OptoActive II ANC Headphones. http://www.optoacoustics.com/medical/optoactive-ii (Last viewed March 16, 2020).
[7] Ahn CB, Cho ZH. Analysis of the eddy-current induced artifacts and the temporal compensation in nuclear magnetic resonance imaging. IEEE Trans Med Imaging 1991;10(1):47–52.
[8] Spees WM, Buhl N, Sun P, Ackerman JJH, Neil JJ, Garbow JR. Quantification and compensation of eddy-current-induced magnetic-field gradients. J Magn Reson 2011;212(1):116–23.
[9] Ravicz ME, Melcher JR. Isolating the auditory system from acoustic noise during functional magnetic resonance imaging: examination of noise conduction through the ear canal, head, and body. J Acoust Soc Am 2001;109:216–31.
[10] Parvulescu A, Clay CS. Reproducibility of signal transmission in the ocean. Radio Elec Eng 1965;29:223–8.
[11] Clay CS, Anderson BE. Matched signals: the beginnings of time reversal. Proc Meet Acoust 2011;12:055001.
[12] Tanter M, Thomas J-L, Fink M. Time reversal and the inverse filter. J Acoust. Soc Am 2000;108(1):223–34.
[13] Fink M. Time reversed acoustics. Phys Today 1997;50:34–40.
[14] Anderson BE, Griffa M, Larmat C, Ulrich TJ, Johnson PA. Time Reversal, Acoust. Today 4(1);5–16 (28).
[15] Candy JV, Meyer AW, Poggio AJ, Guidry BL. Time-reversal processing for an acoustic communications experiment in a highly reverberant environment. J Acoust Soc Am 2004;115(4):1621–31.
[16] Meyer AW, Candy JV, Poggio AJ. Time reversal signal processing in communication – a feasibility study. Lawrence Livermore Nat Lab Lib 2002;246245.
[17] Yon S, Tanter M, Fink M. Sound focusing in rooms: the time-reversal approach. J Acoust Soc Am 2003;113(3):1533–43.
[18] Ribay G, de Rosny J, Fink M. Time reversal of noise sources in a reverberation room. J Acoust Soc Am 2005;117(5):2866–72.
[19] Anderson BE, Clemens M, Willardson ML. The effect of transducer directivity on time reversal focusing. J Acoust Soc Am 2017;142(1).
[20] Denison MH, Anderson BE. Time reversal acoustics applied to rooms of various reverberation times. J Acoust Soc Am 2018;144(6):3055–66.
[21] Willardson ML, Anderson BE, Young SM, Denison MH, Patchett BD. Time reversal focusing of high amplitude sound in a reverberation chamber. J Acoust Soc Am 2018;143(2):696–705.
[22] Denison MH, Anderson BE. The effects of source placement on time reversal focusing in rooms. Appl Acoust 2019;156:279–88.
[23] Anderson BE, Douma J, Ulrich TJ, Snieder R. Improving spatio-temporal focusing and source reconstruction through deconvolution. Wave Motion 2015;52(9):151–9.
[24] Pierce AD. Acoustics: An introduction to its physical principles and applications. Woodbury, New York): Acoustical Society of America; 1989. p. 58.
[25] Widrow B, Stearns SD. Adaptive signal processing. Prentice-Hall, Englewood Cliffs, New Jersey; 1985. pp. 302–367.
[26] Gordon RT, Vining WD. Active noise control: a review of the field. Am Indust Hyg Assoc J 1992;53(11):721–5.
[27] Nelson PA, Elliot SJ. Active control of sound. Academic Press Inc., San Diego, California; 1993. p. 161-203.
[28] Jiang J, Li Y. Review of active control techniques with emphasis on sound quality enhancement. Appl Acoust 2018;136:139–48.

Appendix C

C.1 Introduction

This section contains the MATLAB© script that I wrote with the assistance of Adam Kingsley to calculate the pressure of a time reversal focus peak at various locations inside of a modeled room. It uses a technique known as modal summation, which can be found in many textbook sources. The complexity of this code, and memory that it takes to run, makes it a valuable tool when attempting to approximate a room acoustics environment through the process of modal summation.

C.2 MATLAB© Script

```
%% This code was written as a numerical solution to equation 6-5.20 from Pierce,
 % and by extension the eq'n 2.39 in Kleiner/Tichy "Acoustics of Small Rooms"
 % with modifications by Timothy Leishman (BYU) to generate
 % his equation 4.2.2-96.
 % written by Brian Patchett with Adam Kingsley Of Brigham Young University, August/September 2019
 % based on a prior solution by Brian Patchett for a lower mode number
 % this code is designed to handle a high number of modes in a room by
 % utilizing parallel processing on the CPU and GPU.
 % this code is the intellectual property of Patchett/Kingsley 2019

%% opening section

clc
clear
close all

%% variables

flag = 1;                       % the flag value selects the receiver position vectors 1 = free field, 2 = wall,
                                % 3 = edge, 4 = corner, 5 = four positions field, wall, edge, corner

f = 500.25:0.25:15000;          % bandwidth of chirp, 0.25 spacing is required to differentiate modal peaks.

j = sqrt(-1);                   % by explicitly defining j matlab has an easier time using it
s = 343;                        % speed of sound
w = 2*pi.*f;                    % omega radial frequency
A = 1;                          % arbitrary amplitude
rho = 1.21;                     % density of air
Lx = 5.89;                      % room dim in x
Ly = 4.96;                      % room dim in y
Lz = 6.98;                      % room dim in z
V = Lx*Ly*Lz;                   % room volume
pref = 20E-6;                   % reference pressure for dB
k = w/s;                        % array of k values
prefix = -4*pi*A/V;             % coefficient value outside of sum
mult = 0.20;                    % white noise multiplier

%% recreates the Nutter plot based on visual inspection
% clc
% close all
% AA = [110 9.5;125 10.5;150 7.2;230 8.9;280 8.7;445 8.5; ...
% 500 8.4;560 8.3;890 8.1;1000 7.4;1120 6.7;1700 5.1;2000 4.4; ...
% 2245 4;3564 2.6;4000 2.2;4490 1.9];

% semilogx(AA(:,1),AA(:,2))

%% create the frequency based damping term by using experimental values of the RT60

% RT60 is frequency dependent, this vector is generated by calculating the
% RT60 with Schroeder integration for an experimental IR in the Impulse Responses
% code. That code interpolates it to have a spacing resolution of 0.25 Hz.

load('RT60_model.mat')
```

```
RT60_model = RT60_model';

% frequency range of the model going to the 16 kHz octave band
f_model = 500.25:0.25:16000;

% RT60 = zeros(1,length(f_model));
% RT60(1,1:end) = 4.174; % this is a flat rt60 for testing

% this line is for using the frequency range 500Hz-15kHz
RT60 = RT60_model;

% this makes the RT60 model the same length as the frequency spectrum by assuming that the values
% from f = 0-500 Hz match the value at 501 Hz, then from 501- 15000 Hz it is the model
% RT60 = zeros(1,length(f_model));
% RT60(1,1:2000) = 4.174;            % approximate value of RT60 (in seconds) from 0-500 Hz,
% RT60(1,2001:end) = RT60_model;

figure
plot(f_model,RT60)
title('RT60 Model for Damping Term')
xlabel('Frequency (Hz)')
ylabel('Time (s)')
grid on


delta = 6.91./RT60;                % damping factor, frequency dependent through RT60, found in 661 notes
                                   % as eq'n 4-2.2.101
delta_c= delta/s;                  % in the algorithm (eq'n 4-2.2.96) delta/c is used, this variable is
                                   % created for use in the algorithm for simplicity sake.

figure
plot(f_model,delta)
title('Damping as a Function of Frequency')
xlabel('Frequency (Hz)')
ylabel('Damping Coefficient (\delta)')
grid on

%% position vectors for numerator Psi functions (eq'n 4-2.2.96) in meters
 % it creates matrix 'pos' of each vector where the ith element is x, y, or z, and the jth element
 % is the position number of the reciever.

x0 = 5.8;     % source position
y0 = 4.8;     % source position
z0 = 0.08;    % source position

% x0 = 2.8;    % source position 2
% y0 = 4.8;    % source position
% z0 = 6.9;    % source position

% x0 = 2.8;    % source position 3
% y0 = 3.8;    % source position 3
% z0 = 6.9;    % source position

% x0 = 2.8;    % source position 4
% y0 = 3.8;    % source position 4
% z0 = 4.5;    % source position 4
```

```
if flag == 1 % FREE FIELD 18 free field positions
   xp=single([3.13 3.58 3.20 2.18 2.08 1.63 2.03 2.38 1.23 3.85 4.46 2.94 1.94 ...
      3.92 2.89 1.50 1.40 3.35]);
   yp=single([2.06 2.80 3.90 2.89 1.74 3.34 1.65 2.93 1.49 2.00 1.38 2.62 1.87 ...
      3.40 3.15 2.19 3.68 1.84]);
   zp=single([1.51 1.79 1.51 1.63 1.87 1.64 1.72 1.86 1.77 1.64 2.18 2.12 1.49 ...
      1.29 1.52 1.77 2.18 1.80]);

elseif flag == 2 % WALLS 18 total positions, 6 per wall that are nonadjacent to source
   xp=single([0.01 0.01 0.01 0.01 0.01 0.01 1.63 2.03 2.38 1.23 3.85 4.46 2.94 1.94 ...
      3.45 3.92 2.89 1.50]);
   yp=single([2.06 1.94 2.80 3.90 2.89 1.74 0.01 0.01 0.01 0.01 0.01 0.01 2.62 1.87 ...
      1.85 3.40 3.15 2.19]);
   zp=single([1.51 2.01 1.79 1.51 1.63 1.87 1.64 1.72 1.86 1.77 1.64 2.18 0.01 0.01 ...
      0.01 0.01 0.01 0.01]);

elseif flag == 3 % EDGES 18 positions, 6 per edge along edges away from source
   xp=single([0.01 0.01 0.01 0.01 0.01 0.01 2.03 2.38 1.23 3.85 4.46 2.94 0.01 ...
      0.01 0.01 0.01 0.01 0.01]);
   yp=single([0.01 0.01 0.01 0.01 0.01 0.01 0.01 0.01 0.01 0.01 0.01 0.01 0.01 1.87 ...
      3.40 3.15 2.19 3.68 1.84]);
   zp=single([1.51 1.79 1.51 1.63 1.87 1.64 0.01 0.01 0.01 0.01 0.01 0.01 0.01 0.01...
      0.01 0.01 0.01 0.01 0.01]);

elseif flag == 4 % CORNERS 8 corners of the room, floor then ceiling
   xp=single([0.01 5.88 5.88 0.01 0.01 5.88 5.88 0.01]);
   yp=single([0.01 0.01 4.95 4.95 0.01 0.01 4.95 4.95]);
   zp=single([0.01 0.01 0.01 0.01 6.97 6.97 6.97 6.97]);

elseif flag == 5 % single position, one for each regime, field, wall, edge, corner respectively
   xp=single([3.13 0.01 0.01 0.01]);
   yp=single([2.06 2.06 0.01 0.01]);
   zp=single([1.51 1.51 1.51 0.01]);
end

% horizontally concatonate the vectors to create a matrix of position values
pos = horzcat(xp',yp',zp');

%% calculate number of modes needed in each dimension. create index vectors for calculation loops.

% the number of modes does not need to be increased to include all tangnetial and oblique
% modes that occur in z-dim above the lower mode numbers of x and y. Brian Anderson calculated that
% we are already on the correct order of modes for an accurate representation of the given room.
xmodes = round((2*Lx.*f(end))./s,-1); % axial mode number to reach frequency band
ymodes = round((2*Ly.*f(end))./s,-1); % the -1 value rounds up to the nearest tens
zmodes = round((2*Lz.*f(end))./s,-1); % this overestimates the mode numbers intentionally

nx = single((1:xmodes)-1);     % index arrays for counting in the following loops
ny = single((1:ymodes)-1);     % index arrays for counting in the following loops
nz = single((1:zmodes)-1);     % index arrays for counting in the following loops

xindex=single(1:length(nx));   % convert to single precision for GPU processing
yindex=single(1:length(ny));   % convert to single precision for GPU processing
zindex=single(1:length(nz));   % convert to single precision for GPU processing
kindex=single(1:length(k));    % convert to single precision for GPU processing
```

```
pindex=single(1:length(pos));  % convert to single precision for GPU processing


epsx = ones(1,xmodes,'single').*2; % epsilon values for Lambda kroenecker
epsx(1) = 1;
epsy = ones(1,ymodes,'single').*2; % epsilon values for Lambda kroenecker
epsy(1) = 1;
epsz = ones(1,zmodes,'single').*2; % epsilon values for Lambda kroenecker
epsz(1) = 1;

words = 'indices loaded';
disp(words)

%% calculate the k_n^2 and k_n values to be used in the denominator of the algorithm
  % this generates a 3D matrix of values to call that are index based and single precision

knsq=zeros(xmodes,ymodes,zmodes,'single');
for Xm=xindex
   for Ym=yindex
      for Zm=zindex
         knsq(Xm,Ym,Zm)=pi^2*((nx(Xm)./Lx).^2 + (ny(Ym)./Ly).^2 + (nz(Zm)./Lz).^2);
      end
   end
end

kn = j*2.*sqrt(knsq);   % by defining kn outside of the loop, the GPU computaion time is halved.

words = 'kn and knsq calculated';
disp(words)

%% this section generates a 3D meshgrid of calculations to apply to the 3D numerator calculation
  % in the following section

[Nx,X] = meshgrid(nx,xp);
xcos = cos(Nx.*X*pi/Lx).*cos(nx*pi*x0./Lx).*epsx;

[Ny,Y] = meshgrid(ny,yp);
ycos = cos(Ny.*Y*pi/Ly).*cos(ny*pi*y0./Ly).*epsy;

[Nz,Z] = meshgrid(nz,zp);
zcos = cos(Nz.*Z*pi/Lz).*cos(nz*pi*z0./Lz).*epsz;

words = 'calculation meshgrid allocated';
disp(words)

%% this section does stuff slow as molassess, now its PARFOR-ed,
 % takes about 30 min to calculate xyzcos calculates the value of all products of the Psi_0 and Psi
 % values with the Neumann-Kroenecker Lambda (1/(epsx*epsy*epsz)) as well.

   xyzcos=zeros(xmodes,ymodes,zmodes,length(pos));
   parfor Pm=pindex
      disp(Pm)
      temp=xyzcos(:,:,:,Pm);
      for Xm=xindex
         for Ym=yindex
            for Zm=zindex
```

```
                temp(Xm,Ym,Zm,:)=cos(nx(Xm).*xp(Pm)*pi/Lx).*cos(nx(Xm)*pi*x0./Lx).*epsx(Xm)...
                    .*cos(ny(Ym).*yp(Pm)*pi/Ly).*cos(ny(Ym)*pi*y0./Ly).*epsy(Ym)...
                    .*cos(nz(Zm).*zp(Pm)*pi/Lz).*cos(nz(Zm)*pi*z0./Lz).*epsz(Zm);

            end
        end
    end
    xyzcos(:,:,:,Pm)=temp;
end

words = 'xyzcos calculated';
disp(words)

%% gpu computation section:
 % this section multiplies 2D arrays in x-y (sheets stacked in z) 10 at a
 % time to find the spectrum inside the sum. it is then summed across all
 % frequencies to get p(x,y,z) for a given Psi and Psi_0
 % the arrays are stored on the GPU, this doesn't really save a lot of time, but it saves
 % memory on the RAM and CPU power.

gpuDevice(1); % specifies the gpu device in the computer to use for array storage

% pre-allocate zero matrices for speed
press_spec = (complex(zeros(length(pos),length(k),'single')));
PdB_loop = zeros(20,1);

for Pm=pindex  % pindex indicates the number of reciever positions in the calculation

    % storing the xyzcos array on the GPU saves RAM space
    Gxyzcos = gpuArray(complex(xyzcos(:,:,:,Pm)));

    for ks=kindex
        disp(ks)                        % keeps track on command window of the current k
        result = (complex(0));        % preallocate result as complex

        KK = (k(ks)^2-knsq-kn*delta_c(ks)); % this is the time intesive calculation
        Gkk = gpuArray(complex(KK));        % store it on the GPU for calculation speed

        stepz = 10; % dividing 10 sheets of z at a time
        for zm = 1:stepz:length(zindex)
            zmf=zm+(stepz-1);

            % the following function is ultimately the final sum calculation p(x,y,z,k)
            % it pulls values from the GPU to the CPU as the result is stored in the RAM
            % it pulls 10 sheets of values, zm:zmf, at a time to be calculated.
            result = result+sum(Gxyzcos(:,:,zm:zmf)./Gkk(:,:,zm:zmf),'all');

        end

        press_spec(Pm,ks) = result;
        % press_spec(Pm,ks) = gather(result);
        % if we don't clear Gkk and KK the memory will get overloaded
        clear Gkk KK

    end
```

```
    % if we don't clear Gxyzcos the GPU memory gets overloaded
    clear Gxyzcos
    % coefficient to the sum is included here as 'prefix', these values are not saved, merely
    % displayed to give an idea of what the differences between positions look like
    PdB_loop = (20*log10(abs((double((prefix.*sum(press_spec,2)).^2)))./pref));
    disp(PdB_loop)
end
%%
%     Ptot = (prefix.*sum(press_spec,2));   % prefix is a combo of the coefficient variables
%
%     Pxyz = (double(abs((Ptot.^2))));      % sum across all frequencies, converted to a double for save
%                                           % magnitude squared as explained by brian anderson
%     PdB = 20*log10(abs(Pxyz)./pref);      % dB conversion
%
%     spectrum_save = double(spectrum);

words = 'CALCULATIONS COMPLETE';
disp(words)

%% save .txt and .mat files

save NEW_NUM_DATA_UPDATES_CORNER.mat press_spec

% save wall_Ptot_corr_RT60.mat Ptot

words = 'FILES SAVED';
disp(words)
%% alert that code is done
bell = audioread('bell.mp3');
bell = bell';
bell = bell(1,3e4:end);
soundsc(bell,32000)
```

Appendix D

D.1 Introduction

This section contains the MATLAB© script that I wrote for use with the open source package k-Wave©. It is broken into 3 sections, each containing a different script for use calculating specific results using the package. Section D.2 contains the script for a 360˚ array of sources with a vertical array of receivers through the center. Section D.3 contains the script for a 180˚ array of sources with a vertical array of receivers centered at the arc of the sources. This script then shifts the source locations to reduce the aperture and runs in entirety again. Collecting data for the peak focus amplitudes for each source array. Section D.4 contains the script for reproducing the linear summation of source signals versus the simultaneous broadcast of all sources simultaneously. Section D.5 is a brief description of how to properly place your sources using the grid layout created by the kgrid function in k-Wave©.

D.2 MATLAB© Script 1

```
%% TryTryAgain1.m
clc
clear
close all
================================================================================
% This was built upon the example given in the k-Wave library called example_ivp_homogeneous_medium.
% It allows the user to define a line of receivers in a 2D space and record a time waveform created
% by two (or potentially more) sources placed in that space. It is important to note that the
% receiver locations are done with the meter measurement axes, and the source locations are placed
% with the grid point locations. This can lead to slight rounding errors if you are calculating the
% positions using something like the Pythagorean theorem, or polar coordinates.
%
================================================================================

% create the computational grid
Nx = 128;       % number of grid points in the x (row) direction
Ny = 128;       % number of grid points in the y (column) direction
dx = 1e-0;      % grid point spacing in the x direction [m]
dy = 1e-0;      % grid point spacing in the y direction [m]

% this function builds the k-Wave grid axes given the above coordinates
% note: the grid center is Nx./2+1
kgrid = kWaveGrid(Nx, dx, Ny, dy);

% define the properties of the propagation medium
medium.sound_speed = 343;  % [m/s]
medium.density = 1.21;          % [kg/m^3]
medium.BonA = 0.4;              % NONLINEARITY [Thermodynamics, gamma - 1]

mag = [2000 4000 6000 8000 10000 12000];  % [magnitude is in Pascals]
rad = 0.25;  % [radius of sources in meters]

r = 5;                          % [distance from the central sensor in he array]
xs = [1.25 2.75 4 4.85];      % [x positions in meters]
xp1 = xs.*10+(Nx./2 + 1);  % [translate those to grid point]
xp2 = -xs.*10+(Nx./2 + 1); % [reflect to opposite side of axis]
yp1 = round(sqrt(r^2-xs.^2),1).*10 + (Ny./2 + 1); %[y positions in terms of grid points]
yp2 = 129 - yp1;                %[reflect to opposite side of axis]
% yp = 115.*ones(1,4); % for a straight array

sensor_data = zeros(length(mag),121,604);
for m = 1:1%length(mag)
%======== initial ball positions in quadrant IV ================================================

disc_magnitude = mag(m);    % [Pa]
disc_x_pos = xp1(1);            % [grid points [1:128]]
disc_y_pos = yp1(1);            % [grid points [1:128]]
disc_radius = rad;              % [grid points [1:128]]
% below: takes info above and makes a disc with an initial amplitude as specified
disc_1 = disc_magnitude * makeDisc(Nx, Ny, disc_x_pos, disc_y_pos, disc_radius);
```

```
disc_magnitude = mag(m);    % [Pa]
disc_x_pos = xp1(2);        % [grid points [1:128]]
disc_y_pos = yp1(2);        % [grid points [1:128]]
disc_radius = rad;          % [grid points [1:128]]
% below: takes info above and makes a disc with an initial amplitude as specified
disc_2 = disc_magnitude * makeDisc(Nx, Ny, disc_x_pos, disc_y_pos, disc_radius);

disc_magnitude = mag(m);    % [Pa]
disc_x_pos = xp1(3);        % [grid points [1:128]]
disc_y_pos = yp1(3);        % [grid points [1:128]]
disc_radius = rad;          % [grid points [1:128]]
% below: takes info above and makes a disc with an initial amplitude as specified
disc_3 = disc_magnitude * makeDisc(Nx, Ny, disc_x_pos, disc_y_pos, disc_radius);

disc_magnitude = mag(m);    % [Pa]
disc_x_pos = xp1(4);        % [grid points [1:128]]
disc_y_pos = yp1(4);        % [grid points [1:128]]
disc_radius = rad;          % [grid points [1:128]]
% below: takes info above and makes a disc with an initial amplitude as specified
disc_4 = disc_magnitude * makeDisc(Nx, Ny, disc_x_pos, disc_y_pos, disc_radius);

%======== reflected ball positions in quadrant I ================================================

disc_magnitude = mag(m);    % [Pa]
disc_x_pos = xp2(1);        % [grid points [1:128]]
disc_y_pos = yp1(1);        % [grid points [1:128]]
disc_radius = rad;          % [grid points [1:128]]
% below: takes info above and makes a disc with an initial amplitude as specified
disc_5 = disc_magnitude * makeDisc(Nx, Ny, disc_x_pos, disc_y_pos, disc_radius);

disc_magnitude = mag(m);    % [Pa]
disc_x_pos = xp2(2);        % [grid points [1:128]]
disc_y_pos = yp1(2);        % [grid points [1:128]]
disc_radius = rad;          % [grid points [1:128]]
% below: takes info above and makes a disc with an initial amplitude as specified
disc_6 = disc_magnitude * makeDisc(Nx, Ny, disc_x_pos, disc_y_pos, disc_radius);

disc_magnitude = mag(m);    % [Pa]
disc_x_pos = xp2(3);        % [grid points [1:128]]
disc_y_pos = yp1(3);        % [grid points [1:128]]
disc_radius = rad;          % [grid points [1:128]]
% below: takes info above and makes a disc with an initial amplitude as specified
disc_7 = disc_magnitude * makeDisc(Nx, Ny, disc_x_pos, disc_y_pos, disc_radius);

disc_magnitude = mag(m);    % [Pa]
disc_x_pos = xp2(4);        % [grid points [1:128]]
disc_y_pos = yp1(4);        % [grid points [1:128]]
disc_radius = rad;          % [grid points [1:128]]
% below: takes info above and makes a disc with an initial amplitude as specified
disc_8 = disc_magnitude * makeDisc(Nx, Ny, disc_x_pos, disc_y_pos, disc_radius);

%%%%%%%%%%%%%%%%%% disc 9 (center) %%%%%%%%%%%%%%%%%%%%%%%%%%%%%%%%%%%%%%%%%%%%%%%%%%%%%%%%%
disc_magnitude = mag(m);    % [Pa]
disc_x_pos = 65;            % [grid points [1:128]]
disc_y_pos = 115;           % [grid points [1:128]]
```

```
disc_radius = rad;                % [grid points [1:128]]
% below: takes info above and makes a disc with an initial amplitude as specified
disc_9 = disc_magnitude * makeDisc(Nx, Ny, disc_x_pos, disc_y_pos, disc_radius);
%%%%%%%%%%%%%%%%%%%%%%%%%%%%%%%%%%%%%%%%%%%%%%%%%%%%%%%%%%%%%%%%%%%%%%%%%%%%%%%


%======== reflected ball positions in quadrant III ================================================

disc_magnitude = mag(m);    % [Pa]
disc_x_pos = xp1(1);        % [grid points [1:128]]
disc_y_pos = yp2(1);        % [grid points [1:128]]
disc_radius = rad;          % [grid points [1:128]]
% below: takes info above and makes a disc with an initial amplitude as specified
disc_10 = disc_magnitude * makeDisc(Nx, Ny, disc_x_pos, disc_y_pos, disc_radius);

disc_magnitude = mag(m);    % [Pa]
disc_x_pos = xp1(2);        % [grid points [1:128]]
disc_y_pos = yp2(2);        % [grid points [1:128]]
disc_radius = rad;          % [grid points [1:128]]
% below: takes info above and makes a disc with an initial amplitude as specified
disc_11 = disc_magnitude * makeDisc(Nx, Ny, disc_x_pos, disc_y_pos, disc_radius);

disc_magnitude = mag(m);    % [Pa]
disc_x_pos = xp1(3);        % [grid points [1:128]]
disc_y_pos = yp2(3);        % [grid points [1:128]]
disc_radius = rad;          % [grid points [1:128]]
% below: takes info above and makes a disc with an initial amplitude as specified
disc_12 = disc_magnitude * makeDisc(Nx, Ny, disc_x_pos, disc_y_pos, disc_radius);

disc_magnitude = mag(m);    % [Pa]
disc_x_pos = xp1(4);        % [grid points [1:128]]
disc_y_pos = yp2(4);        % [grid points [1:128]]
disc_radius = rad;          % [grid points [1:128]]
% below: takes info above and makes a disc with an initial amplitude as specified
disc_13 = disc_magnitude * makeDisc(Nx, Ny, disc_x_pos, disc_y_pos, disc_radius);


%======== reflected ball positions in quadrant II =================================================

disc_magnitude = mag(m);    % [Pa]
disc_x_pos = xp2(1);        % [grid points [1:128]]
disc_y_pos = yp2(1);        % [grid points [1:128]]
disc_radius = rad;          % [grid points [1:128]]
% below: takes info above and makes a disc with an initial amplitude as specified
disc_14 = disc_magnitude * makeDisc(Nx, Ny, disc_x_pos, disc_y_pos, disc_radius);

disc_magnitude = mag(m);    % [Pa]
disc_x_pos = xp2(2);        % [grid points [1:128]]
disc_y_pos = yp2(2);        % [grid points [1:128]]
disc_radius = rad;          % [grid points [1:128]]
% below: takes info above and makes a disc with an initial amplitude as specified
disc_15 = disc_magnitude * makeDisc(Nx, Ny, disc_x_pos, disc_y_pos, disc_radius);

disc_magnitude = mag(m);    % [Pa]
disc_x_pos = xp2(3);        % [grid points [1:128]]
disc_y_pos = yp2(3);        % [grid points [1:128]]
```

```
disc_radius = rad;                  % [grid points [1:128]]
% below: takes info above and makes a disc with an initial amplitude as specified
disc_16 = disc_magnitude * makeDisc(Nx, Ny, disc_x_pos, disc_y_pos, disc_radius);

disc_magnitude = mag(m);    % [Pa]
disc_x_pos = xp2(4);            % [grid points [1:128]]
disc_y_pos = yp2(4);            % [grid points [1:128]]
disc_radius = rad;                  % [grid points [1:128]]
% below: takes info above and makes a disc with an initial amplitude as specified
disc_17 = disc_magnitude * makeDisc(Nx, Ny, disc_x_pos, disc_y_pos, disc_radius);

%%%%%%%%%%%%%%%%%%% disc 18 (center) %%%%%%%%%%%%%%%%%%%%%%%%%%%%%%%%%%%%%%
disc_magnitude = mag(m);    % [Pa]
disc_x_pos = 65;                  % [grid points [1:128]]
disc_y_pos = 13;                  % [grid points [1:128]]
disc_radius = rad;                  % [grid points [1:128]]
% below: takes info above and makes a disc with an initial amplitude as specified
disc_18 = disc_magnitude * makeDisc(Nx, Ny, disc_x_pos, disc_y_pos, disc_radius);
%%%%%%%%%%%%%%%%%%%%%%%%%%%%%%%%%%%%%%%%%%%%%%%%%%%%%%%%%%%%%%%%%%%%%%%%%%%%%%%%%%

% the sum of the solutions is the final source solution
source.p0 = disc_1 + disc_2 + disc_3 + disc_4 + disc_5 + disc_6 + disc_7 + disc_8 + disc_9 +...
    disc_10 + disc_11 + disc_12 + disc_13 + disc_14 + disc_15 + disc_16 + disc_17 + disc_18;

% define a series of Cartesian points to collect the data. NOTE: these are in decimeters, making hte
% array 6 meters in length in both directions.
x = (-60:60) * dx;                 % [dm]
y = 0 * dy * ones(size(x));     % [dm]
sensor.mask = [x; y];          % [sensor mask creates the array of sensors at the given locations]

% run the simulation and calculate what each sensor see from time 0 to time end
sensor_data(m,:,:) = kspaceFirstOrder2D(kgrid, medium, source, sensor);
end
% plot the initial pressure and sensor distribution, primarily for ensuring the right positions have
% been chosen and the code is working properly, not always needed.
figure;
imagesc(kgrid.y_vec, kgrid.x_vec, source.p0 + cart2grid(kgrid, sensor.mask), [-1, 1]);
colormap(getColorMap);
title('Source and Receiver Array Positions: 360\circ','FontSize',28)
ylabel('x-position [dm]','FontSize',26);
xlabel('y-position [dm]','FontSize',26);
grid on
axis image;

%%
%=================================================================================
% VISUALISATION
%=================================================================================
%% surface plots


for k = 1:6

    Pa(:,:) = sensor_data(k,:,:);

    fig1 = figure;
```

```
    [m,c] = contour(Pa);
    c.LineWidth = 1.5;
    colormap(getColorMap);
    view(90,90)
    title(['18 Sources at ', num2str(mag(k)), ' Pa,',' 360','\circ',' Aperture'])
    ylabel('Sensor Number');
    xlabel('Samples (1143.3 sam/s)');
    colorbar;
    xlim([140 220])
    %ylim([0 61])
    grid off
    %saveas(fig1,['contour_',num2str(k),'.fig'])

    fig2 = figure;
    surf(Pa);
    colormap(getColorMap);
    view(90,90)
    %zlim([-max(abs(sensor_data(30,:))) max(abs(sensor_data(30,:)))])
    shading interp % gets rid of the lines
    title(['18 Sources at ', num2str(mag(k)), ' Pa,',' 360','\circ',' Aperture'])
    ylabel('Sensor Number');
    xlabel('Samples (1143.3 sam/s)');
    colorbar;
    xlim([140 220])
    %ylim([0 61])
    grid on
    %saveas(fig2,['surface_',num2str(k),'.fig'])
end
%% quad for dissertation
figq = figure;
t = tiledlayout(2,2)
for k = 1:4;

Pa(:,:) = sensor_data(k,:,:);

h(k) = nexttile(t)
surf(Pa);
    colormap(getColorMap);
    view(90,90)
    %zlim([-max(abs(sensor_data(30,:))) max(abs(sensor_data(30,:)))])
    shading interp % gets rid of the lines
    title(['18 Sources at ', num2str(mag(k)), ' Pa,',' 360','\circ',' Aperture'])
    ylabel('Sensor Number');
    xlabel('Samples (1143.3 sam/s)');
    colorbar;
    xlim([140 220])
    %ylim([0 61])
    grid on
%saveas(figq,'contour_quad.fig')
end
set(h,'Colormap',jet,'CLim',[-6000 6000])
cbh = colorbar(h(end));
cbh.Layout.Tile = 'east';
cbTitleHandle = get(cbh,'Title');
titleString = {'Pressure','(Pa)'};
set(cbTitleHandle ,'String',titleString);
```

```
%% peak plots

[a,b,c] = size(sensor_data);
time = 874.6356e-9.*(0:(c-1)).*100000;
cs = 61;

% angle_deg = zeros(1,length(xs));
% for ii = 1:a
%     angle_deg(1,ii) = abs(2.*atan(xs(ii)./round(sqrt(r.^2-xs(ii).^2),1))*180./pi);
% end

% plot the peaks of the central sensor
figure
for j = 1:a
   pa(:,:) = sensor_data(j,cs,:);

   hold on
   plot(interp(time,10),interp(pa,10))
   xlabel('Time (ms)')
   ylabel('Pressure (Pa)')
   %xlim([0.1 0.3])
   hold off
end
legend([num2str(mag(1)),' Pa'],[num2str(mag(2)),' Pa'],[num2str(mag(3)),' Pa'],...
   [num2str(mag(4)),' Pa'],[num2str(mag(5)),' Pa'],[num2str(mag(6)),' Pa'])

% plot the SCALED peaks of the central sensor

scl = [6 3 2 3/2 6/5 1];
figure
for j = 1:a
   pa(:,:) = sensor_data(j,cs,:);

   hold on
   plot(interp(time,4),interp(pa*scl(j),4))
   xlabel('Time (ms)')
   ylabel('Pressure (Pa)')
   hold off
end
title('18 Sources, 360 deg Aperture')
xlim([13 16])
legend([num2str(mag(1)),' Pa'],[num2str(mag(2)),' Pa'],[num2str(mag(3)),' Pa'],...
   [num2str(mag(4)),' Pa'],[num2str(mag(5)),' Pa'],[num2str(mag(6)),' Pa'])
grid on


%% fft of peak wave : each time step is 8.7464e-4 s
clear fft_pa Pa P1 P2
fs = 1.1433e04;    % calculated from time steps and number of samples
pref = 20e-6;

%fft_pa = zeros(6,370); P1 = zeros(6,370); P2 = zeros(6,370);
for k = 1:6

Pa(:,:) = sensor_data(k,:,:);
```

```
fft_pa(k,:) = fft(Pa(cs,:));
L = length(fft_pa(k,:))-1;
freqs = fs*(0:(L/2))/L;
P2(k,:) = abs(fft_pa(k,:)/L);
P1(k,:) = P2(k,1:floor(L/2+1));
P1(k,2:end-1) = 2*P1(k,2:end-1);
end

%%
fig5 = figure;
plot(freqs,P1(1,:).*scl(1),freqs,P1(2,:).*scl(2),freqs,P1(3,:).*scl(3),freqs,P1(4,:).*scl(4),...
    freqs,P1(5,:).*scl(5),freqs,P1(6,:))
title('FFT of {\itN}-wave Focus')
xlabel('Frequency (Hz)')
ylabel('Pressure (Pa)')
legend([num2str(mag(1)),' Pa'],[num2str(mag(2)),' Pa'],[num2str(mag(3)),' Pa'],[num2str(mag(4)),' Pa'],...
    [num2str(mag(5)),' Pa'],[num2str(mag(6)),' Pa']);
grid on
%saveas(fig5,'fft.fig')

%%
fig6 = figure;
plot(freqs,20*log10(abs(P1(1,:).*scl(1))./pref),freqs,20*log10(abs(P1(2,:).*scl(2))./pref),...
    freqs,20*log10(abs(P1(3,:).*scl(3))./pref),freqs,20*log10(abs(P1(4,:).*scl(4))./pref),...
    freqs,20*log10(abs(P1(5,:).*scl(5))./pref),freqs,20*log10(abs(P1(6,:).*scl(6))./pref))
title('Scaled FFT of {\itN}-wave Focus')
xlabel('Frequency (Hz)')
ylabel('Sound Pressure Level (ref 20\muPa)')
legend([num2str(mag(1)),' Pa'],[num2str(mag(2)),' Pa'],[num2str(mag(3)),' Pa'],[num2str(mag(4)),' Pa'],...
    [num2str(mag(5)),' Pa'],[num2str(mag(6)),' Pa']);
grid on
%saveas(fig6,'scaled_fft.fig')
```

D.3 MATLAB© Script 2

```
%% TryTryAgain4.m
clc
clear
close all
% ================================================================================
% This was built upon the example given in the k-Wave library called example_ivp_homogeneous_medium.
% It allows the user to define a line of receivers in a 2D space and record a time waveform created
% by two (or potentially more) sources placed in that space. It is important to note that the
% receiver locations are done with the meter measurement axes, and the source locations are placed
% with the grid point locations. This can lead to slight rounding errors if you are calculating the
% positions using something like the pythagorean theorem, or polar coordinates.
% ================================================================================

% create the computational grid
Nx = 128;        % number of grid points in the x (row) direction
Ny = 128;        % number of grid points in the y (column) direction
dx = 1e-0;       % grid point spacing in the x direction [m]
dy = 1e-0;       % grid point spacing in the y direction [m]

% this function builds the k-Wave grid axes given the above coordinates
% note: the grid center is Nx./2+1
kgrid = kWaveGrid(Nx, dx, Ny, dy);

% define the properties of the propagation medium
medium.sound_speed = 343;  % [m/s]
medium.density = 1.21;     % [kg/m^3]
medium.BonA = 0.4;         % [Thermodynamics, gamma - 1]

mag = 12000;  % [magnitude is in Pascals]
rad = 0.25;        % [radius of sources in meters]

r = 5;                  % [distance from the central sensor in he array]
xs = [[1 1.8 2.75 3.6 4.15 4.65 4.95 5];…
1:4.99/9:4.99;0.8:5/9:5;0.8:4.1/9:4;0.6:3/9:3;0.4:2.5/9:2.5;0.4:2/9:2;0.2:1.5/9:1.5];  % [x positions in meters]
xp1 = xs.*10+(Nx./2 + 1);  % [translate those to grid point]
xp2 = -xs.*10+(Nx./2 + 1); % [reflect to opposite side of axis for 2nd source]
yp = round(sqrt(r^2-xs.^2),1).*10 + (Ny./2 + 1); % [y positions in terms of grid points]
% yp = 115.*ones(1,length(xs)); % for a straight array

[cc,dd] = size(xs);

sensor_data = zeros(length(mag),121,604);
for m = 1:cc
%======== initial ball positions in quadrant IV ================================================

disc_magnitude = mag;      % [Pa]
disc_x_pos = xp1(m,1);     % [grid points [1:128]]
disc_y_pos = yp(m,1);      % [grid points [1:128]]
disc_radius = rad;         % [grid points [1:128]]
% below: takes info above and makes a disc with an initial amplitude as specified
disc_1 = disc_magnitude * makeDisc(Nx, Ny, disc_x_pos, disc_y_pos, disc_radius);

disc_magnitude = mag;      % [Pa]
```

```
disc_x_pos = xp1(m,2);     % [grid points [1:128]]
disc_y_pos = yp(m,2);      % [grid points [1:128]]
disc_radius = rad;         % [grid points [1:128]]
% below: takes info above and makes a disc with an initial amplitude as specified
disc_2 = disc_magnitude * makeDisc(Nx, Ny, disc_x_pos, disc_y_pos, disc_radius);

disc_magnitude = mag;      % [Pa]
disc_x_pos = xp1(m,3);     % [grid points [1:128]]
disc_y_pos = yp(m,3);      % [grid points [1:128]]
disc_radius = rad;         % [grid points [1:128]]
% below: takes info above and makes a disc with an initial amplitude as specified
disc_3 = disc_magnitude * makeDisc(Nx, Ny, disc_x_pos, disc_y_pos, disc_radius);

disc_magnitude = mag;      % [Pa]
disc_x_pos = xp1(m,4);     % [grid points [1:128]]
disc_y_pos = yp(m,4);      % [grid points [1:128]]
disc_radius = rad;         % [grid points [1:128]]
% below: takes info above and makes a disc with an initial amplitude as specified
disc_4 = disc_magnitude * makeDisc(Nx, Ny, disc_x_pos, disc_y_pos, disc_radius);

disc_magnitude = mag;      % [Pa]
disc_x_pos = xp1(m,5);     % [grid points [1:128]]
disc_y_pos = yp(m,5);      % [grid points [1:128]]
disc_radius = rad;         % [grid points [1:128]]
% below: takes info above and makes a disc with an initial amplitude as specified
disc_5 = disc_magnitude * makeDisc(Nx, Ny, disc_x_pos, disc_y_pos, disc_radius);

disc_magnitude = mag;      % [Pa]
disc_x_pos = xp1(m,6);     % [grid points [1:128]]
disc_y_pos = yp(m,6);      % [grid points [1:128]]
disc_radius = rad;         % [grid points [1:128]]
% below: takes info above and makes a disc with an initial amplitude as specified
disc_6 = disc_magnitude * makeDisc(Nx, Ny, disc_x_pos, disc_y_pos, disc_radius);

disc_magnitude = mag;      % [Pa]
disc_x_pos = xp1(m,7);     % [grid points [1:128]]
disc_y_pos = yp(m,7);      % [grid points [1:128]]
disc_radius = rad;         % [grid points [1:128]]
% below: takes info above and makes a disc with an initial amplitude as specified
disc_7 = disc_magnitude * makeDisc(Nx, Ny, disc_x_pos, disc_y_pos, disc_radius);

disc_magnitude = mag;      % [Pa]
disc_x_pos = xp1(m,8);     % [grid points [1:128]]
disc_y_pos = yp(m,8);      % [grid points [1:128]]
disc_radius = rad;         % [grid points [1:128]]
% below: takes info above and makes a disc with an initial amplitude as specified
disc_8 = disc_magnitude * makeDisc(Nx, Ny, disc_x_pos, disc_y_pos, disc_radius);

%======== reflected ball positions in quadrant I ===========================================

disc_magnitude = mag;      % [Pa]
disc_x_pos = xp2(m,1);     % [grid points [1:128]]
disc_y_pos = yp(m,1);      % [grid points [1:128]]
disc_radius = rad;         % [grid points [1:128]]
% below: takes info above and makes a disc with an initial amplitude as specified
disc_9 = disc_magnitude * makeDisc(Nx, Ny, disc_x_pos, disc_y_pos, disc_radius);
```

```
disc_magnitude = mag;      % [Pa]
disc_x_pos = xp2(m,2);     % [grid points [1:128]]
disc_y_pos = yp(m,2);      % [grid points [1:128]]
disc_radius = rad;         % [grid points [1:128]]
% below: takes info above and makes a disc with an initial amplitude as specified
disc_10 = disc_magnitude * makeDisc(Nx, Ny, disc_x_pos, disc_y_pos, disc_radius);

disc_magnitude = mag;      % [Pa]
disc_x_pos = xp2(m,3);     % [grid points [1:128]]
disc_y_pos = yp(m,3);      % [grid points [1:128]]
disc_radius = rad;         % [grid points [1:128]]
% below: takes info above and makes a disc with an initial amplitude as specified
disc_11 = disc_magnitude * makeDisc(Nx, Ny, disc_x_pos, disc_y_pos, disc_radius);

disc_magnitude = mag;      % [Pa]
disc_x_pos = xp2(m,4);     % [grid points [1:128]]
disc_y_pos = yp(m,4);      % [grid points [1:128]]
disc_radius = rad;         % [grid points [1:128]]
% below: takes info above and makes a disc with an initial amplitude as specified
disc_12 = disc_magnitude * makeDisc(Nx, Ny, disc_x_pos, disc_y_pos, disc_radius);

disc_magnitude = mag;      % [Pa]
disc_x_pos = xp2(m,5);     % [grid points [1:128]]
disc_y_pos = yp(m,5);      % [grid points [1:128]]
disc_radius = rad;         % [grid points [1:128]]
% below: takes info above and makes a disc with an initial amplitude as specified
disc_13 = disc_magnitude * makeDisc(Nx, Ny, disc_x_pos, disc_y_pos, disc_radius);

disc_magnitude = mag;      % [Pa]
disc_x_pos = xp2(m,6);     % [grid points [1:128]]
disc_y_pos = yp(m,6);      % [grid points [1:128]]
disc_radius = rad;         % [grid points [1:128]]
% below: takes info above and makes a disc with an initial amplitude as specified
disc_14 = disc_magnitude * makeDisc(Nx, Ny, disc_x_pos, disc_y_pos, disc_radius);

disc_magnitude = mag;      % [Pa]
disc_x_pos = xp2(m,7);     % [grid points [1:128]]
disc_y_pos = yp(m,7);      % [grid points [1:128]]
disc_radius = rad;         % [grid points [1:128]]
% below: takes info above and makes a disc with an initial amplitude as specified
disc_15 = disc_magnitude * makeDisc(Nx, Ny, disc_x_pos, disc_y_pos, disc_radius);

disc_magnitude = mag;      % [Pa]
disc_x_pos = xp2(m,8);     % [grid points [1:128]]
disc_y_pos = yp(m,8);      % [grid points [1:128]]
disc_radius = rad;         % [grid points [1:128]]
% below: takes info above and makes a disc with an initial amplitude as specified
disc_16 = disc_magnitude * makeDisc(Nx, Ny, disc_x_pos, disc_y_pos, disc_radius);

%%%%%%%%%%%%%%%%%%%% disc 9 (center) %%%%%%%%%%%%%%%%%%%%%%%%%%%%%%%%%%%%
disc_magnitude = mag;      % [Pa]
disc_x_pos = 65;           % [grid points [1:128]]
disc_y_pos = 115;          % [grid points [1:128]]
disc_radius = rad;         % [grid points [1:128]]
% below: takes info above and makes a disc with an initial amplitude as specified
```

```
disc_17 = disc_magnitude * makeDisc(Nx, Ny, disc_x_pos, disc_y_pos, disc_radius);
%%%%%%%%%%%%%%%%%%%%%%%%%%%%%%%%%%%%%%%%%%%%%%%%%%%%%%%%%%%%%%%%%%%%%%%%%%%%%%%

% the sum of the two solutions is the final source solution
source.p0 = disc_1 + disc_2 + disc_3 + disc_4 + disc_5 + disc_6 + disc_7 + disc_8 + disc_9 +...
    disc_10 + disc_11 + disc_12 + disc_13 + disc_14 + disc_15 + disc_16 + disc_17;

% define a series of Cartesian points to collect the data. NOTE: these are in decimeters, making hte
% array 6 meters in length in both directions.
x = (-60:60) * dx;                  % [dm]
y = 0 * dy * ones(size(x));     % [dm]
sensor.mask = [x; y];             % [sensor mask creates the array of sensors at the given locations]

% run the simulation and calculate what each sensor see from time 0 to time end
sensor_data(m,:,:) = kspaceFirstOrder2D(kgrid, medium, source, sensor);

% plot the initial pressure and sensor distribution, primarily for ensuring the right positions have
% been chosen and the code is working properly, not always needed.
figure;
imagesc(kgrid.y_vec, kgrid.x_vec, source.p0 + cart2grid(kgrid, sensor.mask), [-1, 1]);
colormap(getColorMap);
ylabel('x-position [m]');
xlabel('y-position [dm]');
grid on
axis image;
end

angle_deg = zeros(1,cc);
for ii = 1:cc
    angle_deg(1,ii) = abs(2.*atan(xs(ii,8)./round(sqrt(r.^2-xs(ii,8).^2),1))*180./pi);
end
%%
% =========================================================================
% VISUALISATION
% =========================================================================
%% surface plots

for k = 1:cc

    Pa(:,:) = sensor_data(k,:,:);

    fig1 = figure;
    [m,c] = contour(Pa);
    c.LineWidth = 1.5;
    colormap(getColorMap);
    view(90,90)
    title(['18 Sources at ', num2str(mag), ' Pa, ',num2str(round(angle_deg(k))),'\circ',' Aperture'])
    ylabel('Sensor Number');
    xlabel('Samples (1143.3 sam/s)');
    colorbar;
    xlim([140 220])
    %ylim([0 61])
    grid off
    %saveas(fig1,['contour_',num2str(k),'.fig'])

    fig2 = figure;
```

```
    surf(Pa);
    colormap(getColorMap);
    view(90,90)
    %zlim([-max(abs(sensor_data(30,:))) max(abs(sensor_data(30,:)))])
    shading interp % gets rid of the lines
    title(['18 Sources at ', num2str(mag), ' Pa, ',num2str(round(angle_deg(k))),'\circ',' Aperture'])
    ylabel('Sensor Number');
    xlabel('Samples (1143.3 sam/s)');
    colorbar;
    xlim([140 220])
    %ylim([0 61])
    grid on
    %saveas(fig2,['surface_',num2str(k),'.fig'])
end
%% quad for dissertation
% figq = figure;
% t = tiledlayout(2,2)
% for k = 1:cc
%
% Pa(:,:) = sensor_data(k,:,:);
%
% h(k) = nexttile(t)
% surf(Pa);
%     colormap(getColorMap);
%     view(90,90)
%     %zlim([-max(abs(sensor_data(30,:))) max(abs(sensor_data(30,:)))])
%     shading interp % gets rid of the lines
%     title([num2str(angle_deg(k)),'\circ',' Aperture'])
%     ylabel('Sensor Number');
%     xlabel('Samples (1143.3 sam/s)');
%     colorbar;
%     xlim([140 220])
%     %ylim([0 61])
%     grid on
% %saveas(figq,'contour_quad.fig')
% end
% set(h,'Colormap',jet,'CLim',[-6000 6000])
% cbh = colorbar(h(end));
% cbh.Layout.Tile = 'east';
% cbTitleHandle = get(cbh,'Title');
% titleString = {'Pressure','(Pa)'};
% set(cbTitleHandle ,'String',titleString);

%% peak plots
[a,b,c] = size(sensor_data);
time = 874.6356e-9.*(0:(c-1)).*100000;
cs = 61;


% plot the peaks of the central sensor
figure
for j = 1:5
    pa(:,:) = sensor_data(j,cs,:);

    hold on
    plot(interp(time,10),interp(pa,10),'LineWidth',3)
```

```
    title('Peak Focus Pressure of Central Receiver','FontSize',28)
    xlabel('Time (ms)','FontSize',26)
    ylabel('Pressure (Pa)','FontSize',26)
    xlim([13.5 14.8])
    hold off
end
legend([num2str(round(angle_deg(1))),'\circ'],[num2str(round(angle_deg(2))),'\circ'],[num2str(round(angle_deg(3)))
,'\circ'],...

[num2str(round(angle_deg(4))),'\circ'],[num2str(round(angle_deg(5))),'\circ'])%,[num2str(round(angle_deg(6))),'\cir
c'],...
    %[num2str(round(angle_deg(7))),'\circ'],[num2str(round(angle_deg(8))),'\circ'])
grid on
%% plot the angles vs NLpk/Lpk
angles = 1:180;
NLpeaks = zeros(1,cc);
for jj = 1:cc
    NLpeaks(1,jj) = max(sensor_data(jj,cs,:));
end

Lpeaks = [10228 10139.3 10191.4 10355.3 9868.14 9270.42 8382.2 5966.02]; % gathered from TryTryAgain2_0
through 2_7

rat1 = NLpeaks(1,8)/Lpeaks(1,8);
rat2 = NLpeaks(1,7)/Lpeaks(1,7);
rat3 = NLpeaks(1,6)/Lpeaks(1,6);
rat4 = NLpeaks(1,5)/Lpeaks(1,5);
rat5 = NLpeaks(1,4)/Lpeaks(1,4);
rat6 = NLpeaks(1,3)/Lpeaks(1,3);
rat7 = NLpeaks(1,2)/Lpeaks(1,2);
rat8 = NLpeaks(1,1)/Lpeaks(1,1);
rat9 = 11287.9/10551.4; % these numbers found with TryTryAgain1

deg = [32 46 56 73 106 140 155 180 360];
rats = [rat1 rat2 rat3 rat4 rat5 rat6 rat7 rat8 rat9];

figure
plot(deg,rats,'-ob','LineWidth',3,'MarkerSize',8)
% plot(32,rat1,'X',46,rat2,'X',56,rat3,'X',73,rat4,'X',103,rat5,'X',140,rat6,'X',...
%     155,rat7,'X',180,rat8,'X',360,rat9,'X','LineWidth',12)
title('Nonlinear Increase Ratio vs. Angle','FontSize',28)
xlabel('Angle (deg)','FontSize',26)
ylabel('NL/L pk Amplitude','FontSize',26)
xlim([0 400])
%
legend([num2str(round(angle_deg(7))),'\circ'],[num2str(round(angle_deg(6))),'\circ'],[num2str(round(angle_deg(5)))
,'\circ'],...
%
[num2str(round(angle_deg(4))),'\circ'],[num2str(round(angle_deg(3))),'\circ'],[num2str(round(angle_deg(2))),'\circ'],
...
%     [num2str(round(angle_deg(1))),'\circ'],'360\circ','FontSize',26,'Location','eastoutside')
grid on

%% plot the angles vs the time of the peaks

ta = [14.0967 14.0339 14.0492 14.0172 14.0816 14.1046 14.1492 14.2177 14.2566];
```

```
figure
plot(interp(deg,1),interp(ta,1),'-ob','LineWidth',3,'MarkerSize',8)
% plot(180,14.2177,'X',140,14.1492,'X',103,14.0816,'X',73,14.0172,'X',56,14.0492,'X',46,14.0339,'X',...
%     32,14.0967,'X','LineWidth',12)
%
legend([num2str(round(angle_deg(1))),'\circ'],[num2str(round(angle_deg(2))),'\circ'],[num2str(round(angle_deg(3)))
,'\circ'],...
%
[num2str(round(angle_deg(4))),'\circ'],[num2str(round(angle_deg(5))),'\circ'],[num2str(round(angle_deg(6))),'\circ'],
...
%     [num2str(round(angle_deg(7))),'\circ'],'360\circ','FontSize',26,'Location','eastoutside')
title('Nonlinear Peak Time of Arival vs. Angle','FontSize',28)
xlabel('Angle (deg)','FontSize',26)
ylabel('Time (ms)','FontSize',26)
xlim([0 400])
grid on
%% fft of peak wave : each time step is 8.7464e-4 s
clear fft_pa Pa P1 P2
fs = 1.1433e04;    % calculated from time steps and number of samples
pref = 20e-6;

%fft_pa = zeros(6,370); P1 = zeros(6,370); P2 = zeros(6,370);
for k = 1:cc

Pa(:,:) = sensor_data(k,:,:);

fft_pa(k,:) = fft(Pa(cs,:));
L = length(fft_pa(k,:))-1;
freqs = fs*(0:(L/2))/L;
P2(k,:) = abs(fft_pa(k,:)/L);
P1(k,:) = P2(k,1:floor(L/2+1));
P1(k,2:end-1) = 2*P1(k,2:end-1);
end

%%
fig5 = figure;
plot(freqs,P1(1,:),freqs,P1(2,:),freqs,P1(3,:),freqs,P1(4,:),freqs,P1(5,:),freqs,P1(6,:),freqs,P1(7,:))
title('FFT of Central Receiver')
xlabel('Frequency (Hz)')
ylabel('Pressure (Pa)')
legend([num2str(round(angle_deg(1))),'\circ'],[num2str(round(angle_deg(2))),'\circ'],[num2str(round(angle_deg(3)))
,'\circ'],...

[num2str(round(angle_deg(4))),'\circ'],[num2str(round(angle_deg(5))),'\circ'],[num2str(round(angle_deg(6))),'\circ'],
...
   [num2str(round(angle_deg(7))),'\circ'])
grid on
%saveas(fig5,'fft.fig')


%% take derivative for steepness estimate

for jk = 1:cc
   csdiff(jk,:) = diff(sensor_data(jk,cs,:));
%     hold on
```

```
%     plot(interp(time(1:end-1),10),interp(csdiff(jk,:),10))
%     hold off
    maxdiff(1,jk) = max(csdiff(jk,:));
end
xlim([13 16])

figure
plot(deg(1,1:8),maxdiff,'-ob','LineWidth',3,'MarkerSize',8)
title('Maximum Value of Derivative vs. Angle','FontSize',28)
xlabel('Angle (deg)','FontSize',26)
ylabel('Maximum Derivative Value (Pa/ms)','FontSize',26)
xlim([20 200])
grid on
```

D.4 MATLAB© Script 3

```
%% KSFOD_Sum_vs_Sim_experiment.m
%% This code recreates the linear summation versus simultaneous acoustic mixing experiment performed
% by Patchett and Anderson (2022).

%**** make the source size large to avoid having the surface of the wave have such high velocity
% that it impacts the wave as it travels out causing ringing and weird stuff at the peak, Dr. A
% confirms that this is a possible issue.****

%            1 Pa =  93.9794 dB
%          10 Pa = 113.9794 dB
%        100 Pa = 133.9794 dB
%     1,000 Pa = 153.9794 dB
%   10,000 Pa = 173.9794 dB
% 100,000 Pa = 193.9794 dB

clc
clear
close all
%set(0,'DefaultFigureVisible','off') % shuts of the figure output for the loop

%% create grid and define properties of medium

% create the computational grid
Nx = 128;       % number of grid points in the x direction
Ny = 128;       % number of grid points in the y direction
Nz = 128;       % number of grid points in the z direction
dx = 0.5;       % grid point spacing in the x direction [m]
dy = 0.5;       % grid point spacing in the y direction [m]
dz = 0.5;       % grid point spacing in the z direction [m]
kgrid = kWaveGrid(Nx, dx, Ny, dy, Nz, dz);

% define the properties of the propagation medium
% medium.sound_speed = 343 * ones(Nx, Ny, Nz);    % [m/s] for air
% medium.sound_speed(1:Nx/2, :, :) = 343;         % [m/s] for air
medium.sound_speed = 343 * ones(Nx, Ny, Nz);      % [m/s] for water
medium.sound_speed(1:Nx/2, :, :) = 343;           % [m/s] for water
% medium.density = 1.21 * ones(Nx, Ny, Nz);       % [kg/m^3] for air
% medium.density(:, Ny/4:end, :) = 1.21;          % [kg/m^3] for air
medium.density = 1.21 * ones(Nx, Ny, Nz);         % [kg/m^3] for water
medium.density(:, Ny/4:end, :) = 1.21;            % [kg/m^3] for water
medium.BonA = 0.4;                          % B/A for diatomic gas
% medium.BonA = 4.8;                            % B/A for water from LANL paper - Sturtevant

%% define the initial pressure distributions for the SUMMATION par tof the model
%close all
%mag = [1e0 1e1 1e2 1e3 1e4 1e5];
mag = 25e3; % mag at 50 kPa

rad = [4 4 4]; % 4 seems to be the best radius for this spacing/amplitude

xp12 = [40,43.75,43.75];
yp12 = [-56.4575,51.4575,45.0044];
```

```
check12 = sqrt((128-abs(xp12(1)))^2+(128-abs(yp12(1)))^2);
check22 = sqrt((128-abs(xp12(2)))^2+(128-abs(yp12(2)))^2);

xp34 = [56.4575,49.75,49.75];
yp34 = [-40,48.3057,45.0044];

check34 = sqrt((128-abs(xp34(1)))^2+(128-abs(yp34(1)))^2);
check44 = sqrt((128-abs(xp34(2)))^2+(128-abs(yp34(2)))^2);

xp56 = [-56.4575,53.75,53.75];
yp56 = [40,46.4062,45.0044];

xp78 = [-40,59.75,59.75];
yp78 = [56.4575,45.0044,45.0044];

flag = 2;  % for switching orientations of sources 1 = CIRCLE, 2 = CURVE, 3 = FLAT

sensor_data = zeros(9,61,740); % preallocate for speed
%%
% create initial pressure distribution using makeBall
ball1_magnitude = mag;       % [Pa]
ball1_x_pos = -xp12(flag);   % [grid points]
ball1_y_pos = yp12(flag);    % [grid points]
ball1_z_pos = 0;             % [grid points]
ball1_radius = rad(flag);    % [grid points]
ball_1 = ball1_magnitude * makeBall(Nx, Ny, Nz, ball1_x_pos, ball1_y_pos, ball1_z_pos, ball1_radius);
source.p0 = ball_1;
y_line = [0 0 0];
x = (-30:1:30) * dx;                    % [m]
y = y_line(flag) * dy * ones(size(x));    % [m]
z = zeros(1,length(x));                  % [m]
sensor.mask = [x; y; z];

% input arguments
input_args = {'PlotPML', true,'DataCast', 'single', 'CartInterp', 'nearest'};

% run the simulation, FIRST ORDER
sensor_data(1,:,:) = kspaceFirstOrder3D(kgrid, medium, source, sensor, input_args{:});

Pa1(:,:) = sensor_data(1,:,:);
figure;
surf(Pa1);
colormap(getColorMap);
view(90,90)
%zlim([-max(abs(sensor_data(30,:))) max(abs(sensor_data(30,:)))])
shading interp % gets rid of the lines
title(['Source 1 at ', num2str(mag), ' Pa, Arc Array'])
ylabel('Sensor Number');
xlabel('Samples (1143.3 sam/s)');
colorbar;
xlim([0 740])
ylim([0 61])
grid on

%%%%%%%%%%%%%%%%%%%%%%%%%%%%%%%%%%%%%%%%%%%%%%%%%%%%%%%%%%%%%%%%%%%%%%%%
```

```
ball2_magnitude = mag;      % [Pa]
ball2_x_pos = xp12(flag);   % [grid points]
ball2_y_pos = yp12(flag);   % [grid points]
ball2_z_pos = 0;            % [grid points]
ball2_radius = rad(flag);   % [grid points]
ball_2 = ball2_magnitude * makeBall(Nx, Ny, Nz, ball2_x_pos, ball2_y_pos, ball2_z_pos, ball2_radius);
source.p0 = ball_2;
y_line = [0 0 0];
x = (-30:1:30) * dx;                    % [m]
y = y_line(flag) * dy * ones(size(x));  % [m]
z = zeros(1,length(x));                 % [m]
sensor.mask = [x; y; z];

% input arguments
input_args = {'PlotPML', true,'DataCast', 'single', 'CartInterp', 'nearest'};

% run the simulation, FIRST ORDER
sensor_data(2,:,:) = kspaceFirstOrder3D(kgrid, medium, source, sensor, input_args{:});

Pa2(:,:) = sensor_data(2,:,:);
figure;
surf(Pa2);
colormap(getColorMap);
view(90,90)
%zlim([-max(abs(sensor_data(30,:))) max(abs(sensor_data(30,:)))])
shading interp % gets rid of the lines
title(['Source 2 at ', num2str(mag), ' Pa, Arc Array'])
ylabel('Sensor Number');
xlabel('Samples (1143.3 sam/s)');
colorbar;
xlim([0 740])
ylim([0 61])
grid on

%%%%%%%%%%%%%%%%%%%%%%%%%%%%%%%%%%%%%%%%%%%%%%%%%%%%%%%%%%%%%%%%%%%%%%%%%%%%%%%

ball3_magnitude = mag;      % [Pa]
ball3_x_pos = -xp34(flag);  % [grid points]
ball3_y_pos = yp34(flag);   % [grid points]
ball3_z_pos = 0;            % [grid points]
ball3_radius = rad(flag);   % [grid points]
ball_3 = ball3_magnitude * makeBall(Nx, Ny, Nz, ball3_x_pos, ball3_y_pos, ball3_z_pos, ball3_radius);
source.p0 = ball_3;
y_line = [0 0 0];
x = (-30:1:30) * dx;                    % [m]
y = y_line(flag) * dy * ones(size(x));  % [m]
z = zeros(1,length(x));                 % [m]
sensor.mask = [x; y; z];

% input arguments
input_args = {'PlotPML', true,'DataCast', 'single', 'CartInterp', 'nearest'};

% run the simulation, FIRST ORDER
sensor_data(3,:,:) = kspaceFirstOrder3D(kgrid, medium, source, sensor, input_args{:});

Pa3(:,:) = sensor_data(3,:,:);
```

```
figure;
surf(Pa3);
colormap(getColorMap);
view(90,90)
%zlim([-max(abs(sensor_data(30,:))) max(abs(sensor_data(30,:)))])
shading interp % gets rid of the lines
title(['Source 3 at ', num2str(mag), ' Pa, Arc Array'])
ylabel('Sensor Number');
xlabel('Samples (1143.3 sam/s)');
colorbar;
xlim([0 740])
ylim([0 61])
grid on

%%%%%%%%%%%%%%%%%%%%%%%%%%%%%%%%%%%%%%%%%%%%%%%%%%%%%%%%%%%%%%%%%%%%%%%%%%%%%%%

ball4_magnitude = mag;      % [Pa]
ball4_x_pos = xp34(flag);   % [grid points]
ball4_y_pos = yp34(flag);   % [grid points]
ball4_z_pos = 0;            % [grid points]
ball4_radius = rad(flag);   % [grid points]
ball_4 = ball4_magnitude * makeBall(Nx, Ny, Nz, ball4_x_pos, ball4_y_pos, ball4_z_pos, ball4_radius);
source.p0 = ball_4;
y_line = [0 0 0];
x = (-30:1:30) * dx;                    % [m]
y = y_line(flag) * dy * ones(size(x));  % [m]
z = zeros(1,length(x));                 % [m]
sensor.mask = [x; y; z];

% input arguments
input_args = {'PlotPML', true,'DataCast', 'single', 'CartInterp', 'nearest'};

% run the simulation, FIRST ORDER
sensor_data(4,:,:) = kspaceFirstOrder3D(kgrid, medium, source, sensor, input_args{:});

Pa4(:,:) = sensor_data(4,:,:);
figure;
surf(Pa4);
colormap(getColorMap);
view(90,90)
%zlim([-max(abs(sensor_data(30,:))) max(abs(sensor_data(30,:)))])
shading interp % gets rid of the lines
title(['Source 4 at ', num2str(mag), ' Pa, Arc Array'])
ylabel('Sensor Number');
xlabel('Samples (1143.3 sam/s)');
colorbar;
xlim([0 740])
ylim([0 61])
grid on

%%%%%%%%%%%%%%%%%%%%%%%%%%%%%%%%%%%%%%%%%%%%%%%%%%%%%%%%%%%%%%%%%%%%%%%%%%%%%%%

ball5_magnitude = mag;      % [Pa]
ball5_x_pos = -xp56(flag);  % [grid points]
ball5_y_pos = yp56(flag);   % [grid points]
ball5_z_pos = 0;            % [grid points]
```

```
ball5_radius = rad(flag);    % [grid points]
ball_5 = ball5_magnitude * makeBall(Nx, Ny, Nz, ball5_x_pos, ball5_y_pos, ball5_z_pos, ball5_radius);
source.p0 = ball_5;
y_line = [0 0 0];
x = (-30:1:30) * dx;                    % [m]
y = y_line(flag) * dy * ones(size(x));    % [m]
z = zeros(1,length(x));                 % [m]
sensor.mask = [x; y; z];

% input arguments
input_args = {'PlotPML', true,'DataCast', 'single', 'CartInterp', 'nearest'};

% run the simulation, FIRST ORDER
sensor_data(5,:,:) = kspaceFirstOrder3D(kgrid, medium, source, sensor, input_args{:});

Pa5(:,:) = sensor_data(5,:,:);
figure;
surf(Pa5);
colormap(getColorMap);
view(90,90)
%zlim([-max(abs(sensor_data(30,:))) max(abs(sensor_data(30,:)))])
shading interp % gets rid of the lines
title(['Source 5 at ', num2str(mag), ' Pa, Arc Array'])
ylabel('Sensor Number');
xlabel('Samples (1143.3 sam/s)');
colorbar;
xlim([0 740])
ylim([0 61])
grid on

%%%%%%%%%%%%%%%%%%%%%%%%%%%%%%%%%%%%%%%%%%%%%%%%%%%%%%%%%%%%%%%%%%%%%%%%%%%%%%%

ball6_magnitude = mag;       % [Pa]
ball6_x_pos = xp56(flag);    % [grid points]
ball6_y_pos = yp56(flag);    % [grid points]
ball6_z_pos = 0;             % [grid points]
ball6_radius = rad(flag);    % [grid points]
ball_6 = ball6_magnitude * makeBall(Nx, Ny, Nz, ball6_x_pos, ball6_y_pos, ball6_z_pos, ball6_radius);
source.p0 = ball_6;
y_line = [0 0 0];
x = (-30:1:30) * dx;                    % [m]
y = y_line(flag) * dy * ones(size(x));    % [m]
z = zeros(1,length(x));                 % [m]
sensor.mask = [x; y; z];

% input arguments
input_args = {'PlotPML', true,'DataCast', 'single', 'CartInterp', 'nearest'};

% run the simulation, FIRST ORDER
sensor_data(6,:,:) = kspaceFirstOrder3D(kgrid, medium, source, sensor, input_args{:});

Pa6(:,:) = sensor_data(6,:,:);
figure;
surf(Pa6);
colormap(getColorMap);
view(90,90)
```

```
%zlim([-max(abs(sensor_data(30,:))) max(abs(sensor_data(30,:)))])
shading interp % gets rid of the lines
title(['Source 6 at ', num2str(mag), ' Pa, Arc Array'])
ylabel('Sensor Number');
xlabel('Samples (1143.3 sam/s)');
colorbar;
xlim([0 740])
ylim([0 61])
grid on

%%%%%%%%%%%%%%%%%%%%%%%%%%%%%%%%%%%%%%%%%%%%%%%%%%%%%%%%%%%%%%%%%%%%%%%%%%%%%%%

ball7_magnitude = mag;      % [Pa]
ball7_x_pos = -xp78(flag);  % [grid points]
ball7_y_pos = yp78(flag);   % [grid points]
ball7_z_pos = 0;            % [grid points]
ball7_radius = rad(flag);   % [grid points]
ball_7 = ball7_magnitude * makeBall(Nx, Ny, Nz, ball7_x_pos, ball7_y_pos, ball7_z_pos, ball7_radius);
source.p0 = ball_7;
y_line = [0 0 0];
x = (-30:1:30) * dx;                    % [m]
y = y_line(flag) * dy * ones(size(x));  % [m]
z = zeros(1,length(x));                 % [m]
sensor.mask = [x; y; z];

% input arguments
input_args = {'PlotPML', true,'DataCast', 'single', 'CartInterp', 'nearest'};

% run the simulation, FIRST ORDER
sensor_data(7,:,:) = kspaceFirstOrder3D(kgrid, medium, source, sensor, input_args{:});

Pa7(:,:) = sensor_data(7,:,:);
figure;
surf(Pa7);
colormap(getColorMap);
view(90,90)
%zlim([-max(abs(sensor_data(30,:))) max(abs(sensor_data(30,:)))])
shading interp % gets rid of the lines
title(['Source 7 at ', num2str(mag), ' Pa, Arc Array'])
ylabel('Sensor Number');
xlabel('Samples (1143.3 sam/s)');
colorbar;
xlim([0 740])
ylim([0 61])
grid on

%%%%%%%%%%%%%%%%%%%%%%%%%%%%%%%%%%%%%%%%%%%%%%%%%%%%%%%%%%%%%%%%%%%%%%%%%%%%%%%

ball8_magnitude = mag;      % [Pa]
ball8_x_pos = xp78(flag);   % [grid points]
ball8_y_pos = yp78(flag);   % [grid points]
ball8_z_pos = 0;            % [grid points]
ball8_radius = rad(flag);   % [grid points]
ball_8 = ball8_magnitude * makeBall(Nx, Ny, Nz, ball8_x_pos, ball8_y_pos, ball8_z_pos, ball8_radius);
source.p0 = ball_8;
y_line = [0 0 0];
```

```
x = (-30:1:30) * dx;                    % [m]
y = y_line(flag) * dy * ones(size(x));    % [m]
z = zeros(1,length(x));                 % [m]
sensor.mask = [x; y; z];

% input arguments
input_args = {'PlotPML', true,'DataCast', 'single', 'CartInterp', 'nearest'};

% run the simulation, FIRST ORDER
sensor_data(8,:,:) = kspaceFirstOrder3D(kgrid, medium, source, sensor, input_args{:});

Pa8(:,:) = sensor_data(8,:,:);
figure;
surf(Pa8);
colormap(getColorMap);
view(90,90)
%zlim([-max(abs(sensor_data(30,:))) max(abs(sensor_data(30,:)))])
shading interp % gets rid of the lines
title(['Source 8 at ', num2str(mag), ' Pa, Arc Array'])
ylabel('Sensor Number');
xlabel('Samples (1143.3 sam/s)');
colorbar;
xlim([0 740])
ylim([0 61])
grid on

%%%%%%%%%%%%%%%%%%%%%%%%%%%%% do the linear summation of the 8 signals and plot

sum_data1 = sum(sensor_data(1:8,:,:),1);

Pa_sum(:,:) = sum_data1(1,:,:);
lin_sum_fig = figure;
surf(Pa_sum);
colormap(getColorMap);
view(90,90)
%zlim([-max(abs(sensor_data(30,:))) max(abs(sensor_data(30,:)))])
shading interp % gets rid of the lines
title(['Linear Summation at ', num2str(mag), ' Pa, Arc Array'])
ylabel('Sensor Number');
xlabel('Samples (1143.3 sam/s)');
colorbar;
xlim([0 740])
ylim([0 61])
grid on
saveas(lin_sum_fig,'summed_surface.fig')

%%%%%%%%%%%%%%%%%%%%%%%%%%%%%%%%%%%%%%%%%%%%  This section will be for the SIMULTANEOUS
data

source.p0 = ball_1 + ball_2 + ball_3 + ball_4 + ball_5 + ball_6 + ball_7 + ball_8;
% source.p0 = ball_1 + ball_2 + ball_5 + ball_6;
% source.p0 = ball_1 + ball_2;

% define a series of Cartesian points to collect the data
y_line = [0 0 0];
x = (-30:1:30) * dx;                    % [m]
```

```
y = y_line(flag) * dy * ones(size(x));    % [m]
z = zeros(1,length(x));                   % [m]
sensor.mask = [x; y; z];

% input arguments
input_args = {'PlotPML', true,'DataCast', 'single', 'CartInterp', 'nearest'};

% run the simulation, FIRST ORDER
sensor_data(9,:,:) = kspaceFirstOrder3D(kgrid, medium, source, sensor, input_args{:});

Pa_sim(:,:) = sensor_data(9,:,:);
simult_fig = figure;
surf(Pa_sim);
colormap(getColorMap);
view(90,90)
%zlim([-max(abs(sensor_data(30,:))) max(abs(sensor_data(30,:)))])
shading interp % gets rid of the lines
title(['Simultaneous Sources at ', num2str(mag), ' Pa, Arc Array'])
ylabel('Sensor Number');
xlabel('Samples (1143.3 sam/s)');
colorbar;
xlim([0 740])
ylim([0 61])
grid on
saveas(simult_fig,'simult_surface.fig')



%%%%%%%%%%%%%%%%%%%%%%%%%%%%
%%%%%%%%%%%%%%%%%%%%%%%%%%%%
%%%%%%%%%%%%%%%%%%%%%%%%%%%%
% all below is from previous code, could be adapted to make plots for this code

% %% find the angle between the outside sources
%
% %angle_deg(1,1) = 360;
% angle_deg(1,1) = abs(2*atan(xp12(2)./yp12(2))*180/pi);
% % for ii = 3:5
% %     angle_deg(1,ii) = abs(tan(xp12(ii)./yp12(ii))*180/pi);
% % end

%% waveform of peak at center sensor, scaled to see nonlinearity increase
[a,b] = size(Pa1);
time = (874.6356e-6.*(0:(b-1))).*1000; % *1000 to put into milliseconds
center_sensor = 30;

fig3 = figure;
plot(time,Pa_sim(center_sensor,:),time,Pa_sum(center_sensor,:))
title(['Central Sensor Pressure v. Time: ', num2str(mag), ' Pa'])
ylabel('Pressure (Pa)');
xlabel('Time (ms)');
xlim([35 100])
legend('Simultaneous','Lin. Summation');
grid on
saveas(fig3,'cent_sens_sum_v_sim.fig')
```

```
%% fft of peak wave : each time step is 8.7464e-4 s

fs = 1.1433e03;    % calculated from time steps and number of samples
pref = 20e-6;

fft_pa_sim = fft(Pa_sim);
L = length(fft_pa_sim)-1;
freqs = fs*(0:(L/2))/L;
P2_sim = abs(fft_pa_sim/L);
P1_sim = P2_sim(1,1:floor(L/2+1));
P1_sim(1,2:end-1) = 2*P1_sim(1,2:end-1);

fft_pa_sum = fft(Pa_sum);
L = length(fft_pa_sum)-1;
freqs = fs*(0:(L/2))/L;
P2_sum = abs(fft_pa_sum/L);
P1_sum = P2_sum(1,1:floor(L/2+1));
P1_sum(1,2:end-1) = 2*P1_sum(1,2:end-1);

figure
plot(freqs,P1_sim,freqs,P1_sum)
title(['Central Sensor FFT: ', num2str(mag), ' Pa'])
legend('Simultaneous','Lin. Summation');


%% animation of surface plot for simultaneous use of 8 sources
figure
surf(Pa_sim);
colormap(getColorMap);
view(0,90)
zlim([-9000 9000])
shading interp % gets rid of the lines
title(['Simultaneous of 8 Sources at ', num2str(mag), ' Pa'])
%ylabel('Sensor Number');
%xlabel('Samples (1143.3 sam/s)');
colorbar;
xlim([0 740])
ylim([0 61])
grid on

vid = VideoWriter('k_wave_simult.mp4','MPEG-4');
open(vid)

% set(gca,'FontSize',24)
set(gca,'nextplot','replacechildren');

% rotation vectors for animation
n = 0:0.1:90;
n(1,1:201) = zeros(1,201);
n(1,202:901) = 0:0.1286:90;

m = 20.*ones(1,length(n));
m(1,1:201) = 90:-0.45:0;
m(1,202:252) = 0:0.4:20;
m(1,701:901) = 20:-0.1:0;
```

```
for i = 1:901

    surf(Pa_sim);
    colormap(getColorMap);
    view(n(i),m(i))
    zlim([-9000 9000])
    shading interp % gets rid of the lines
    title(['Simultaneous 8 Sources at ', num2str(mag), ' Pa'])
    %ylabel('Sensor Number');
    %xlabel('Samples (1143.3 sam/s)');
    colorbar;
    xlim([0 740])
    ylim([0 61])
    grid on

    writeVideo(vid,getframe(gcf))
end
close(vid)

disp('Video 1 Complete')

%% animation of surface plot for linear summation of 8 sources
figure
surf(Pa_sum);
colormap(getColorMap);
view(0,90)
zlim([-9000 9000])
shading interp % gets rid of the lines
title(['Linear Summation 8 Sources at ', num2str(mag), ' Pa'])
%ylabel('Sensor Number');
%xlabel('Samples (1143.3 sam/s)');
colorbar;
xlim([0 740])
ylim([0 61])
grid on

vid = VideoWriter('k_wave_lin_sum.mp4','MPEG-4');
open(vid)

% set(gca,'FontSize',24)
set(gca,'nextplot','replacechildren');

% rotation vectors for animation
n = 0:0.1:90;
n(1,1:201) = zeros(1,201);
n(1,202:901) = 0:0.1286:90;

m = 20.*ones(1,length(n));
m(1,1:201) = 90:-0.45:0;
m(1,202:252) = 0:0.4:20;
m(1,701:901) = 20:-0.1:0;

for i = 1:901

    surf(Pa_sum);
    colormap(getColorMap);
```

```
    view(n(i),m(i))
    zlim([-9000 9000])
    shading interp % gets rid of the lines
    title(['Linear Summation of 8 Sources at ', num2str(mag), ' Pa'])
    %ylabel('Sensor Number');
    %xlabel('Samples (1143.3 sam/s)');
    colorbar;
    xlim([0 740])
    ylim([0 61])
    grid on

    writeVideo(vid,getframe(gcf))
end
close(vid)

disp('Video 2 Complete')
```

D.5 Placement of Sources and Receivers in k-Wave©

The placement of sources and receivers in the k-Wave© environment can prove a bit challenging. This section should provide some useful tips for properly placing your model elements within the modeled environment.

A plot of the grid space in two dimensions will serve to better illustrate the process. Figure D.1 illustrates the kgrid layout for placing elements. The orientation of grid points is not as one would expect for the y-axis values.

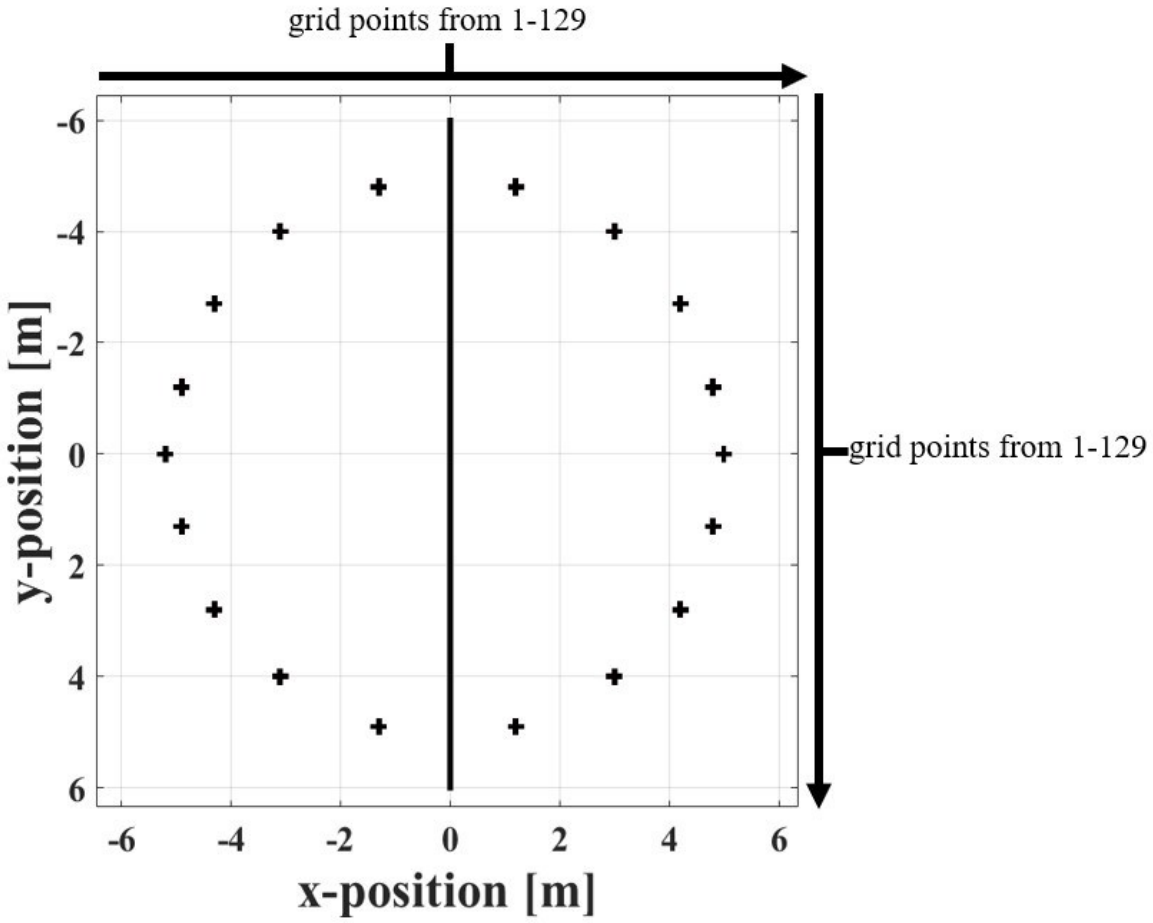

Figure D.1: An example of the grid format and layout with sources and receivers placed as they are in Fig. 4.1, but with the x-axis, and y-axis labels and values as they are in the kgrid function for element placement in k-Wave©.

When creating a grid using the kgrid function, any power of 2 can be used as a limit for the number of grid points in any direction, labeled as Nx or Ny. Here I have used 2^7, or 128, grid points in each cartesian direction. The grids begin at "1" and end with "129". This is important to note as any symmetrical arrangement will have to be centered around the point (65,65) on the grid. In addition to the grid spacing, one can assign a certain number of grid points per meter in order to determine the proper size of the environment being modeled. These are the dx and dy values for input to kgrid. Here is where the challenges begin to arise. The inputs for placing the receivers in the modeled space are expecting values from x-minimum to x-maximum in steps of dx, and the same for the y positions. But the placement of the sources is dictated by grid coordinates. So, as in Fig. D.1, I could place my array of receivers according to any of the x/y coordinates in meters, with the resolution of placement calling from dx and dy in meters. To place sources, however, one must choose a grid point set of coordinates on the plane to place them at. This can prove challenging when attempting to make a symmetric curve, for example. One would be able to place a central receiver at the 0 m in x, and 0 m in y position on the grid. But to place sources around that receiver one must calculate the positions away from the receiver using the Pythagorean theorem, as is standard practice, but then transform that answer in x and y to match the nearest grid point crossing at which the source can actually be placed.

An example of the algorithm is contained below. I developed this to transform the positions in x and y from meters to grid points in quadrant IV of the cartesian plot, Fig. D.1.

```
xs = [1.25 2.75 4 4.85];                          % [x positions in meters]
xp1 = xs.*10+(Nx./2 + 1);                         % [translate those to grid point]
yp1 = round(sqrt(r^2-xs.^2),1).*10 + (Ny./2 + 1); %[y positions in terms of grid points]
```

The positions in the x-direction in meters are given by the array variable "xs". The variable "xp1" translates those positions to a grid point value that is offset by adding the center point in x,

($(Nx/2 + 1) = 65$ for a 128-point grid). The y coordinate is then calculated using the Pythagorean theorem and offsetting the y coordinate by the center point as well in order to place it in quadrant IV correctly. This process can be repeated for each of the quadrants, transforming the positions of the sources in meter coordinates to grid point coordinates.